Microstructural studies on failure mechanisms in thermo-mechanical fatigue of repaired DS R80 and IN 738 Superalloys.

By
Emmanuel Otchere Abrokwah

A thesis submitted to
the Faculty of Graduate Studies
in partial fulfilment of
the requirements for the degree of
Master of Science

Department of Mechanical and Manufacturing Engineering
Faculty of Engineering
University of Manitoba
Winnipeg, Manitoba

February 2012

Abstract.

Directionally solidified Rene 80 (DS R80) and polycrystalline Inconel 738(IN 738) Superalloys were tested in thermo-mechanical fatigue (TMF) over the temperature range of 500-900°C and plastic strain range from 0.1 to 0.8% using a DSI Gleeble thermal simulator. Thermo-mechanical testing was carried out on the parent material (baseline) in the conventional solution treated and aged condition (STA), as well as gas tungsten arc welded (GTAW) with an IN-738 filler, followed by solution treatment and ageing. Comparison of the baseline alloy microstructure with that of the welded and heat treated alloy showed that varying crack initiation mechanisms, notably oxidation by stress assisted grain boundary oxidation, grain boundary MC carbides fatigue crack initiation, fatigue crack initiation from sample surfaces, crack initiation from weld defects and creep deformation were operating, leading to different "weakest link" and failure initiation points. The observations from this study show that the repaired samples had extra crack initiation sites not present in the baseline, which accounted for their occasional poor fatigue life. These defects include lack of fusion between the weld and the base metal, fusion zone cracking, and heat affected zone microfissures.

Acknowledgments

I would like to express my profound gratitude first and foremost to the Almighty God for His guidance and protection throughout my stay in this MSc. Secondly I want to say a big thank you to Dr. Norman Richards, my research supervisor for his dedication and support throughout this MSc. My sincerest gratitude goes to the University of Manitoba and Natural Sciences and Engineering Research Council of Canada (NSERC) for their financial support throughout the course of this study, and to the following for their assistance; Dr. Ojo for helping me to be part of this research group, Dr. Norman Halden & Dr. Sidhu of the Geology Department for helping with the EPMA analysis, Mr Mike Boskwick, and Mr Don Mardis (retired) all of the Mechanical Engineering Laboratory for their assistance with equipments. I am also grateful to my family and friends for their support and diverse contributions and finally to the lecturers and staff of the Mechanical and Manufacturing Engineering Department of University of Manitoba.

Dedication

To my unborn child.

Contents

Front Matter

List of Tables

List of Figures

List of Copyrighted Material

List of Symbols

List of Appendices

CHAPTER 1.0 : Introduction

Superalloys have been used quite extensively in the past decades in high temperature applications in the aerospace and land base power generation industries as turbine components. This is due to their superior resistance to creep, fatigue and oxidation damaging mechanisms at high temperatures close to 0.8Tm in Kelvin. Their strength is mainly derived from the precipitating gamma prime phase and solid solution alloying. During the service life of components such as blades, high stresses and temperature excursions lead to crack initiation and material damage. In addition, environmental factors such as atmospheric oxygen and sulfur from combustion gases exacerbates the problem and accelerates damage. With time, routine component inspection may "call" the component unfit for service prompting repair works or complete replacement. The high cost in replacement makes repairing schemes, some 60% replacement cost more attractive as operation cost is reduced by some 40%. Replacement cost for a modern High Pressure Turbine (HPT) stage 1 blade is about $600,000 USD per engine [Year 2000], thus repair cost of up to 60% replacement cost to damage component is more attractive [1]. Repair techniques such as vacuum braze and gas tungsten arc welding are being used for various types of repair in the aerospace and power generation industries. Other alternatives under consideration and research include electron beam welding, laser welding, low heat input, diffusion bonding, wide gap brazing and plasma spray. Amongst these methods, the widely understood and more familiar technique, which is more cost effective to date to repair industries is the gas tungsten arc welding (GTAW). However, after repair, there is varying fatigue data for the repaired components. Some of the repaired components have comparatively good fatigue properties as the baseline material

whereas others have inferior fatigue properties compared to the baseline. These disparities have been identified as the lack of repair process optimization that causes variation in weld quality leading to unwanted defects in the repaired component. With the presence of extra failure initiation sites in the repaired component, cracks are likely to initiate from numerous places compared to the baseline, accounting for their occasional inferior fatigue properties at high temperatures. It is therefore imperative to identify what these initiation mechanisms are, how they occur and in which areas of the repaired components they are located. This knowledge will better equip the repair engineer to be able to select the best repair techniques and process parameters towards an optimize process that minimizes the effect of these failure sites in the repaired components. This thesis is divided into five chapters. Chapter one will provide a general overview of the need to look at the failure mechanisms in the repaired component of IN 738 and DS R80. Chapter two will present a literature review on Ni-base Superalloys, their baseline microstructure, alloying elements, and strengthening mechanisms. The chapter will further discuss the nomenclature of welds and some known defects and a review of the various failure mechanisms in Superalloys at elevated temperatures. The third chapter deals with the methodology, and the results of the various experiments would be discussed in chapter four. The final chapter, chapter 5 , summarizes the results presented in the fourth chapter and then make recommendations for future works.

CHAPTER 2.0 Literature Review

2.1 History of Superalloys

The advent of higher performing turbine engines brought the forging of complex alloy system in the mid-1960s [2]. Other authors [3] date the advent of the coming of Superalloys even some decades back to the 1920's, with development expanding in the nineteen fifties and sixties. With the increase in alloy content of Ni-based Superalloys for better creep and stress rupture capability with time, the alloys became increasingly difficult to forge. This necessitated a change in the fabrication process to casting to accommodate the complex elemental combination. The investment casting process was preferred over other fabrication techniques because it is amendable to the fabrication of hollow blades with complex and detailed cooling passages [4], which allows for higher operating temperatures. Since the middle of the1980s, turbine inlet temperatures have appreciated by about 260 ºC. About 50% of this increase is attributed to more efficient designs, while the other half is due to improved Superalloys and casting techniques. For example, the introduction of directional solidification promoted up to a 50 ºC increase in operating temperature with thermal fatigue strength approximately 10 times that of the polycrystalline counterpart [5], while the single crystal process produced a further increase in operating temperatures for the alloys[2].

The first generation of the cast blades and vanes were fine grained polycrystalline structures produced by conventional investment casting techniques. These blades were then heat treated to coarsen the grain structures for enhanced creep resistance. Improvement in the casting technique made it possible to produce directionally solidified

(DS) structures with columnar grains oriented along the longitudinal axis of the blade. The columnar grain structure enhances the elevated temperature ductility property by alignment [3] or eliminating the grain boundaries perpendicular to stress axis as failure initiation sites. An additional improvement over the DS process was the development of the single crystal (SX) process in which a single crystal grows to form the entire blade. Since there are no grain boundaries in the SX process, grain boundary strengtheners, which are also low melting point element that causes incipient melting were reduced or eliminated entirely, allowing even higher operating temperatures [2]

2.1.1 Polycrystalline casting

For many applications such as blades and vanes, DS and SX castings have replaced polycrystalline castings, however, polycrystalline castings are still utilized for structures such as compressor housings, diffuser cases, exhaust casings and engine frames [2]. Its continued use is currently attributed to the relatively low cost and ease of fabrication [6]. Some of these parts are very large and the castings can weigh up to 1500 lb. The benefit of casting large structural parts allows reduced manufacturing costs and eliminates the casting of many smaller parts which will require further joining processes. Since many of these parts are strength and fatigue critical, innovations have been developed to produce castings with finer and more uniform grain sizes [2].

2.1.2 Directional solidification (DS) casting

With the increase in demand for gas turbines to be operated at higher temperatures, new frontiers in alloying and process improvement became necessary and a drive towards directionally solidified alloys to meet this challenge intensified, resulting in alloys such as MAR-M200 [7].

In the development of directionally solidified structure, it is of outmost importance that the dendrites (grains) grow from one end of the casting to the other. This is accomplished by creating a steep temperature gradient, by removing the majority of the heat from one end of the casting. Controlling of temperature and cooling rate are critical in DS alloy manufacturing. If the thermal gradient is too fast, grains will nucleate ahead of the solid/liquid interface, on the other hand, if the movement is too slow, excessive macrosegregation will occur in addition to freckles formation, which are defects of equiaxed grains with interdendritic composition. The process is normally automated to achieve proper grain growth. Typical defects in DS castings include equiaxed grains, misoriented grains, grain boundary cracking, excessive shrinkage and microporosity. Increasing the thermal gradient during casting is used to control the formation of equiaxed grains, misoriented grains and microporosity [2].

2.1.3 Single crystal (SX) casting

The DS casting process was modified to suppress all the growing columnar grains but one, to cast parts with only a single grain, thereby eliminating all of the grain boundaries. This process further increased the operating temperatures within which turbine blades could be used due to the elimination of the grain boundaries and subsequent improvement

in creep rupture properties [8]. In addition, alloying elements that were necessary to prevent grain boundary cracking, but were detrimental to creep strength, namely boron, hafnium, zirconium and carbon, could be eliminated [2].

2.2 Alloying elements

The composition of most Ni-base Superalloys contains at least 12-13 important elements that are carefully controlled during fabrication. They include Ni, Co, Cr, Fe, Mo, W, Nb, Ta, Ti, Al, C, B, Zr and Hf. In general, most precipitation hardening Ni base Superalloys contain 10-20% chromium, about 8% aluminum and titanium, 5-10% cobalt and small amounts of boron, zirconium, and carbon. Other common additions include molybdenum, tungsten, niobium, tantalum, and hafnium [3]. These elements partition into either the gamma matrix, the gamma prime, the carbides or the grain boundaries. Elements from groups V, VI, and VII, notably nickel, cobalt, iron, chromium, molybdenum and tungsten make up the face-centered-cubic (FCC) austenitic γ matrix [3]. In general, refractory alloy elements with large atomic radii compared to Ni are added for the solid-solution strengthening of the gamma phase [9]. Cobalt has been reported to decrease the solubility of elements, which form a precipitate [10]. Groups III, IV and V elements such as aluminum, titanium, niobium, tantalum and hafnium partition to make the up the FCC intermetallic ordered γ’ precipitate [3]. It is this γ’ phase which is responsible for the useful high-temperature properties of most precipitation hardening Ni base Superalloys [10]. Boron, carbon and hafnium elements from Groups II, III and IV tend to segregate to grain boundaries [3]. These elements have been found to increase the rupture life of Ni base Superalloys when added in small amounts [10]. One explanation given to this

observation is that, boron and zirconium atoms occupy grain boundaries and fill up open spaces present there. This confers some strength to the grain boundary by slowing down diffusional processes, which contribute to creep deformation [10]. Another proposal, which has been backed by experimental results, suggests that grain boundary boron and zirconium suppresses early agglomeration of $M_{23}C_6$ carbides, which leads to subsequent cracks. This suppression was attributed to the reduction in carbon segregation by boron and zirconium. This effect has also been observed to encourage intragranular carbide precipitation, which improves on creep resistance of the alloy. The carbide precipitation on grain boundaries is also important for control of grain size during wrought processing [9]. However, if boron is added in excess amount, hard, brittle and low melting point borides may precipitate on the grain boundary. This could be a problem in forging wrought alloys due to their low melting point [10]. Also during high temperature applications, these borides could melt causing gain boundary voids and separation. Two other sub-classifications include the carbide formers-titanium, chromium, molybdenum, tungsten & tantalum and the oxide formers-aluminum and chromium [3]. In recent developments, the weight percent (wt%) of chromium has been reduced by some 10% in order to allow more additions of aluminum needed to increase the volume fraction of the γ' precipitates. The decrease in chromium content does affect the alloys ability to resist oxidation. Donachie et al [10] reported that, the highest normal operating temperatures of today's engines are such that even 20% of chromium does not offer sufficient oxidation resistant. Table 2.1 shows a summary of some effect of several elements in Ni base Superalloys.

The presence of yttrium in some of these alloys, aids in the formation of adherent oxide scale to substrate for oxidation resistance. In second and third generation of powdered metallurgy Superalloys, additions of about 3wt% and 6wt% rhenium has led to an increase in creep strength as a result of inducing a negative misfit by partitioning into the γ matrix and promoting rafting in the microstructure. It is also reported that Re reduces the overall diffusion rate in nickel base Superalloys[11]

Table 2.1: Alloying elements in a Ni-base Superalloys [5]

Element	Known Effect
Cr	Oxidation resistance, carbide former $M_{23}C_6$ and M_7C_3.
Mo&W	Solid-solution strengtheners, carbide formers M_6C and MC
Al&Ti	Formation of γ'[Ni_3(Al,Ti)] hardening precipitate, Ti forms MC
Co	Raises solvus temperature of γ'
B&Zr	Increase rupture strength, B forms borides when present in large amounts.
C	Formation of various carbides such as MC, M_6C, $M_{23}C_6$, M_7C_3
Nb	Formation of Ni_3Nb hardening precipitate, carbide former
Ta	Solid-solution strengthener, carbide former MC

2.3 Microstructure of Ni base Superalloys

The base microstructure of precipitation hardened Ni base Superalloys comprises of the gamma matrix, the gamma prime and double gamma prime phase, the gamma-gamma eutectics, Ni-Zr and Ni-Ti intermetallics, primary MC carbides and grain boundary carbide precipitates, namely $M_{23}C_6$, M_6C and boride particles. These phases may be present depending on the heat treatment, operating temperature and time for the alloy in operation. The various phases will be discussed below.

2.3.1 The Gamma matrix γ

The gamma γ matrix has the austenitic structure of Ni necessary for good elevated temperature creep properties. This matrix is strengthened by solid solution elements such as chromium, molybdenum, cobalt and tungsten [12]. The phase has a cubic lattice structure with similar lattice parameter to the γ'. The lattice parameter of γ nickel is 3.52Å, but with the addition of solid solution strengthening elements, the lattice parameter is usually measured as 3.56 Å [12]. Because of similarity in the lattice parameters between the matrix and the precipitated phase, the γ matrix is often coherent with the γ' phase when the precipitates are small in size. The small misfits between the γ matrix and the γ' phase results in a low γ/γ' interfacial energy. The magnitude and the sign of the misfit would influence the development of microstructure under applied load at elevated temperatures.

$$\delta(\text{mis-fit}) = (a\gamma' - a\gamma) / 0.5(a\gamma' + a\gamma) \quad \ldots\ldots(1)$$

where aγ’ and aγ are the lattice parameters of the γ’ and the γ phases respectively. This misfit will result in initial internal stresses which will strongly influence precipitate shape and resultant mechanical property [9,13]

With a small misfit the alloy forms a coherent interface and such microstructures are very stable at elevated temperature applications. One other microstructure implication of misfit is the sign of misfit and how it encourages rafting. When the γ matrix has relatively smaller lattice parameter than the γ’ phase, the misfit is said to be positive and this can be altered by changing the composition of the alloy especially the aluminum to titanium ratio. A negative misfit does encourage the formation of raft γ‘ phase which is essentially layers of the phase in a direction normal to the applied stress. This rafting can help reduce creep rate if the main mechanism involves the climb of dislocations across the precipitate raft. [11]

The Ni gamma matrix is favored for most gas turbine design for high temperature applications, some within 0.9Tm in Kelvin. Such Superalloys with Ni as its base element are capable of running for hundreds of thousands of hours for somewhat low temperature applications. The basic reason for such resilience to harsh working conditions of high temperature and oxidation may be due to nickel’s ability to tolerate alloying without phase instability [3].

2.3.2 The Gamma prime γ'

Gamma prime γ' is the principal precipitation hardening strengthening phase in precipitation hardened Ni base superalloys [12,14,15]. This unique intermetallic phase contribute remarkable strength by dislocation bypassing or particle cutting through the γ-γ' alloy. Is quite interesting to note that, the strength of this intermetallic phase increases with increase in temperature and reduces at about 600 ^{o}C and above [11]. Details of the strengthening mechanism by γ' phase will be discussed later. The nominal composition of γ' phase is Ni_3Al although it is usually designated Ni_3[Al,Ti] since as much as 65% of the aluminum can be replaced with titanium [12]. Sims et al [3] quotes the composition formula as $(Ni,Co)_3(Al,Ti)$. Replacement of the Ti can alter the appearance of the γ' and the resultant lattice parameter. The nickel can also be replaced with chromium and cobalt to a limited degree. The gamma prime has a face centered cubic structure with a lattice parameter of a_o=3.58-3.59 Å [16] for stoichiometric Ni_3Al gamma prime. The γ' and γ usually have identical FCC structure with their lattice parameter differing by some 5% [12]. In the lattice, the nickel atoms are at the face centers and the aluminum and the titanium atoms are at the corners of the cube. However, this phase is not strictly stoichiometric as there may exist excess of vacancies in one of the sublattice such that, nickel atoms might occupy the aluminum site and vice-versa. In addition to aluminum and titanium, niobium, hafnium and tantalum may preferentially partition into the γ' phase [11]. The γ' phase can be precipitated out of the γ matrix either through aging after solution treatment, or during cooling of the casting through temperature range of about 534^{o}C – 983^{o}C. Formation of the γ' phase occurs in the solid state as the supersaturated solid solution of γ-nickel is cooled below the solvus temperature. It will initially nucleate

in the γ matrix as a coherent precipitate having its crystallographic orientation identical to the orientation of the γ matrix [12]. Hence the precipitation and the growth kinetics of the γ' phase are dependent on the cooling rate at which the alloy is cooled through the solvus temperature. Cooling rate in excess of 40K/min will typically precipitate a unimodal distribution of fine γ' with sizes of 300-500nm. Slower cooling rate tends to promote the formation of bi-modal distribution of γ' phase with size ranging from <50nm and >500nm [9]. During solution treatment, they normally go into solution at about 1235 ^{o}C to 1250 ^{o}C [17] In addition, larger γ' is able to precipitate on grain boundaries during cooling, aging or annealing process. Another type of γ' is formed during eutectic solidification of liquid metal called the γ-γ' eutectic. During solidification of the cast Ni base Superalloy, a solution which is highly saturated in γ' forming elements namely Al and Ti are formed due to dendritic segregation. When the supersaturation of the eutectic liquid with γ' forming elements is high enough such that retention of the element is impossible, the eutectic γ' phase forms [12]. A large number of Superalloys, in particular the heat treated ones show two sizes of γ' precipitate. The larger or primary γ' phase which is usually nucleated at high temperature forms first followed by the smaller secondary γ' phase at lower temperatures during cooling or during later stages in heat treatment [12]. For a given chemical composition, the volume fraction of γ' decreases with increase in temperature. During heat treatment, this phenomena is used to dissolve the γ' phase at sufficiently high temperature and then aged in order to precipitate uniformly dispersed and fine phase [11].

In most metal and their alloys, strength decreases instantaneously with increase in temperature. This reason is attributed to the fact that at elevated temperatures, thermal

activation makes it easier for dislocation motion to surmount obstacles. However, the precipitated γ' phase in the nickel base Superalloy are particularly resistant and stable even at elevated temperatures. Ordinary slip in both γ and γ' occurs along {111}<110>. If all conditions being equal and slip is confined to just these two planes at all temperatures, then it is expected that the alloy should behave similar to any other metal with decrease in strength at elevated temperatures. However, there is the possibility of cross slip from their usual {111} plane to {110} plane where they have lower anti-phase domain boundary energy. This cross slip sometimes causes extended dislocations to be positioned partly on the close-packed plane and partly on the cube plane. Such a dislocation becomes locked leading to an increase in strength. This strength decreases at temperatures beyond 600^{o}C [11].

2.3.3 The γ'' phase

For applications where greater strength is required at lower temperatures (eg. Turbine disc), alloys can be strengthened using another phase referred to as γ'' and they normally occur in nickel base Superalloys when there is considerable additions of niobium (Inconel 718) or vanadium [11,18]. The composition of the γ'' phase is therefore written as Ni_3Nb or Ni_3V and normally occur as disc in the microstructure. The crystal structure is a body centered tetragonal (BCT) structure with an ordered arrangement of Ni and Nb/V atoms. Strengthening therefore occurs by both coherency hardening and order hardening mechanisms. The lattice parameter of the γ'' are a_o=0.362nm and c_o=0.741nm [11]. It is reported to precipitate in the temperature range of 550^{o}C-660^{o}C but other authors also report even higher temperatures of 700^{o}C-900^{o}C [18].

2.3.4 Carbides

There are basically three types of carbides namely the MC carbides, the $M_{23}C_6$ carbides and M_6C carbides. The MC carbides normally are found at both within the grain boundary and inside the grains. The $M_{23}C_6$ and the M_6C are normally located at the grain boundaries. Their primary function is to confer some strength to the matrix but their purpose is served better on the grain boundary where they retard diffusion damaging mechanism at high temperatures. Some early researchers noted the detrimental effect of carbides located on the grain boundary and took mitigation steps to reduce the amount of carbon composition in the alloy [3], as they can serve as crack initiation sites. However, further studies of carbon reduction uncovered sharply the reduced creep properties and ductility of common Superalloys such as Nimonic 80A and Udimet 500 [3].

If no carbides were present, excessive grain boundary sliding may occur which will lead to premature failure, on the other hand, a continuous film formation of carbides on the grain boundary would render stress relaxation difficult and failure again occurs prematurely. The optimum carbide distribution desired is one that encourages stress relief by restricted grain boundary sliding but one that will not offer a continues path for fatigue crack propagation. The condition where carbides are relatively small and uniformly dispersed lead to the best combination of properties [10]. Thus, there is divided opinion as to whether carbides should be tolerated or avoided in the matrix of the alloy. A lot more investigators seem to welcome their presence, arguing that its benefits may outweighs its disadvantages. Therefore understanding their chemical composition, morphology, distribution and the types is very critical to alloy design and heat treatment processes [3].

2.3.41 MC carbides

The MC carbide is the most common type of carbide found in Superalloys and is usually of the TiC type. The TiC has a cubic FCC structure with lattice parameter a_o=4.32Å. Although the metal of the carbide is predominantly titanium, other elements such as tantalum, zirconium, niobium, molybdenum, vanadium and chromium could substitute for the titanium. These carbides are irregularly shaped and are uniformly dispersed through out the grains and at grain boundaries. It is normally the first carbide to form in the Superalloy during solidification and at high temperatures, they tend to break up for more stable carbides of $M_{23}C_6$ and M_6C [12]. Because of the considerable amount of volume occupied by these carbides along the grain boundary, potential mechanical property degradation may occur when MC carbide undergo this phase transformation. Although carbides are sources of crack initiation during fatigue, discrete carbides located on the grain boundary impedes grain boundary sliding at high temperatures during creep. [9].

2.3.42 $M_{23}C_6$

This type of carbide is predominantly rich in chromium. They are common in alloys with moderate to high chromium content [3]. It has an FCC crystal structure with a lattice parameter a_o=10.638Å. Even though chromium is the dominant metal element, other traces of elements such as nickel, cobalt, iron, molybdenum, and tungsten is quite common. It usually nucleate and form at lower temperatures and grows slowly compared to MC carbides [12]. Sims et al [3] reports their formation at temperatures between 760-980^{o}C from either degenerated MC carbide or from soluble carbon residual in the alloy matrix. The preferred precipitation locations for the carbides are grain boundaries and upon aging or further annealing, they may precipitate at twin boundaries. In cases where they precipitate from MC carbide decomposition, they are normally found in close proximity to the MC carbides. $M_{23}C_6$ go into solution at about 1040^{o}C [12] and are therefore useful in controlling grain boundary slip and grain boundary growth at high temperatures compared to MC carbides. The shape and form of $M_{23}C_6$ precipitates is dependent on the chemical composition as well as grain size. For instance, substantial amount of Cr above 12wt% will lead to the formation of a continuous film along the grain boundary. When considerable amount of molybdenum and tungsten are present, the approximate composition is given as $Cr_{21}(Mo,W)_2C_6$. However, considerable Ni can also substitute in the carbide with Co and Fe also substituting for the chromium [3]. The effect of the grain size results from the extent of precipitation possible at grain boundary. The larger the grain size, the smaller the grain boundary area available for precipitation formation. A given volume of precipitate such as $M_{23}C_6$ will therefore form a thicker and

more continuous film as grain sizes increase. On the other hand, if the grain size is too fine, the density of $M_{23}C_6$ becomes so small that a loss in rupture life occurs [10].

Rupture failure can initiate either from non-existence of these carbides on the grain boundary or by the zipper akin brittle fracture when precipitated as a continuous film [3].

2.3.43 M_6C

The majority of cobalt based and nickel based Superalloys that contains relatively high amount of the heavy elements-tungsten and molybdenum will preferentially form M_6C instead of $M_{23}C_6$ carbides. Although tungsten and molybdenum are the two main metal elements for this carbide, they can sometimes be substituted for by chromium, cobalt and nickel. Like the $M_{23}C_6$, they prefer to form on the grain boundary and sometimes can be randomly distributed throughout the matrix. It has a cubic structure with lattice parameter of a_o=10.5Å and can sometimes form in the vicinity of MC carbide breaking down [12]. Again, like $M_{23}C_6$, it is useful on the grain boundary at high temperatures to prevent sliding. It is quite stable at higher temperatures compared to the $M_{23}C_6$. Typical formulae for M_6C are $(Ni,Co)_3Mo_3C$ and $(Ni,Co)_2W_4C$. Other data even suggest wider composition for M_6C with formulas ranging from approximately M_3C to $M_{13}C$. Unlike more rigid $M_{23}C_6$, the composition can vary widely [3].

2.3.5 Sigma phase

The sigma phase is a hard and brittle phase which normally forms from transition metal elements. It has a tetragonal structure with 30 atoms per unit cell [12]. The lattice parameters of a chromium-cobalt sigma phase are a_o=8.81Å and c_o=4.56Å. The most frequently encountered sigma phases are formed from elements of manganese, chromium, cobalt, nickel, iron and molybdenum, the latter five are most common on nickel base Superalloys. It is thought that the formation of sigma phases in Superalloys is detrimental to the mechanical and chemical properties of the alloy in that the hard brittle nature tends to lower the ductility of the alloy and also its formation robs the matrix of chromium and molybdenum, which are useful for solid solution strengthening. Another possible adverse effect of the formation of the sigma phase is that, it ties up chromium and reduces the oxidation resistance of the alloy. Its hardness however does not increase the hardness of the alloy since it forms after long hours of exposure of the alloy to heat, which would have been overaged and softened. They normally form by nucleation and growth usually at long and often several of thousands of hours. The temperature range where most alloys are prone to sigma formation are between 820^{o}C and 900^{o}C and will preferentially form on grain boundaries, twin boundaries, and interfaces of second phase particles such as carbides and borides [12].

2.3.5 Borides

Boron is generally present in Superalloys at very low levels such as parts per million range. It has both beneficial and detriment effect on the mechanical properties of the Superalloy. For example, when present in its elemental state on the grain boundary, it blocks the onset of grain boundary tearing under creep rupture loading. When present at relatively high levels of 1200ppm, the elemental boron can react to form M_3B_2 or M_5B_3 boride particles. They are normally reported to have shapes varying from blocky to half-moon in appearance and are known suppliers of boron to the grain boundary [3]. It is reported to have a tetragonal unit cell with dimensions a_o=5.78Å c_o=3.13Å and c_o/a_o=0.542 [12].

2.4 Heat treatment

Microstructure of cast Superalloys are normally altered by heat treatment processes to obtain good mechanical properties at high temperatures. In the as-cast condition, the microstructure is as a result of the slow cooling of the melt alloy and has the characteristic dendrite structure of solidified melt. Because of segregation associated with dendritic solidification, there are elemental concentration gradient throughout the alloy, which in most cases is heterogeneously distributed. At the centre of the matrix, it is usually reported to be richer in elements [Co, Al, & Ti] that reduces the melting point of the nickel. The principal methods of altering the microstructure of the as-cast alloy are through controlling their cooling rate and chemical composition modification. In addition, the microstructure of the cast alloy can be slightly modified by appropriate heat

treatment. After the heat treatment, the alloy can revert back to its prior heat treated microstructure only by going back into the melt [12].

There are two stages of heat treatment employed to precipitate the desired microstructure for Superalloys. The first one is solution treatment, and the second is aging treatment. The purpose of the solution treatment is put as much of the phases into a single solid solution at temperatures below what would normally cause incipient melting of the alloy [11]. This is accomplished by heat treating the alloy above the solubility limit of γ' phase. This is to ensure that, upon subsequent ageing at lower temperatures, a large volume fraction of γ' will be precipitated [10]. This first phase is followed by a single or multiple ageing treatments at which time the carbides and the γ' will nucleate and grow [12]. In some alloys, more than one aging treatment is employed to precipitate duplex size phases. One good reason for this procedure is to provide strength over wide range of temperature applications [10]. The heat treatment would vary from one alloy composition to the other and various alloys will have their own unique heat treatment depending on the final outcome of desired microstructure and property of the final alloy [11].

The heat treatment is normally carried out at both high and low temperatures to precipitate specific microstructures. For example, the higher temperature heat treatment precipitates coarser particles of γ' phase while as lower temperature heat treatment leads to the precipitation of finer secondary dispersion. In most cases, both high and low temperature heat treatment are utilized simultaneously to produce coarse and fine precipitate γ' known as bi-modal distribution. One other effect of temperature of heat treatment is on the grain size. For example, when the alloy is heat treated at the subsolvus

temperature, the grains are normally relatively small but when treated at super solvus temperature, the grains grow bigger because the majority of the γ' dissolves and there is no pinning effect during the migration of the γ-γ' boundary interface [11].

To achieve effective strengthening by precipitation hardening of an intermetallic phase, it essential that the following conditions must be achieved [10]:

1. volume fraction of at least 30%
2. interparticle spacing on the order of 500Å
3. A strength greater than that of the matrix to minimize slip cut
4. Good lattice mismatch (within 1%) with matrix to promote stability.
5. Sufficient ductility to prevent easy path of fracture.

These requirements are essential, however, in some alloy designs; some may not be very critical. For example, in relation to the interparticle spacing, it had been found out that the creep resistance of M-252 (small volume of γ') at 871^{o}C is sensitive to particle size and spacing between the precipitates, but not in IN 700 (large volume fraction of γ'). It was concluded that for γ' volume fraction in excess of 40% may render some alloy systems insensitive to effect of particle spacing [10]

2.4.1 Stability of microstructure during heat treatment

2.4.11 The γ'

The γ' phase is perhaps the most sensitive of the phases to time at very high temperatures. The rate of overaging of the γ' is greatly controlled by the chemical composition of the γ' and the γ matrix surrounding it. Its been reported by Johnson& Donachie [12] that γ' phase anneals in two ways, namely losing its regular appearance and by growth through agglomeration. It has been observed in some alloys that γ' envelopes around carbides and borides and also on grain boundaries after aging. The stability of γ' phase during annealing process have been determined to be dependent on the chemical make up of the γ' phase. For example, in Udimet 700 sample, sigma phase noted to form at the peripheral grains and in regions where the MC carbides broke down in favor of $M_{23}C_6$, the γ' phase aged rapidly. This was explained based on the fact that, the depletion of chromium by the formation of the $M_{23}C_6$ or a chromium rich sigma phase must have caused the rapid ageing of the γ' phase. For bi-modal distribution of γ' phase, the γ' most sensitive to annealing are the smaller secondary ones formed at lower temperatures. In exposed Udimet 700 samples, the secondary γ‘ were more sensitive to annealing than the larger primary γ‘ phase [12].

2.4.12. The carbides

The type of carbides present after heat treatment can be greatly influenced and altered during and after annealing. In almost all Ni-based Superalloys, a substantial amount of MC carbides are present after casting or annealing process. The MC carbides are usually the only or first carbide to respond to annealing process at temperatures of about 760^{o}C to incipient melting point temperature at which some undergo decomposition/break down. The MC carbides typically solution at about 1232^{o}C, but it can undergo a decomposition reaction at temperatures above 1093^{o}C in as few as 10 hours [12]. Depending on the composition of the primary MC carbide and the overall alloy composition, subsequent solid state transformation may decompose the MC carbide into a variety of $M_{23}C_6$, M_6C and M_7C_3 during heat treatment and in service. For example, Cr from the matrix can potentially react with the less stable TiC and NbC carbides to form series of $M_{23}C_6$, M_6C and M_7C_3 carbides. As the primary MC carbides are consumed, there is depletion of Cr from the matrix [9]. The type of carbide formed from the break down of the MC carbide will depend on the overall composition of the alloy and the temperature. In general, alloys that contain a total of less than 6wt% molybdenum plus its equivalent tungsten will favor the formation of $M_{23}C_6$. However, in alloys that contain relatively higher amount of tungsten and molybdenum will produce M_6C. The $M_{23}C_6$ will initially form as globular carbides on the grain boundary and then will later on nucleate in the grains especially on twin boundaries. It has been noted that, annealing exposure does not increase the size of these carbides, but instead increases the quantity of carbides present. For alloys that have high content of chromium, continuous $M_{23}C_6$ can precipitate on grain boundary during heat treatment. In the normal operating temperatures (700^{o}C-1000^{o}C) for Superalloy

applications, the M_6C and the $M_{23}C_6$ are normally stable. Investigation reveals that $M_{23}C_6$ tend to solution at about 1037^oC and the M_6C was found to be stable at higher temperatures, it does not solution until around 1148^oC or above [12].

2.4.13 The sigma phase

Sigma phases can be formed at long hours of exposure- hundreds of hours and they normally occur between temperature range of 760^oC and 898^oC. Some alloys that have been notably observed to form sigma phase include Udimet 700, Nimonic 115, and IN100. For some other alloys, exposure at temperature of 815^oC for a few hundred hours can result in extensive formation of sigma phase [12].

2.5 Hardening mechanisms of Ni base Superalloys

The superior strengthening mechanisms in Ni base Superalloys is achieved by either solid solution strengthening or precipitation hardening. Both mechanisms confer strength to the base alloy due to their interaction with dislocation movement and they will be discussed as follows.

2.5.1 Precipitation Hardening

As has previously been stated, the main strengthening phase in Ni base Superalloys is the intermetallic ordered γ' phase that precipitates in the matrix during cooling of the alloy through the solvus temperature. The strengthening is due to the interaction between the γ' phase and mobile dislocations in the matrix of the alloy. The movement of the mobile dislocation are impeded when they attempt to cut or by-pass the γ' precipitate. As such, a

larger force or stress will be required to overcome the γ' barrier thereby conferring strength to the alloy. The interaction, in general depends on the dimensions of the precipitate, its strength, spacing, and fraction present [19]. The finely distributed γ' phase represents an effective barrier to dislocation movement. The following important theories have been put forth to explain this interaction:

2.5.11.Long-range interaction of dislocations with precipitates.

Mott and Nabarro [20] recognized that the strain field surrounding a coherent, semi coherent and noncoherent particles can increase the yield stress of the material and act as sources of strengthening. The increase in yield strength is given by $\Delta\sigma \approx 2G\varepsilon f$ where f is the volume fraction of the dispersed phase and ε is the measure of the strain field. From the equation, it is clear that an increase in strain field (coherency strain field) will increase the yield strength.

2.5.12. Dislocation-Particle interaction, with and without particle shear.

There are several ways in which particles can act as barriers to dislocation. They can act as strong impenetrable particles through which the dislocation can only move by looping around the particles or act as coherent particle through which dislocations can pass, but only at stress levels higher than required to move dislocations through the matrix phase. Thus, the second phase particles either may be cut by dislocations or the particles will resist cutting and the dislocations will be forced to bypass them [20].

The size and the crystallographic orientation between the precipitate and the matrix can have two limiting cases:

(i) The precipitate particles are impenetrable to the dislocations. This is normally refereed to as the Orowan model. Orowan postulated that, for a dislocation to overcome an impenetrable second-phase particle, which intersects the slip plane of dislocation in a ductile matrix, it requires an additional stress to make the dislocation expand between the particles. When the stress applied is sufficiently high, the dislocation bows in between the particle, goes round it and leaving behind a loop around the particle. The stress necessary to cause dislocation to move by Orowan Model must exceed the sum of the critical shear stress necessary for overcoming the long-range barrier and the critical shear stress for matrix yielding in the absence of a precipitate. In cases where the stress required to cause particle shearing (Gb/x) is greater than the stress required to cause bowing, then the dislocation will move according to the Orowan bowing rather than shearing. This is the Orowan model of strengthening due to dispersion or precipitated incoherent particles. The increase in the yield stress due to the presence of the incoherent particles is therefore given as the sum of the critical shear stress necessary for overcoming the long-range barrier, the critical shear stress for matrix yielding in the absence of a precipitate and the shear stress required to cause dislocation bowing

$T_y=T_m+T_{LR}+Gb/x$……..[19]

After every bypass, one loop is added around the precipitate. The loops exert a back stress on dislocation sources which must be overcome for additional slips to take place. This will require an additional increase in shear stress and

hence an improvement in yield stress. The result of such continues bowing is that, the dispersed non-coherent precipitate will cause the matrix to strain-harden. This strain hardening can also add to the strength of the alloy. [20]

(ii) The precipitate particles are penetrable to dislocations: the particles are sheared by the dislocation in their slip planes. If the additional stress required in excess of $Tm+T_{LR}$ for particle shear is less than that required for bending the dislocation between the particles (Gb/x), then the particles will be sheared by dislocation during yielding.

$T_y<T_m+T_{LR}+Gb/x$…….[19]

Normally for yielding to occur, dislocations move in pair to cause the shearing of the particle. The first dislocation creates the anti-phase boundary and the second pair restores the order in the particle. On shearing, a dislocation step on one burgers vector high is produced at the particle-matrix interface as result of creating an anti-phase boundary. The new dislocation step will increase the surface area of contact. The creation of the extra surface area is accompanied with an increase in surface energy, which must be overcome by the applied stress for yielding to occur thereby conferring strength to the alloy. When the particles are sheared, there is little work hardening [20] .

2.5.13Variation of yield stress with aging time and precipitate size.

Figure 2.1 shows the effect of precipitate size on the strengthening mechanism in precipitated alloys. During the initial stages of aging, the small precipitates or coherent phase with the matrix will be sheared under plastic loading. When the first dislocation shears the precipitates, it creates an anti-phase boundary with an increase in energy in the particle.

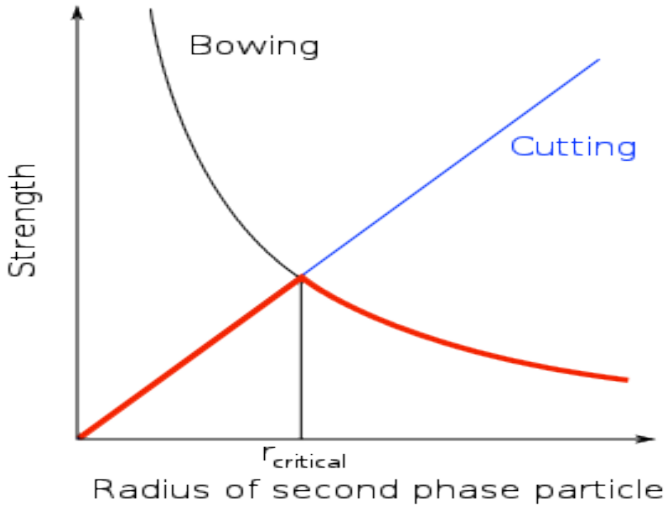

Figure 2.1 Variation of strengthening mechanism with increase in precipitate size [21]

If the Tshear>Torowan, then dislocation will be extruded through the particles and if Tshear<Torowan, the particle will be cut. Whether or not the particle will be sheared will depend on the particle size, the energy of the anti-phase boundary created and the

interparticle spacing. For coherent precipitates with low anti-phase boundary, only very small sized particles can be cut. With aging, the second phase particles grow in size such that, the average distance between them also increases and Torowan for dislocation bowing also decreases [19].

2.5.2 Solid Solution hardening.

When an edge dislocation is present in a material, it exerts a compressive stress above the slip plane and a tensile stress below the slip plane. The energy around the dislocation is high and dislocation mobility is relatively easy. With the presence of a substitutional or intersticial solute atom, this energy of the system is reduced making the dislocation mobility more difficult. For a substitutional solute atom bigger than the host metal atom, the change in volume due to the spherical misfit will be positive and would be attracted to the tensile side of the slip plane as the interacting energy there is negative. However, for a smaller substitutional atom, the change in volume of the system will be negative and would be attracted to the compressive side of the slip plane. In both ways the energy of the interaction between the dislocation and crystal will be lowered thereby reducing the mobility of the dislocation. A higher stress level will therefore be required to cause dislocation movement. It must be noted that, substitutional solid solution are only effective in pining edge dislocation, but screw dislocation are still free to move. However, for an intersticial type solid solution, the intersticial atom will normally distort the crystal structure to a tetragonal one which have the capacity to impede both edge and screw dislocations. The strengthening due to solid solution is most effective when the mobility of dislocation and that of the diffusing solute atoms are almost the same [19,20].

2.6 Welding

Welding is a very critical technique in the fabrication and repair of precipitation hardening (PH) Ni-base Superalloys. In an attempt to understand and control the weldability of these alloys, considerable research and development of the process have been conducted over the past 50 years. This led to the development of welding consumables that meet the ever increasing demand on the mechanical and oxidation properties of the welded joint [22]. Because of the high cost of replacement, normally repair is often a more economic choice. In many cases, the microstructure of the base alloy is altered during service, which prompts the use of repair methods different from the original fabrication of the base metal. For applications where post-weld heat treatments may be required to restore mechanical properties, cracking becomes a problem particularly in the γ' and γ'' strengthened alloys [22]. This section will look at the weld nomenclature and explore some weldability issues associated with repair of precipitation hardened Ni-base alloys, particularly on problems that are normally encountered during repair and post weld heat treatment. Precautions that can be taken to minimize these problems and ensure a sound repair joint will also be discussed.

2.6.1 Weld nomenclature

2.6.11The composite Zone

The composition of the majority of the weld bead during the process of welding comprises of the filler material diluted with the material melted from the base metal and the two are intimately mixed. The composition of this region will therefore be an intermediate between the filler metal and the base metal. As a result of difference in composition between the weld bead and the base material, its response to etching will be different from the base material, making the boundaries of the composite zone easily identified [23]

2.6.12 The unmixed zone

The unmixed zone is the region below the composite zone where there is no considerable evidence of mixing of the filler metal and the base metal. The existence of the unmixed zone is of practical significance in that; a careful examination of the HAZ cracks has been associated with the unmixed zone [23]

2.6.13 The Partially melted zone

The partially melted zone (PMZ) is the area adjacent the weld metal where liquation can occur during the welding. In the process of welding, usually the alloy is heated to a temperature range that lies within the liquid+solid region at point b in Figure 2.2, where there exist both liquid and solid phases. Below point “b”, at “c”, there exist no liquid and at point “a”, only liquid exist. After solidification at point “b”, that region is termed as partially melted region [24]

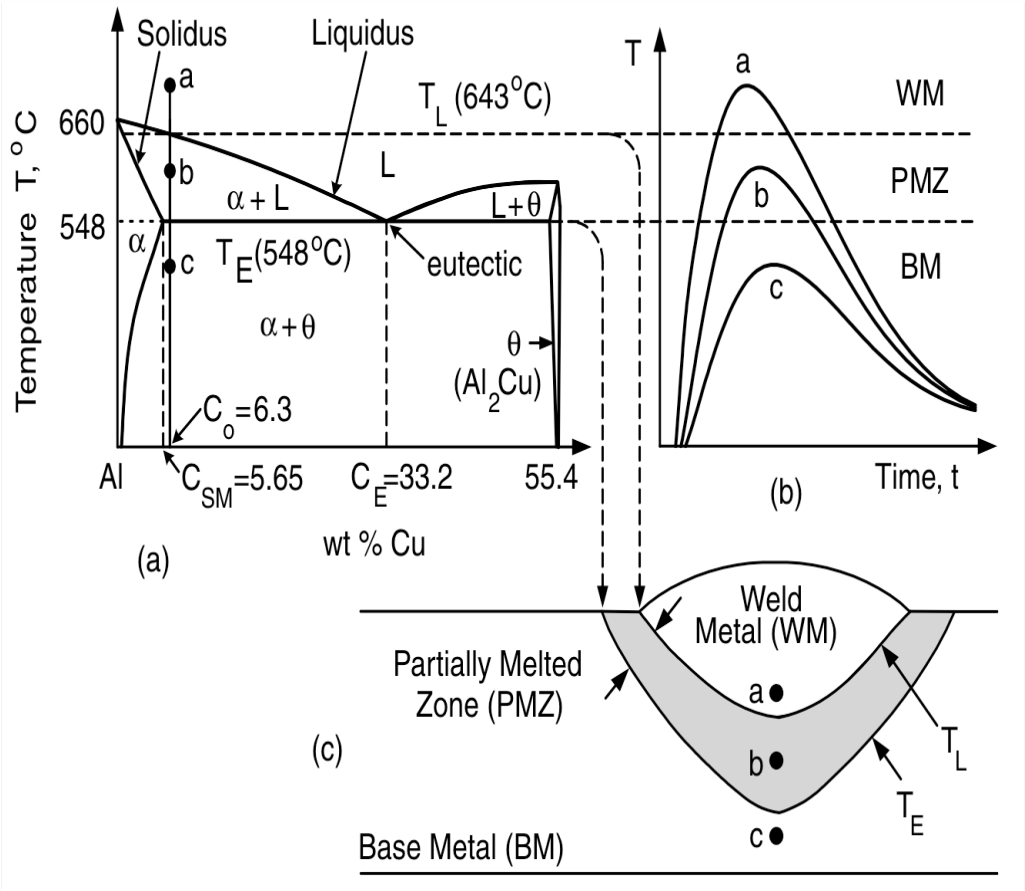

Figure 2.2 Weld nomenclature and the phase diagram [23]

2.6.14 The heat affected zone (HAZ)

The heat affected zone is the region beyond the fusion boundary such that any microstructural changes that occurs is entirely within the solid state. A wide variety of microstructure changes aided by thermal activation are possible depending on the alloys prior processing before welding and after welding. For example, there can be normal grain growth or recrystallization of cold worked materials. If it appears that the microstructural property of the as welded material will be seriously impaired, pre-weld and post-weld heat treatments can be carried out to minimize the damage [23]

2.6.2 Dissolution of precipitation and loss of strength in as weld-sample and post weld heat treated components of Ni-base Superalloys.

Using figure 2.3 below, we consider a case of the welding of a heat-treatable Ni-base alloy in the aged condition. Regions adjacent to the weld is heated above the precipitation temperature range of the γ' phase. Dissolution of the γ' ranges from partial dissolution near the edge of the HAZ at point 2 to full dissolution close to the fusion boundary at point 1. The γ' dissolution reduces the hardness or strength in the HAZ.

Owczarski and Sullivan[24] conducted some studies on the dissolution of the strengthening precipitates in the HAZ of Udimet 700 during welding. The material was in the full aged condition. In their results, they made the following observations; that the unaffected base metal consists of coarse angular γ' and fine spherical γ', typical of the prior-weld microstructure. The first stage of dissolution close to the weld interface and just inside the HAZ is characterized by the disappearance of the fine γ' and the rounding of the coarse angular γ'. Further dissolution of coarse γ' was observed in the middle of the HAZ. Since most precipitation hardening Ni-base Superalloys are highly alloyed with Ti and Al, the areas in close proximity to the dissolved coarse γ' become supersaturated with Ti and Al enabling finer γ' reprecipitating during cooling.

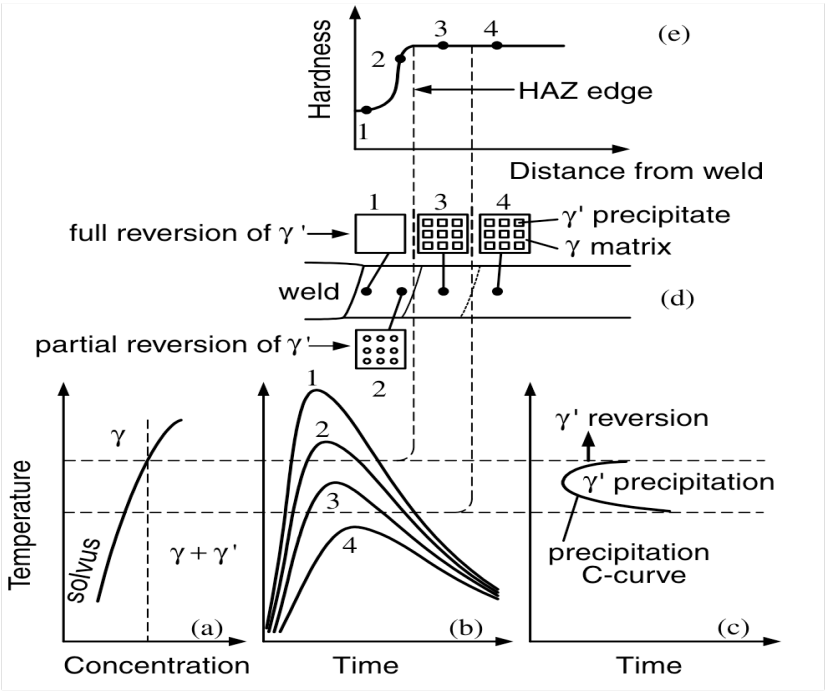

Figure 2.3 Dissolution of γ' phase during welding [24]

Dissolution continues toward completion as the fusion boundary is approached (Figure 2.3). The final dissolution and distribution of γ' occur in the weld metal itself. The weld metal contains a homogeneous distribution of fine γ' precipitate. It is further observed that reprecipitation of very fine γ' occurs in the region where coarse γ' has begun to dissolve during welding and was attributed to the precipitation of the elements that were taken into solution during welding [24].

2.6.3 Hardness Profiles

Figure 2.4 shows the hardness distributions of Inconel 718 laser and gas–tungsten arc welded in the as- welded condition. The hardness of the solutionized and laser-welded workpiece (Fig.2.4a) was not affected much by welding. The solutionized, aged, and laser welded work piece was observed to be softer in the HAZ. This is because of the dissolution of γ' precipitate in the HAZ and the fusion zone. The use of low heat input in laser weld produces a narrower HAZ than in the gas–tungsten arc. Maximum hardness of the weld was achieved, by an aging process, either aged after welding or solutionized and then aged after welding[24]

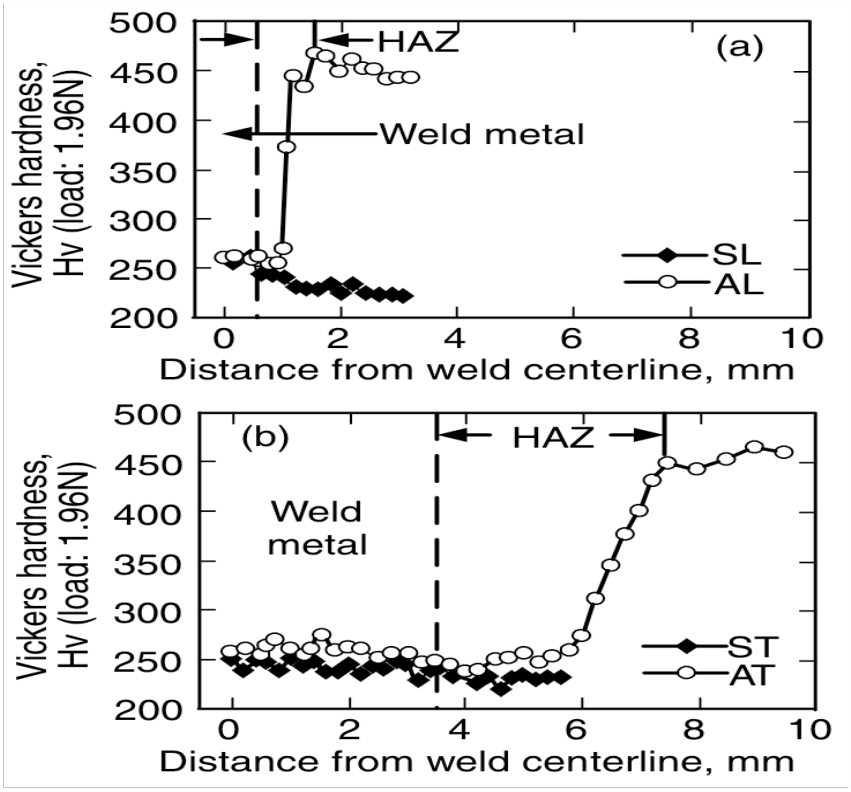

Figure 2.4. Hardness Profile of fusion zone, HAZ and the base material [24]

2.6.4 Welding Discontinuity/defects

Weld discontinuity can be grouped under three main categories namely, design related, welding process related, and metallurgical related. Design related discontinuities include wrong choice of weld joint for a given application and undesirable changes in cross section after welding. Process related discontinuity includes undercuts, slag inclusions, porosity, overlap, tungsten inclusions, shrinkage voids, lack of fusion, and lack of penetration, underfill and oxide inclusions. Metallurgical related discontinuities include cracks, fissures and segregation [25]

1. **Lack of fusion & penetration:** Lack of fusion (LOF) occurs when the degree to which the original base metal surface to be welded does not fuse sufficiently with the welding filler as illustrated in Figure 2.5, while lack of penetration (LOP) occurs when a molten metal is unable to sufficiently penetrate the base metal or when joint penetration is less than specified. In other words, lack of penetration is the degree to which the base metal is melted and re-solidified.

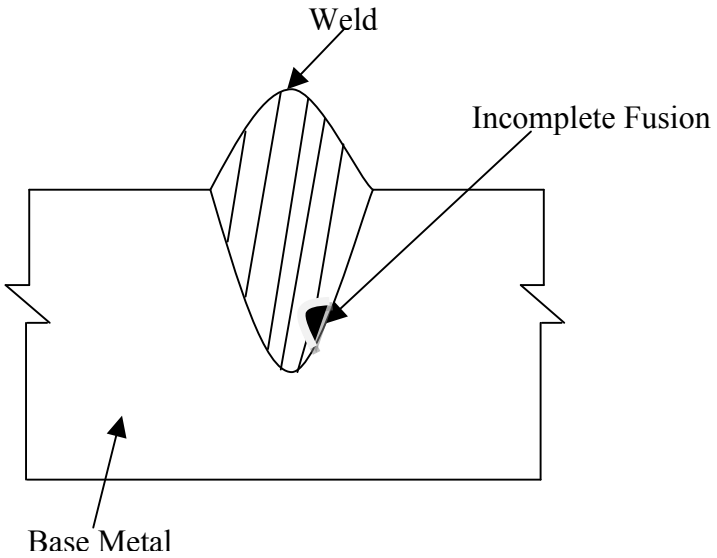

Figure 2.5 Incomplete fusion [26]

This is to say that, there could be a well fused joint but lack of root penetration. As such, LOF discontinuity are located on the sidewall while as LOP are located around the root of the weld. LOF normally occurs when excessive travel speed is used, excessive electrode size, insufficient current, and poor joint penetration. LOP may be as a result of low welding current, excessive travel speed, surface contaminant such as oxides which prevents the full melting of the base alloy. [26,27]. A defect therefore occurs which robs the joint of its full strength.

2. **Porosity:** Is one of the common weld defects in almost all the welding techniques. It does occur either on the surface or the interior of the weld. Gases that are trapped in the solidification pool of the weld cause this weld defect. In other words, the metal freezes before the gases have a chance to escape. The two main primary source of porosity include moisture and dirty wire/base metal[26]

3. **Undercutting:** Undercutting is a defect that appears as a groove in the parent metal directly along the edges of the weld. This type of defect is most commonly caused by improper welding parameters particularly the travel speed and arc voltage. Extremely fast solidification due to too high travel speed causes the bead to peak at its centre. The undercut groove is where melted base material has been drawn into the weld and not allowed to wet back properly because of the rapid solidification. Decreasing the arc travel speed will gradually reduce the size of the undercut and eventually eliminate it [26]. This weld defect is illustrated in Figure 2.6.

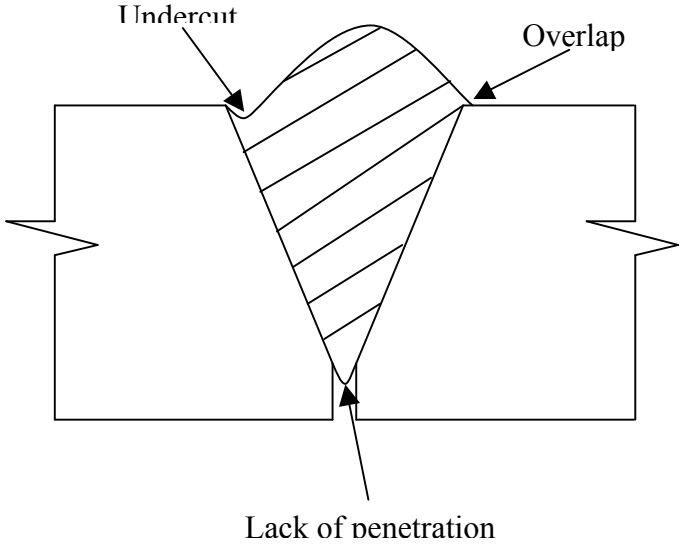

Figure 2.6 Welding defects [26]

4. **Cracking:** When the joint is under stress, it can crack and create a defect. These cracks can either occur at the top of the bead, within the weld or in the HAZ of the base metal. With appropriate pre and post weld heat treatment, cracking can be held to a minimum [26]

5. **Tungsten inclusion:** Tungsten inclusions are particles found in the weld metal from the non-consumable tungsten electrode used in GTAW. These inclusions are the result of exceeding the maximum current for a given electrode size or type, letting the tip of the electrode make contact with the hot tip of the electrode, using an excessive electrode extension, and inadequate gas shielding [25]

Some of these discontinuities do not render the welded joint unusable but defects will always have some adverse effect on the mechanical properties of the welded joint. For

example, the presence of porosity or lack of fusion between the weld joint and the base metal will reduce the fatigue properties of the repaired sample. However, an overlap or undercut can be grounded to size or shape when necessary.

2.6.5 Selected weldability issues with precipitated Ni-base Superalloys

Repair welding of Ni-base Superalloys is extensively used in the gas turbine engine industry in order to extend service life and avoid the high costs associated with the replacement of damaged components. Repair of rotating components is usually associated with turbine blade corrosion/erosion and is normally confined to the tips or edges of the turbine blades. The kind of repair techniques employed may include gas tungsten arc welding, laser beam welding, or brazing, to build up layers of material to restore the original shape of the component. In most cases a postweld heat treatment (PWHT) consisting of a solution anneal and aging treatment is then applied to restore the strength of the component. Ideally, the repair is made with a matching (or near matching) filler metal that will achieve the same strength and corrosion resistance of the base metal. In some cases, solid-solution strengthened filler metals are used for these repairs in order to avoid solidification cracking. One disadvantage of the use of solid-solution strengthened filler metals is that the repair weld cannot be hardened by heat treatment and the elevated temperature properties of the repaired component can then be compromised. Their use are therefore limited to the tip of the blades where there is zero stress. The static components of turbine engines are also subject to repair welding primarily due to fatigue cracking that ensues during service. These components must also be solution annealed and aged following welding to restore the desired mechanical properties.

Considerable research has been conducted on the repair welding characteristics of Ni-base Superalloys, particularly alloy 718 and Waspaloy which are widely used to construct static components in the hot section of aerospace turbine engines, since they are resistant to strain-age cracking. Most of these studies are focused on the degradation in weldability that occurs after multiple repair and PWHT cycles [22].

2.6.51 Postweld heat treatment cracking (PWHTC)

During postweld heat treatment of heat-treatable Ni- base alloys cracks do occur in both the fusion zone and the HAZ. The cracking phenomenon have been observed to be similar in most materials and may be applicable to other alloy systems.

1. Reasons for Postweld Heat Treatment

After welding of heat-treatable Ni-base alloys post-weld heat treatment is carried out to relieve residual stresses which may be harmful to the mechanical properties of the repaired component, and also to develop the maximum strength. Developing the maximum strength of the weld involves solutionizing with subsequent aging. The residual stresses in the weld are also relieved during the solution heat treatment. However, the problem arises during the temperature build up to the solutionizing temperature, with aging occurring in the weld before full solutionizing. This is because the aging temperature range is below the solutionizing temperature. Since aging occurs prior to the relief of residual stresses, cracks may develop during post-weld heat treatment. Such post-weld heat treatment cracking is referred to as strain-age cracking [22]

2.6.52 Development of Cracking

Figure 2.7 shows the path of postweld heat treatment cracking in a typical Ni-base Superalloy. Temperatures ranging from T1 to T2 are the precipitation temperature range. To relieve the residual stresses after welding, the work piece is heated up to the solutionization temperature (Figure 2.7b). During the heating profile, the alloy composition traverses the precipitation temperature range. With a very rapid heating cycle, the heating profile will miss intersecting the C curve and preclude cracking, otherwise cracking will occur (Figure 2.7c). Cracking after heat treatment usually initiate in the HAZ and notably on grain boundaries but not always the case [24].

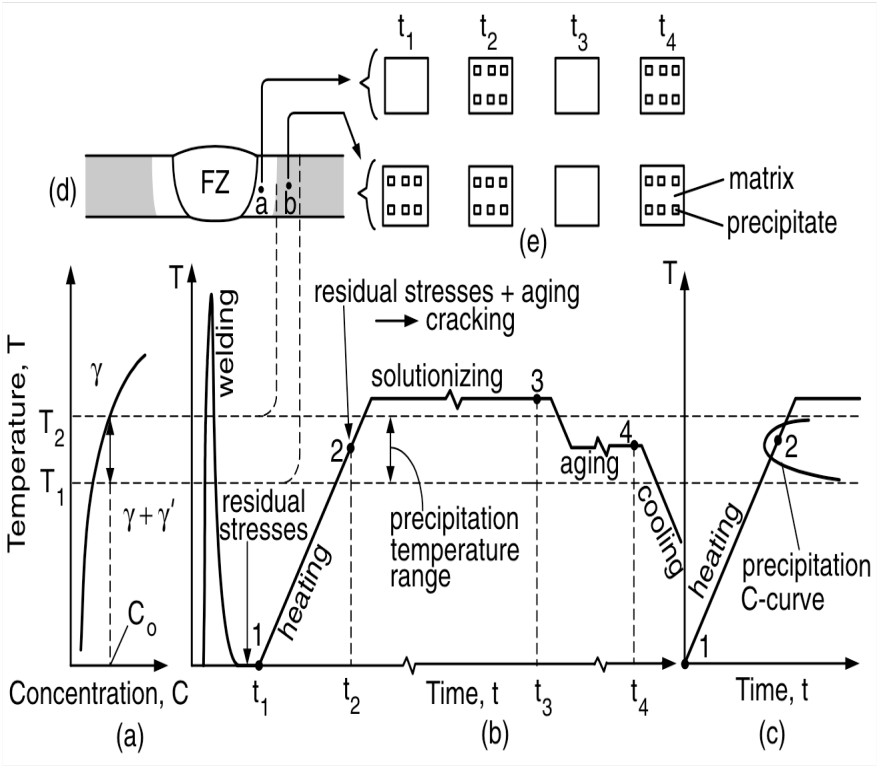

Figure 2.7 Strain age cracking [24]

2.6.53 Effect of Composition

The effect of Al and Ti contents on the postweld heat treatment cracking susceptibility in Ni-base alloys is shown in figure 2.8. From the graph, it is evident that the γ'-strengthened Ni-base alloys with high Al and Ti contents are difficult to weld due to the high susceptibility to cracking. This is because of rapid age hardening and their low ductility [24]. Similar results have been reported by Sidhu et al [28] where cast IN 738 given the University of Manitoba pre-weld heat treatment (UMT) was less susceptible to solidification cracking and postweld heat treatment crack due to more ductile base material compared to the conventional solution heat treatment. In another work by the same author in reference 28, high content of Al in filler alloy was reported to increase susceptibility to postweld heat treatment cracking in cast IN 738 [29].

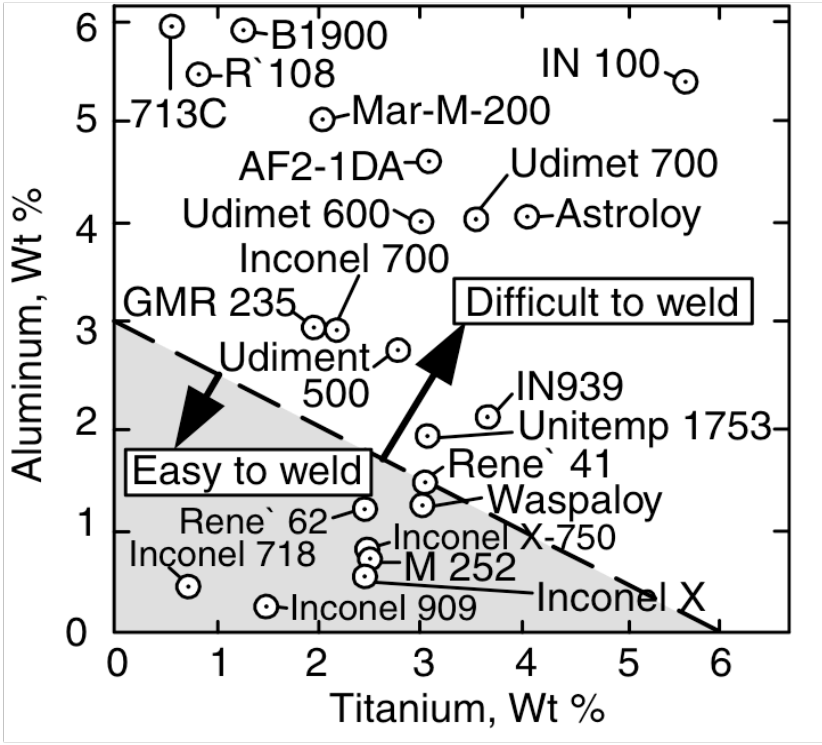

Figure 2.8 Effect of composition on cracking susceptibility [24]

2.6.54 Proposed Mechanism for PWHTC

Postweld heat treatment cracking in Ni-base alloys is thought to be as a result of low ductility coupled with high strains in the HAZ. A number of mechanisms have been proposed for the causes of low ductility in the HAZ, including, embrittlement of the grain boundary due to liquidation, and embrittlement of the grain boundary by oxides through oxidation reactions during heat treatment. Possible reasons assigned to the cause of high strains in the HAZ include welding stresses and the thermal expansion and contraction of the material. The precipitation of strengthening γ' phases in PH Ni base Superalloys results in contraction during aging. This aging contraction in conjunction with the embrittled grain boundary is speculated to be a contributing factor to postweld heat treatment cracking in heat- treatable Ni-base alloys[24]

2.6.55 Some suggested remedies

Avoiding post weld heat treatment crack is of utmost importance to the repair engineer. Various solutions to the problem have been recommended. Quite a number of these methods are based on experimentally observed crack susceptibility C curves. "A crack susceptibility C curve is a curve indicating the onset of postweld heat-treatment cracking in a temperature–time plot. It is usually obtained by isothermal heat treating of welded circle patches at different temperatures for different periods of time and checking for cracking" [24].

The lower end of the aging temperature range is characterized by relatively slow aging process and the occurrence of cracking approaches asymptotically with decrease in temperature. In addition, residual stresses are noted to relax at the higher temperature end of the aging temperature range and the occurrence of cracking approaches asymptotically at some higher temperature limit. In between the upper and lower asymptotic limits exists a minimum time, below which no cracking is possible and beyond which cracking is certain to occur. Aging of Inconel 718 was noted to be slower than the γ' strengthened Ni-base alloys. Consequently, C curve for Inconel 718 is to the extreme right of the C curve of Waspaloy, indicating the former's superior resistant to postweld heat treatment cracking. For applications where post weld heat treatment crack resistance is crucial, Inconel 718 must be considered. Practical limitations to the use of a single alloy for construction purposes exist and may require the use of other alloys to meet specific requirement. As such the following methods to reduce the cracking susceptibility are worth considering [24].

1. A multistep-type preweld overaging has been observed to significantly decrease postweld heat treatment cracking in alloy Rene 41. An overaged workpiece has better ductility and precludes severe residual stresses in the HAZ. However, during the welding process, the overaged precipitate go into solution in the HAZ and consequently the HAZ may still harden and age contract during postweld heat treatment. There appears to be controversy over the effect of preweld solution annealing. For example, Gottlieb[24] reported in his work that solution-annealed Rene 41 at 1080°C for half an hour and subsequent water quenching is more susceptible to postweld heat treatment cracking than

fully age hardened Rene 41 at 1080°C for half an hour, water quenched, aged at 760°C for 4 –16 h followed by air cooling. However, work done by Berry and Hughes [24], reported similarity in crack susceptibility for fully age hardened Rene 41 and solution-annealed Rene 41 during postweld heat treatment. For effective stress relief during post weld treatment with minimal or no cracks, the weldment must be heated rapidly before it has a chance to harden and age contract. Crack susceptibility reduces with increase in heating rate that can avoid intersecting the crack susceptibility C curve. The application of this method will be possible if the welded structure can be heated rapidly in a furnace with minimum distortions. [24].

Postweld heat treatment cracking can also be avoided by using vacuum or inert atmospheres for heat treatment. Since there is no oxygen present to embrittle the grain boundary during postweld heat treatment, the cracking phenomenon may be reduced. Modification of repair process such as using low welding heat inputs, the use of small grain-size materials, and controlling the composition of the alloy are other recommended techniques. Design trouble shooting such as Low-restraint joint designs may also limit cracking tendency [24].

2.7 Thermo-mechanical fatigue failure mechanisms in Ni base Superalloys

Thermo-mechanical fatigue (TMF) comprises of alternating temperature and mechanical cyclic strain independently, that leads to failure through complex interactions of fatigue, creep and oxidation. Fatigue test conducted under constant temperatures are known as Isothermal fatigue (IF) test. If a sample is held between two restricted ends subjected to thermal fluctuations, it undergoes an external compressive strain due to expansion, this is known as thermo-mechanical fatigue [30]. Practical situations involve pressure vessels, sudden breaks on railway lines and gas turbine engines that undergo start-ups and shut downs. Occasionally the term low-cycle thermal fatigue or low-cycle (LC) thermo-mechanical fatigue is used. A LC fatigue normally occurs at high strain cycle where the strain range falls within the inelastic region. This is the strain range where strain in non-recoverable and leads to fatigue damage. For all low cycle fatigue, the material undergoes damage in a finitely short number of cycles usually below 10,000 cycles. Thermo-mechanical fatigue usually falls under low-cycle fatigue. For instance, the sudden application of breaks on rail wheels occurs infrequently and this may occur less than 10,000 cycles during the life of the wheel. Similarly the thermal and mechanical strain excursions on turbine blades during start-up and shut-down during take-off and landing of jet engines is less than 30,000 cycles over the life of an aircraft [30]. Previous attempts have predicted TMF life components by approximating Isothermal fatigue life at the maximum temperatures of the TMF. Independent research by Nelson et al [31] and Malpertu & Reme [32] showed a strong correlation between the TMF out of phase (OP) phase and the IF but varies for the TMF in-phase (IP). This result was also collaborated by Bill et al [33] in his investigation of low cycle fatigue behaviour of alloy MAR-M200

over cyclic temperature range of 500-1000 ^{o}C. These results indicates that, the use of IF experiments for TMF life prediction is not a good approximation and requires modification for future predictive work. Different temperature and load cycle may also yield different life prediction results for the same alloy. A study of the TMF behaviour of Superalloy by Kuwabara et al [34] reveals that, loading wave form does affect the fatigue life of Superalloys at high temperatures. For instance in the said research, it was observed that TMF-IP had shorter life's compared to the TMF-OP loading at higher mechanical strain ranges. Bill et al [33] in their investigation of the TMF behaviour of MAR-M200, showed shorter lives for TMF-IP than OP. Other researchers [35,36,37] have backed this results in their findings, working on different alloys, which showed TMF-IP with severe damage compared to the OP with a crossover at lower strain. This cross over phenomenon was observed by Nelson et al [31] to occur at strain ranges less than 0.0045 in B-1900+Hf alloys. In the study of CMSX-6 single crystal, Mughrabi et al [38] showed that the TMF-IP exhibited longer life compared to the OP while as Marchionni [39] reported similar fatigue life for both temperature-strain cycle combinations within the scatter of data, thus, there is varying opinion on what wave form causes the most damage, and which best simulates the conditions for Superalloy applications at high temperatures. Because of the practical importance of TMF in real life engineering applications such as turbine blades, several scientific research have been devoted to failure mechanisms related to high temperature applications. In comparison to IF, the data base for TMF life prediction is very limited. This may be as a result of the complexity involved in the experiments, and the test still remains expensive. Several initiation mechanism do

interplay during TMF which accounts for the reduced life compared to the IF and will be discussed as follows.

2.7.1 Fatigue and fracture at elevated temperatures

Since the early works of Rosenhain and Ewen [40] there have been acknowledgement that metals undergo a transition from transgranular fatigue crack to intergranular fatigue crack at elevated temperatures [41]. When transgranular cracks occur, the grain boundaries stronger than the grains are unaffected while as intergranular crack occurs on weak grain boundaries. The term Equicohesive temperature (ECT) was coined by Jeffries, which was, defined as "that temperature at which the grains and the grain boundary have equal strength" [20]. Intergranular fatigue cracks occurs above the ECT and intragranular cracks below the ECT. Since the amount of grain boundary area decreases with increasing grain size, large grain size material will have higher strength above ECT compared to their fine grain counterparts. Below the ECT, the reverse is true [20, 42]

Ordinary ductile fracture initiated at inclusions and second phase particles can extend to elevated temperatures. In most practical situations, the fracture will occur during creep void coalescence, as such the stresses within the material/component tend to be lower than for ductile fracture. The voids, which lie roughly normal to the tensile axis, are formed as a result of grain boundary sliding which creates wedge cracks. At higher temperatures, and assuming that no other fracture mechanism is operating, the material will neck down to a point through an accelerated void nucleation and cracking called creep cavitations [20]

2.7.2 Creep

Creep is defined as the high temperature anelastic deformation by formation of voids under static loading [19]. It is usually characterized by the slow flow of material under constant tensile load with a corresponding decrease in cross sectional area. The material finally fails when an increase in stress due to small area bearing the same load exceeds the ultimate tensile stress. The temperature range through which creep becomes significant is $0.5Tm<T<Tm$ in Kelvin, as such, the temperature for creep may vary from each metal or alloy system [19]. Several mechanisms have been postulated to be responsible for the creep damage and they include: diffusion creep, dislocation creep, dislocation glide and grain boundary sliding.

2.7.21 Diffusion Creep

Diffusion creep normally occurs at low stress levels of $\delta/G<10\text{-}4$ but at very high temperatures. Nabarro and Herring [19] proposed that pre-existing vacancies within the grain migrate and agglomerate in regions close to the grain boundary. They are normally aligned in the direction of the applied stress in the lateral regions of the grain and causes an increase in the length of the grain. Coble also proposed that diffusion creep occurred by the diffusion of vacancy in the grain boundary instead of within the grains as proposed by Nabarro and Herring. This vacancy diffusion occurs at somewhat lower temperatures compared to Nabarro-Herring vacancy fluxing [20]. This eventually leads to grain boundary sliding [19]. In a similar work, Harper and Dorn concluded that diffusion creep occurs by dislocation climb which was later extended by Lemay as vacancy diffusion between sources and sinks [19]

2.7.22 Dislocation Creep

The stress range for dislocation creep is $10\text{-}4<\delta/G<10\text{-}2$ and it occurs by dislocation glide assisted by vacancy diffusion when an obstacle is to overcome. The earliest model for dislocation creep was advanced by Weertman based on the mechanism in which dislocation climb plays a major role. When an obstacle at high temperatures holds a gliding dislocation, diffusion of vacancies can cause the dislocation to climb, surmounting the obstacle and then proceed by gliding again until it meets another obstacle. The glide step therefore yields almost all the strain but the climb step controls the rate of dislocation motion. Since climb is controlled by the diffusion of vacancies and interstitials, the rate controlling step therefore becomes a function of the atomic diffusion [19].

2.7.23 Dislocation Glide

Dislocation glide normally occurs at higher stress level $\delta/G>10\text{-}2$ and occurs at all temperature levels. Kestenabach et al [19] concluded that climb is replaced by glide which is not dependent on a diffusion process, rather a thermally activated dislocation glide. The creep rate in this regime is established based on the ease with which dislocations are impeded by obstacles such as precipitate, solute atoms, and other dislocations [20]

2.7.24 Grain boundary sliding

At elevated temperatures, grain boundaries in polycrystalline metals and its alloys can move relative to each other. The sliding is a shear process usually promoted at high temperatures and low strain rate. Even though the largely accepted view of grain boundary sliding occurs as a bulk movement of the two grains, other observations also indicate that flow occurs in a softened area of finite distance into the grain from the grain boundary. The total contribution to strain due to grain boundary sliding is from a few % to as high as 50% [20]. Grain boundary sliding normally does not play any significant role during primary and secondary creep. However, in tertiary creep it does contribute to initiation and propagation of intercrystalline cracks [19]. Ashby and Verral proposed that the individual grains are translated by a combination of sliding and diffusional flow under the influence of the applied stress [19].

Frequently, more than one mechanism may be in operation simultaneously during high temperature creep deformation. If several mechanisms are operating in parallel, ie. operating independent of each other, then the steady state rate will be the summation of the entire individual mechanism creep rate and the fastest mechanism will be controlling the creep behaviour. However, if the mechanisms are operating in series, ie operating in sequence, then the total creep rate will be computed as the total inverse of the summation of the individual inverse of each creep mechanism with the slowest mechanism controlling the creep deformation[20].

2.7.3 Oxidation.

2.7.31 Oxidation fatigue interaction

Environmentally assisted fatigue failure mechanism in metals involve the interaction of a cyclic stress and am oxidizing environment. Such fatigue interaction with the environment is dependent on the relationship among loading, environmental, and metallurgical factors. It is generally reported that, for a given material, the fatigue strength (or fatigue life at a given maximum stress value) generally decreases in the presence of an aggressive environment. The severity of this failure mechanism varies widely, depending on a specific metal-environment combination. The environment may affect the probability of fatigue crack initiation, the fatigue crack growth rate, and in some cases both [27] during thermo-mechanical fatigue.

Fig.2.9 shows the effect of an aggressive environment on fatigue crack initiation of a material. The graph compares the smooth-specimen stress- life (*S*-*N*) curves obtained from inert and aggressive environments. Because as much as 95% of the structure life is spent on fatigue crack initiation, *S*-*N* curve comparison provides a good indication of the influence of environment on crack initiation. In the figure [Fig.2.9], an aggressive environment can promote crack initiation and can shorten the fatigue life of the structure [15].

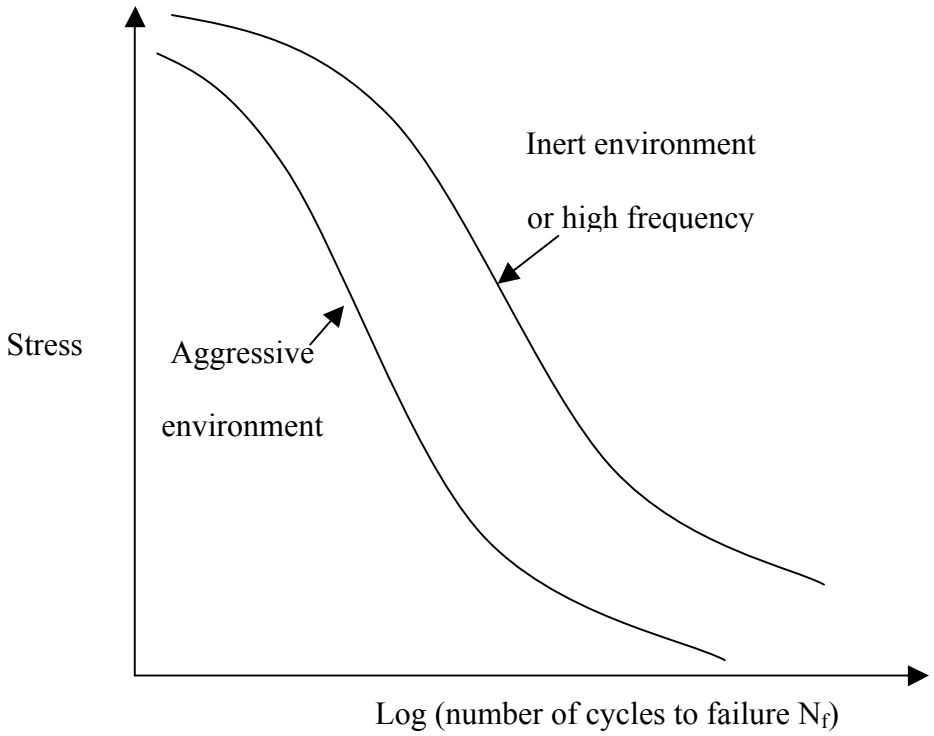

Figure 2.9 Effect of environment on fatigue properties of alloys [15]

Coffin [43,44] was the pioneer in the investigation of the effect of environment on mechanical properties of samples. At temperatures above 500^{o}C, brittle oxides are formed and aids in crack propagation into the specimen. The oxide layer undergoes mechanical strain as a result of the externally applied load or variations in thermal expansitivity of the oxide and the matrix [30].

K.B. Sankara Rao [45] reported in his study of high temperature low cycle fatigue (LCF) behavior of intermetallics that interactions between oxidation, creep and fatigue leads to drastic reduction in life. Similar results have been reported by Rodriguez and Mannan [46]. In their research, they also observed a significant decrease in fatigue life due to

oxidation interaction with fatigue damaging mechanism during LCF. The influence of the environment can usually be identified by the presence of oxidation products on fracture surfaces or within growing cracks. Oxidation products, however, may not always be present [27], depending on the frequency of the test.

2.7.32 Mechanisms of oxidation assisted fatigue failure

Interaction between oxidation and fatigue crack growth.

Neu et al along with H. Christ reported in their work [47,48] that in both IF and TMF conditions, oxidation played an important role in influencing crack growth. When the oxidation effect is dominant, the cracks grow by a combination of oxide-induced and fatigue crack growth mechanism. Such oxide-fatigue interactions increase crack growth rates and reduce the fatigue life of the specimen [47]. During cyclic loading, the surface oxides and surface coating impede the rapid movement of oxygen into the metal itself and prevent internal oxidation that exacerbates the cracking phenomenon and improves on the fatigue life of the component [49,50]. When these oxides get damaged, oxidation interacts with the cycling loading leading to the degradation of the alloy and decrease in fatigue strength. Various theories have been postulated for oxidation- fatigue interaction during TMF low cycle fatigue and some of these mechanisms will be discussed below.

A. Brittle fracture of oxide spikes ahead of crack tip.

During operation of component, damaged oxides exposes the bare metal to diffusion of atmospheric oxygen. The metal atom decomposes into a metal ion and an electron at the wall of the crack and also at the tip of crack. Diffusing oxygen atoms reacts with the

electrons and gets ionized. The oxygen ion then reacts with the free metal ion to form oxides. The anions that react with the metal ions at the crack tip forms very hard and brittle oxides. Sometimes these oxides are observed to be in a distance ahead of the crack tip called the plastic zone. This plastic zone is more susceptible to oxidation compared to the bulk crack length, a phenomenon normally referred to as stress assisted grain boundary oxidation (SAGBO)[51,52] Oxides found at the tips of crack during loading cracks by brittle fracture exposing new metal surface to the environmental damage. Oxygen continues to diffuse into crack openings forming the hard brittle oxides with subsequent crack and the cycle repeats itself.[47] In this theory, the oxidation is interacting with the cycling loading, aiding in the crack growth and reducing the fatigue life [52].

B. Voids formation leading to crack initiation.

D.A. Woodford [53] has shown that oxidation adversely reduces the creep properties of the Superalloy. It was observed during a lab experiment tested in an oxygen containing environment that, a lot of cavitations occurred on the grain boundaries and came to a conclusion that these internal voids grow in response to external oxidation processes.[53] These results were corroborated by other independent researchers [54] and concluded that exposure times to oxygen or air environment increased the depth of penetration of grain boundaries. It was observed in this same experiment that the grain boundary cavities were limited to the fracture areas in the unexposed test pieces whereas the exposed test pieces had grain boundary cavities in places away from the fractured region confirming the role of oxygen penetration to the formation of cavities.[54] The formation of these cavities led

to the reduced creep and fatigue life of the specimen. The depletion of gamma prime phase reduces the load bearing capacity of the cross sectional area which lead to early creep failure.[20] For an increase in oxygen partial pressures the creep properties of the specimen decreased with time and similar effect was observed for fatigue properties. Test carried out in air or oxygen atmosphere had lower fatigue life and strength properties. [54]

C. Embrittlement

Other researchers have also reported that embrittlement due to atomic oxygen penetrating grain boundaries and being located at the crack tip does influence the fatigue crack growth. [55] These effects are attributed to the diffusion of oxygen into the highly stressed alloy grain boundaries resulting in interface decohession and brittle intergranular crack propagation [46]. A schematic representation is shown in figure 2.10.

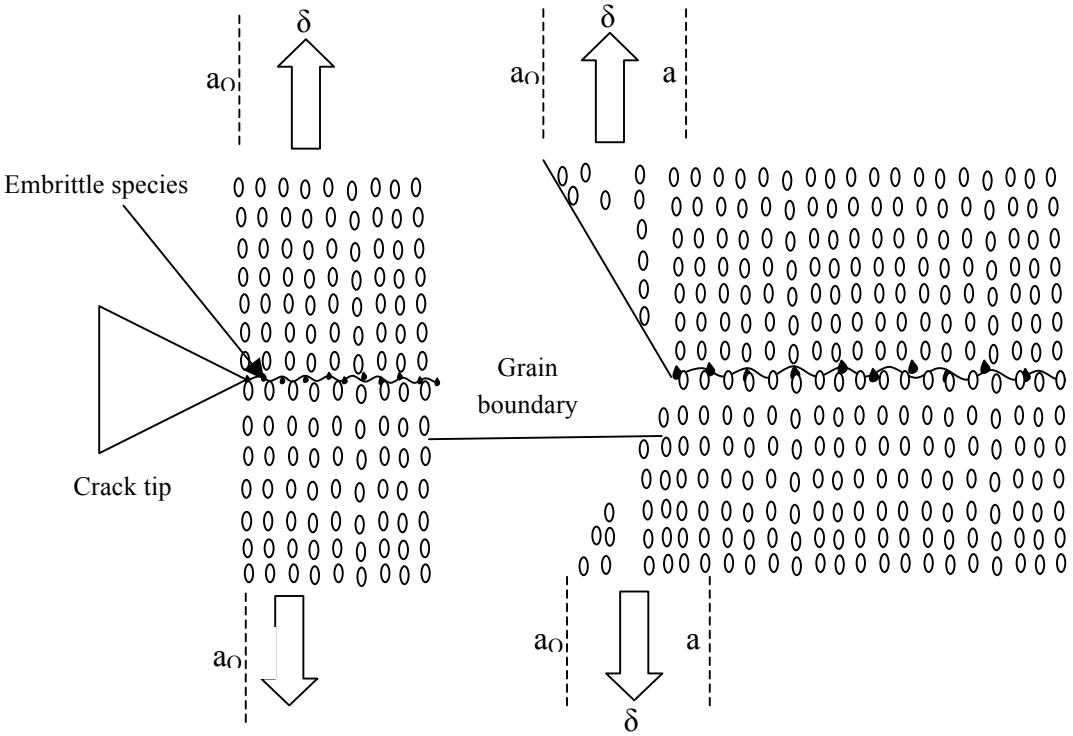

Figure 2.10 Grain boundary embrittlement [55]

D. Oxidation of grain boundary phases

Other environmental effect includes oxidation of grain boundaries, gamma prime and grain boundary carbides. [55] For example, it was observed in Nb containing Superalloy, that the oxidation of NbC particles near grain boundaries makes fatigue crack growth very sensitive to the environment. However studies conducted on alloy Rene 80 with a relatively high Cr% and less Nb showed less susceptibility to oxidation. [55] Investigation by Bhadeshia [11] revealed that additions of Hf and Ta significantly affected the fatigue crack growth resistance in many ways. It was noted that the removal of Nb present in some Inconel will remove the detrimental effect of NbC oxidation.

One explanation to the detrimental effect of NbC oxidation is that the products formed, which was termed Ti/Nb oxycarbide particles, have a relatively weaker interface with the matrix leading to early cavitations and corresponding fast failure.[56]

2.8 Scope of this work

All the references on alloys IN738 and Rene 80 mentioned above were concerned with LCF of the parent material in the solution treated and aged (STA) condition; however the economic necessity to extend the life of these very expensive components necessitates the development of generally fusion welding procedures such as gas tungsten arc welding (GTAW) and laser welding. Till date, comparative microstructural studies on failure mechanisms between the parent material and repaired material during thermo-mechanical fatigue is scanty and hardly researched into. The present research is concerned with microstructural failure evaluation of the TMF behaviour of the parent IN 738 and DS Rene 80 alloy STA, along with TMF of the simulated weld repair using IN-738 filler. The main objective of this research is to

1. Identify the failure mechanisms present in the repaired components for both polycrystalline Inconel 738 (IN 738) and Directionally Solidified Rene 80 (DS R80) during thermo mechanical fatigue (TMF).
2. Compare the thermo-mechanical fatigue life of baseline samples and repaired samples.

The study comprised of conducting thermo-mechanical fatigue test on the solution treated and aged base material to serve as the baseline for comparison. Similar test were conducted on the repaired samples and their fatigue life graphed. Microstructural studies were also conducted on baseline and repaired samples for both IN 738 and DS R80 alloys.

CHAPTER 3.0 Experimental Procedure

3.1 Thermo-mechanical fatigue.

The DS alloy Rene 80 and IN 738 were supplied by PCC Airfoils Minerva, OH, as approximately 250 mm x 50 mm x 10 mm thick investment castings, with the grains of R80 being in the <100> direction along the length of the casting. The castings were wire EDM'd using a Hansvedt EDM Model DS-2 traveling wire machine into test coupons 100 mm x 25 mm x 3 mm thick. Prior to welding, test coupons were overaged as per Thakur et al [57] at 1020°C for 16 hours. Gas tungsten arc welding was carried out at Standard Aero Ltd. on 3 mm thick coupons with a 45° v-shaped profile 1.27 mm deep. Welding was carried out at 60 amps at 76 mm/min using 1.14 mm thick IN-738 wire, and a wire feed rate of 203 mm/min. Tensile type test coupons were laser profiled to ASTM E8 dimensions being 100 mm x 25 mm x 3 mm and pin loaded [Fig.3.1]

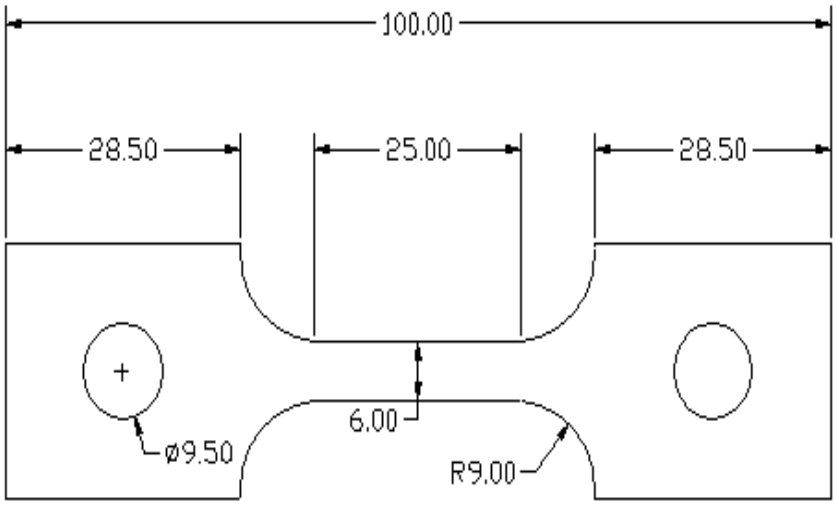

Figure 3.1 Tensile type test coupons for TMF test

For DS R80, post weld solution heat treatment was carried out in vacuum by heating to 1100°C at 50°C per minute and then in 50°C intervals to 1204°C; each temperature interval was held for 15 minutes, with a final time at 1204°C for 2 hrs. Ageing was carried out at 1052°C for 4 hrs and 843°C for 16 hrs, again in vacuum for DS Rene 80. The IN 738 alloy was solution treated at 1120^{o}C at 10^{o}C/min for 2 hours and then aged at 845^{o}C for 24 hours. The recast layer was subsequently removed by grinding and all surfaces prepared to a surface finish using 600 grit. Thermo-mechanical testing was carried out in air using a Gleeble 1500 model from DSI, Poestenkill, NY New York, USA, by raising the test material temperature from 500°C to 900°C in 25 seconds, holding at 900°C for 1.5 seconds and cooling to 500°C in 25 seconds and repeating the cycle. Set up for sample in Gleeble machine for the TMF test is shown in figure 3.2.

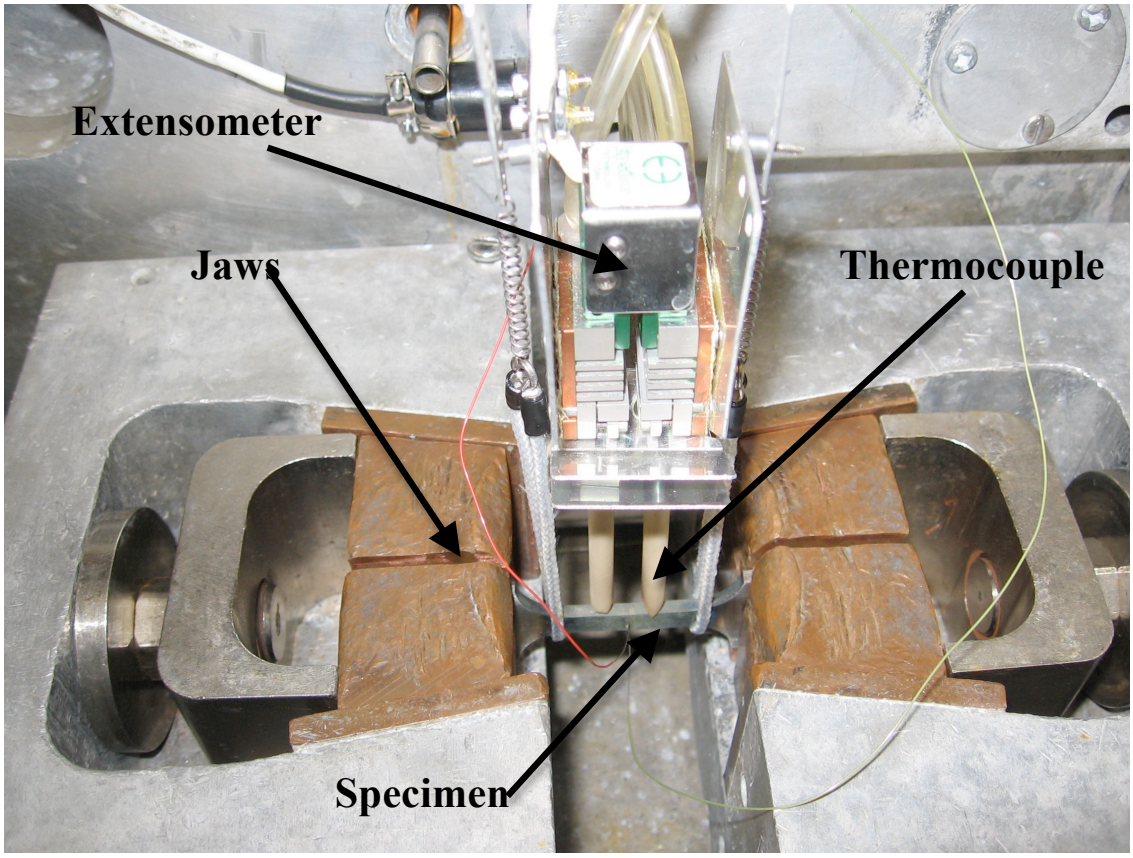

Figure 3.2 Fixture of the test coupon in the Gleeble machine

The test schedule used led to a frequency of test of 0.019 sec^{-1}. The short hold at 900°C was an attempt to minimize creep effect relative to fatigue behaviour. Temperature was monitored using Type K thermocouples. A personal computer was used in strain control with plastic strain values imposed on test coupons from 0.1% to 0.8% using an extensometer having two ceramic probes in contact with the test coupon. The plastic strain was applied independently, such that it attains its set point at 900^{o}C leading to an in-phase strain-temperature profile. Closed loop process parameter control was used for strain control in 250 cycle increments and then checked for cracks. The criterion for failure was to monitor the load drop until a visible trace showed a drop of 20 percent. At times complete failure of the test coupon occurred and at other times the tests were stopped with the test coupons showing a partly cracked gauge length.

3.2 Microstructure analysis

Fracture surfaces after the TMF test were examined using a Nikon SMZ800 optical microscope and JEOL 5900 SEM with an Oxford EDS system. Edges and fracture surfaces, especially at corners were evaluated and photographed for “thumbnail” type crack initiation areas. Sectioned representative samples of other halves were prepared for manual grinding and polishing by mounting them in black phenolic powder (Bakelite) . Specimens were ground on a manual grinder using successive finer grits of silicon carbide papers (240,320,400,600 and 1200 grit) with constant running water as lubricant. Polishing was then performed using an emery cloth embedded with 6 micron diamond suspension on a rotating wheel and a final polish on the 1 micron diamond suspension wheel until a final mirror-like surface was achieved. Subsequent cleaning using an

ultrasonic bath in methanol for 10 minutes was carried out to remove any residual diamond suspension during the polishing and dried with warm air. Mounted samples were analyzed both in the unetched and etched conditions. Etching for grain boundary evaluation was carried out using Marbles etchant (10g Cu_2SO_4 in 50mL H_2O and 50mL HCl, swabbing for 5 seconds) and for gamma prime observation using 12ml H_3PO_4/ 40 ml HNO_3 / 48ml H_2SO_4 at 6 volts for 3 seconds. Volume fraction analysis of porosity density using the Clemex^{TM} software was carried out using a 20X objective lens. Analytical techniques such as semi-quantitative point analysis using energy dispersive spectrometry(EDS), qualitative EDS line scans and mapping techniques were utilized to evaluate precipitates in the matrix, on the grain boundary and in the fusion zone. Electron microprobe analyses were performed on a Cameca SX100 electron microprobe, equipped with five wavelength-dispersive spectrometers with its source of electron excitation being a tungsten filament gun at the Geology Department, University of Manitoba. The electron microprobe was calibrated using known standards and backscattered electron imaging on the electron microprobe was used to locate the grain boundary precipitates. The major elements in the grain boundary precipitates namely Ti, Mo, W and Cr were analyzed using 15KeV and a lower acceleration voltage of 5KeV was employed to reduce the intensity of background interference and X-ray absorption for trace element boron and carbon.

CHAPTER 4.0 Results and Discussion

4.1 Base microstructure

4.1.1 Base Microstructure of IN738

The microstructure of the IN 738 alloy solution treated at 1120^{o}C at 10^{o}C/min for 2 hours and aged at 845^{o}C for 24 hours consists of both primary gamma prime and secondary gamma prime phases co-existing in the gamma matrix, normally referred to as bimodal distribution. Figure 4.1 shows the bi-modal distribution with coarse primary gamma prime particles, having sizes ranging from 0.7µm-2.6µm and an average size of 1.3µm. The coarse primary gamma prime was precipitated from the gamma matrix at high temperatures close to the solidus during casting [58] and solution heat treatment. The secondary gamma prime phase is very fine with size ranging from 0.1µm-0.3µm and an average size of 0.2µm. They are formed at relatively lower temperatures compared to the formation of the primary gamma prime. Elongated primary gamma prime phase with lengths ranging from 3.5µm-15.1µm and an average length of 6.6 µm [Fig 4.2] were located on some grain boundaries.

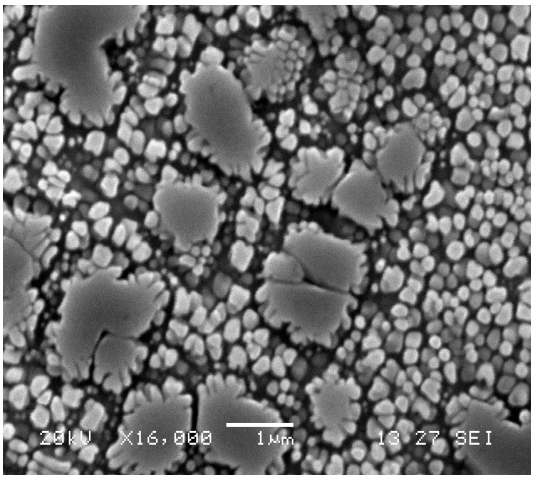

Figure 4.1 SEM micrograph, etched with γ' etchant, showing bimodal distribution of γ' phase

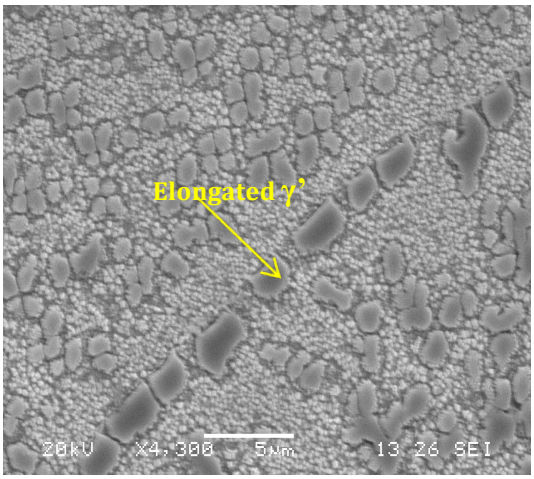

Figure 4.2 SEM micrograph, etched with γ' etchant, showing elongated γ' on grain boundaries

In addition, secondary solidification constituent such as γ-γ' eutectics [Fig 4.3] and MC type carbides rich in Ti were present. These secondary solidification products are normally formed in interdendritic regions from the last liquid to solidify during the last stages of the solidification. The MC type carbides had lengths ranging from 9µm-49µm with varying composition. Typical EDS semi-quantitative compositions of MC carbides can be found in appendix A. However, they show a marked peak in Ti.

(MC carbides and γ-γ' eutectics)-Xray mapping Technique

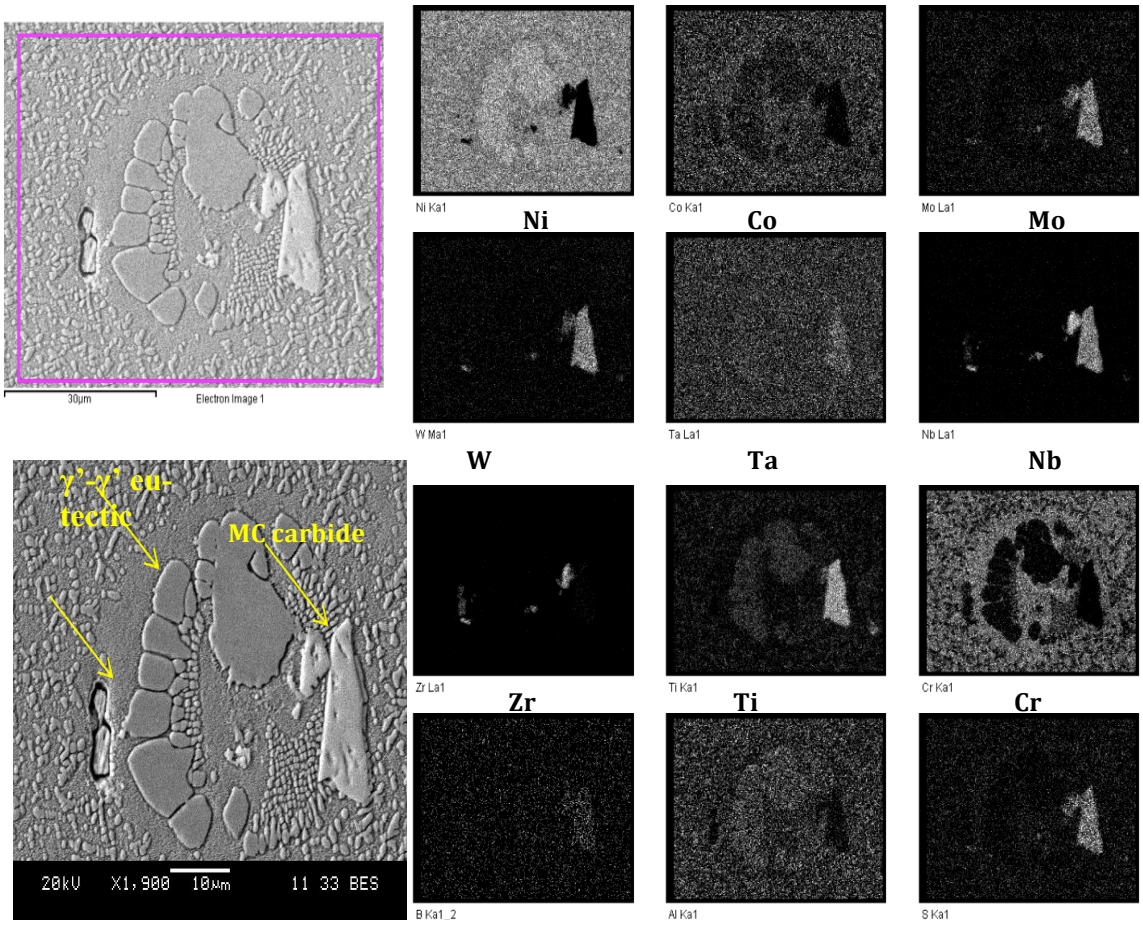

Figure 4.3 SEM Back scattered image

When etched with Marbles reagent the dendrite network was revealed showing interweaving dendrites oriented at different angles throughout the microstructure [Fig.4.4]. Porosity was also observed in the base material. The fraction of the porosity in the base material was approximated using the Clemex^{TM} software at 20X magnification to be 1%. [Fig.4.5]. The average grain size in the STA condition was 374 µm . Grain boundary precipitates notably $M_{23}C_6$ and M_6C were also observed. Other microconstituents such as Ti-Zr intermetallics, Ni-Zr intermetallics, M_2SC sulphocarbides and borides reported in other literature [58,59] were not observed in the present research.

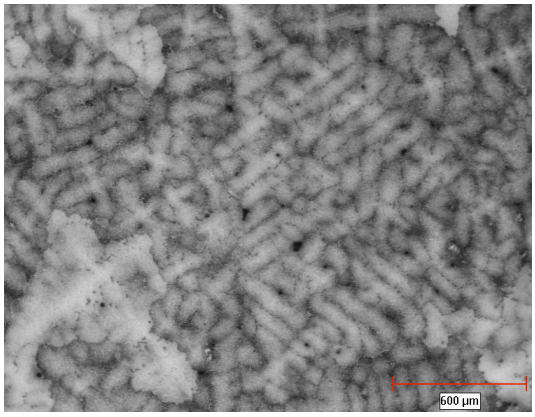

Figure 4.4 Optical micrograph, etched with marbles, showing dendrite network

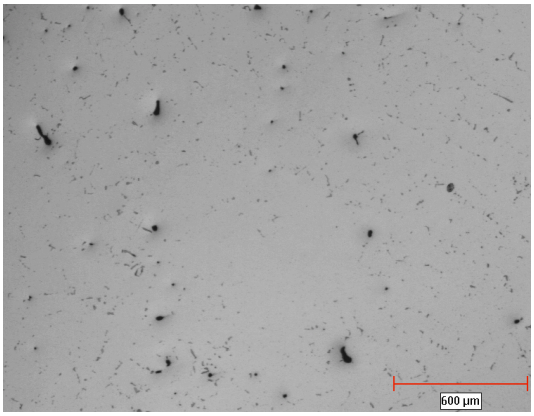

Figure 4.5 Optical micrograph, polished & unetched, showing porosity

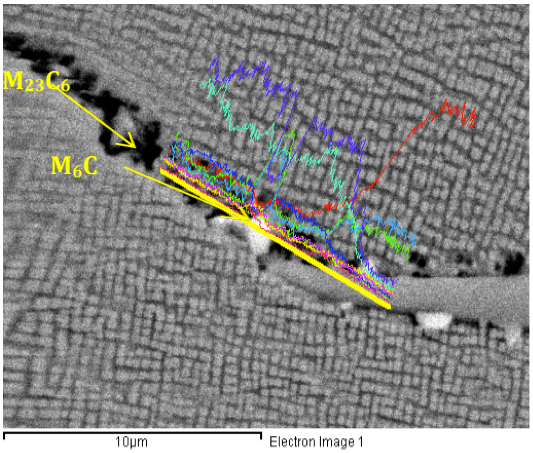

Figure 4.6 SEM micrograph, back scattered, showing $M_{23}C_6$ and M_6C or Boride

4.1.2 Base microstructure of DS R80

The microstructure of the DS R80 solution heat treated from 1100°C at 10°C/15min, raised to 1204°C, held for 2hours and aged at 1052°C/4hours + 843°C/16hours in vacuum shows directionally elongated dendrites [Fig.4.7]. Fine secondary gamma prime phase [Fig.4.8], with sizes ranging from 0.2µm -0.4µm and an average of 0.3µm was also observed. Table 4.1 summarizes gamma prime distribution in the base alloys. Approximate porosity density was determined to be 0.5% using Clemex™ software. The average grain size perpendicular to solidification direction in the STA condition was 554 µm.

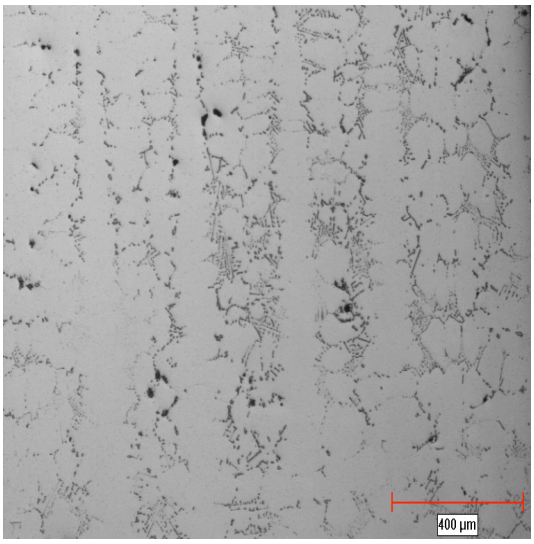

Figure. 4.7 Optical micrograph showing DS dendrites in Rene 80

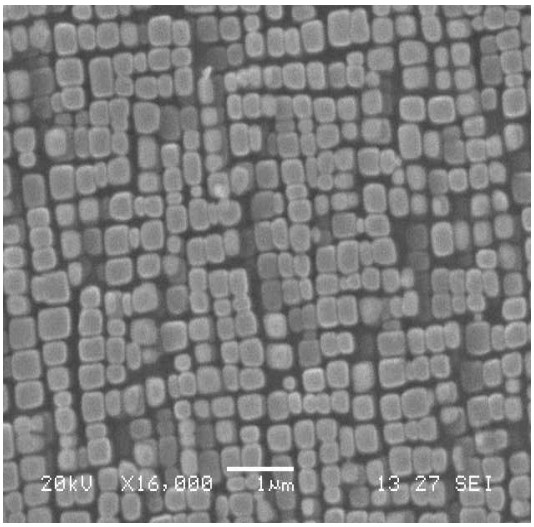

Figure 4.8 SEM micrograph, etched with γ' etchant, showing secondary γ' phase.

Blocky MC type carbides [Fig.4.9] of size length ranging from 5 -37 µm interspersed with long needle-like Ti rich particles, also MC carbides [Fig. 4.10] having length range of 16-62µm. were present. Tin et al [60] also reported the formation of blocky and scipt-

like MC carbides in Ni-base single crystal alloy. These carbides are usually formed in Superalloys during freezing as discrete particles, randomly distributed both in intergranular and intragranular regions. They are usually located in the interdendritic regions of the alloy. Some MC type carbides were cracked in the base alloy. Semi-quantitative EDS analysis of the MC type carbides are listed in Table 4.2 and appendix B.

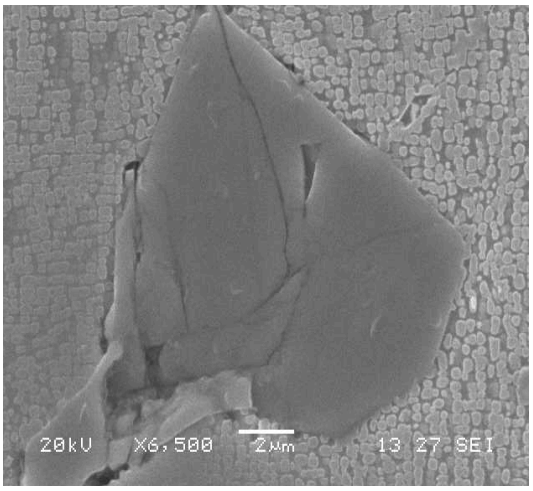

Figure 4.9 SEM, etched with γ' etchant, showing cracked MC carbides in base material.

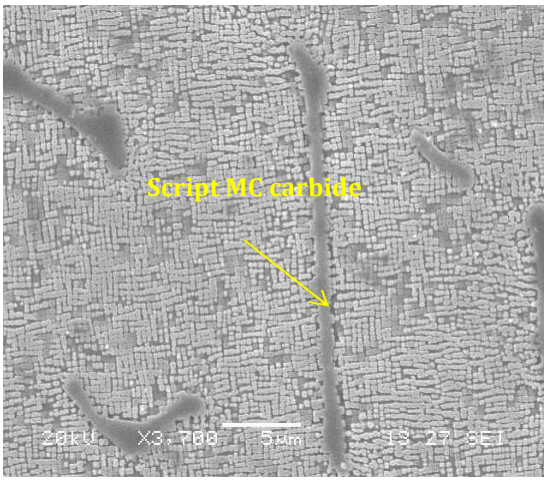

Figure 4.10 SEM micrograph, etched with γ' etchant, showing acicular MC

Grain boundary precipitates such as M_6C and $M_{23}C_6$ were also present on the grain boundary of the DS R80. Some of these precipitates were seen forming close to MC carbides. With appreciable amount of Cr and W, continuous film of $M_{23}C_6$ forms on some grain boundaries. Sims et al [3] reported that, MC carbides sometimes decompose at high temperatures to form $M_{23}C_6$ and M_6C. Fig 4.11, shows a spectrum rich in Cr, Mo and W, likely to be $M_{23}C_6$, with M = Cr, W and Mo and is in agreement with Sims et al [3] of approximate composition $Cr_{21}(Mo,W)_2C_6$.

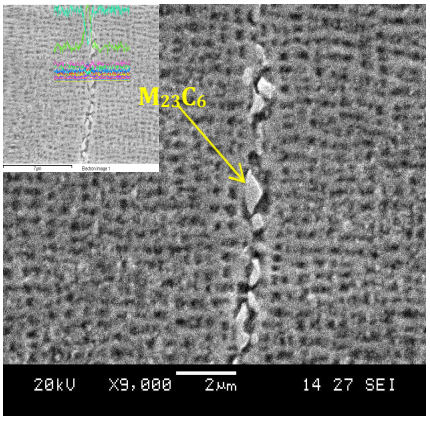

Figure 4.11 $M_{23}C_6$ on grain boundries showing Cr,W &Mo enrichment as $(Cr,Mo,W)_{23}C_6$

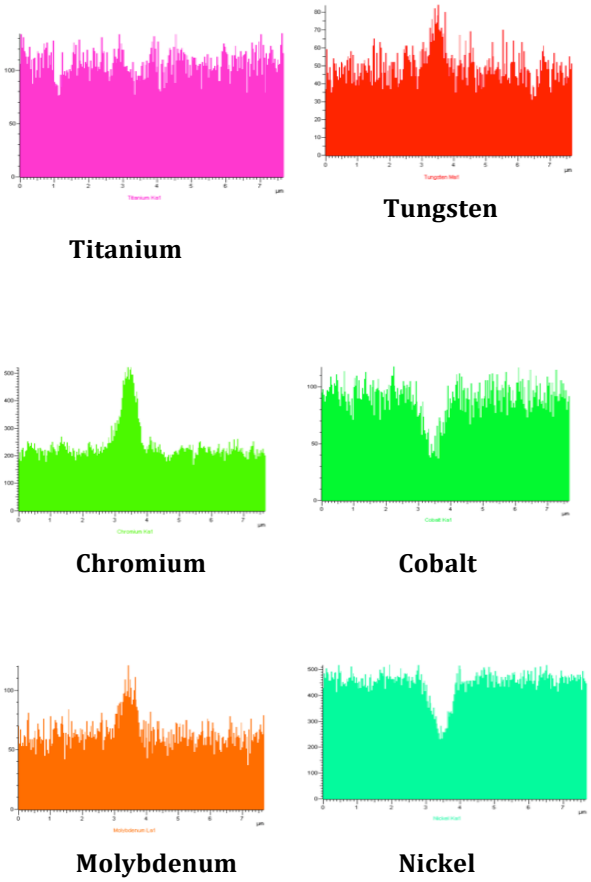

Fig 4.12 shows the presence of a grain boundary precipitate seen from the EDS line scan spectrum to be mainly Ti rich, likely to be MC and also a bright appearing precipitate in the back-scattered mode, rich in Mo & W possibly M_6C.

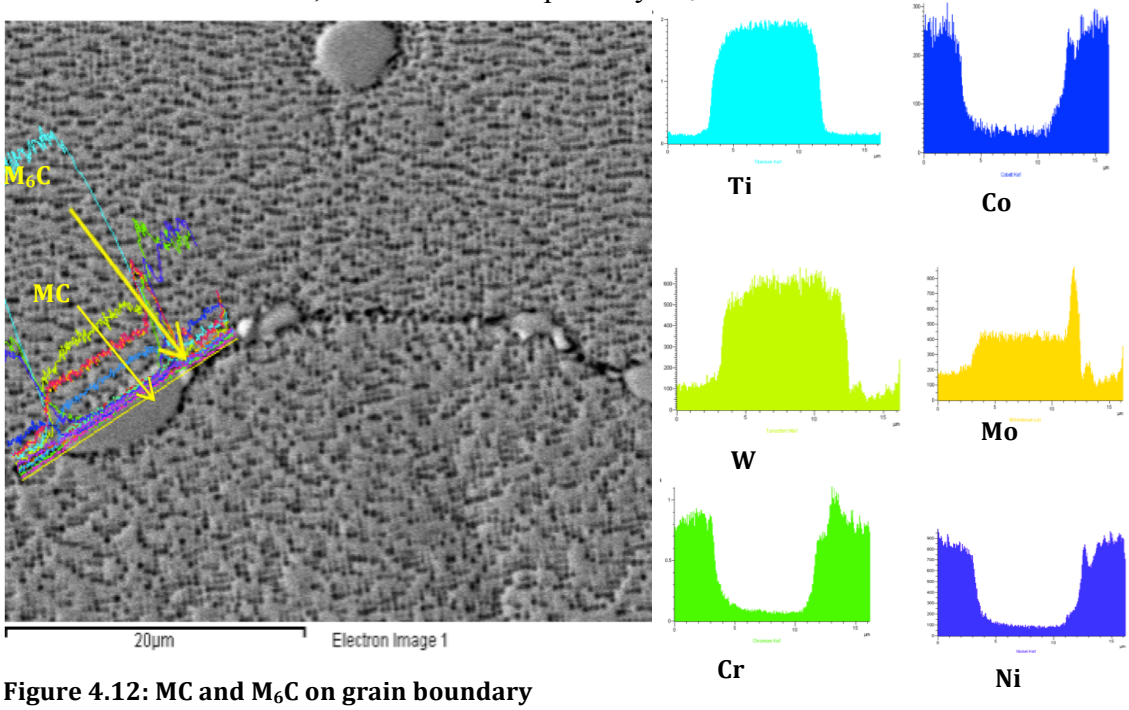

Figure 4.12: MC and M_6C on grain boundary

Figure 4.13 shows a back scattered electron (BSE) image of grain boundary precipitates. WDS mapping using electron microprobe (EPMA) show that, the bright particle labelled 1 had appreciable amount of Mo &W and was rich in carbon, thus a carbide phase and most probably an M_6C [Fig. 4.14 &4.15].

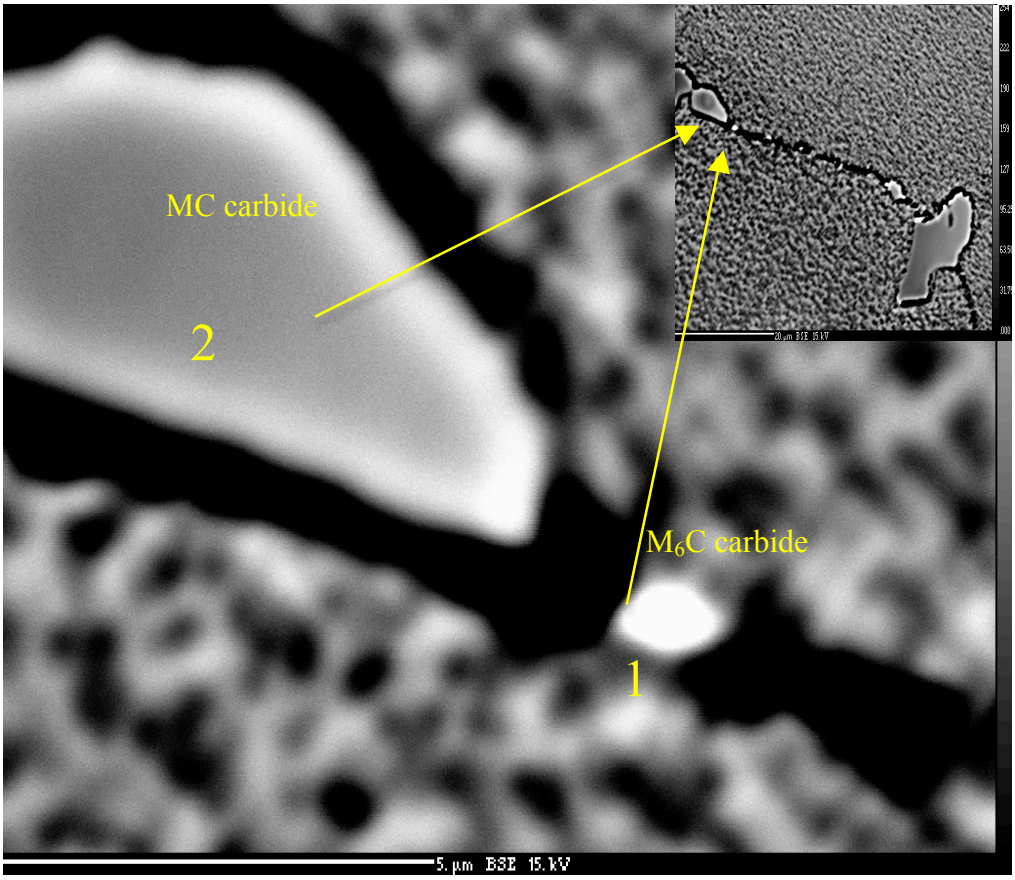

Figure 4.13 EPMA BSE, slightly etched with Marbles reagent, showing M_6C in close proximity to the MC carbide

One unexplained discrepancy in the mapping is the relative intensity of carbon in the MC carbide (particle 2) and the M_6C carbide (particle 1). The chemical weight percent of carbon in MC carbide assuming M to be Ti, will be calculated using molecular mass calculations. The atomic mass for Ti=47.867 and for C=12.0107. For an MC carbide, the

total molecular mass is mTi+mC=47.867+12.0107=59.8777. Therefore the weight % of C in MC carbide is (12.0107/59.8777) X100= 20.05, approximately 20wt%. If we assume M in the formula M_6C to be either W or Mo, we can calculate for the weight % of C as above. If M is Tungsten (W), then the weight% of C in M_6C will be 1.09 wt% and that for M being Mo will be 2.087wt%. As such, C was expected to be more concentrated in the MC carbide (particle 2) than the M_6C (particle 1). However, the mapping results show high concentration of C in particle 1. The inconsistency between calculated values of expected carbon concentration in the carbides and observed experimental carbon concentration from the maps throws some caution on the use of EPMA for carbon analysis. Thus, the identification of a phase using just chemical analysis may not be adequate and a crystal structure analysis using a Transmitted Electron Microscope (TEM) may be a complementary technique for final identification.

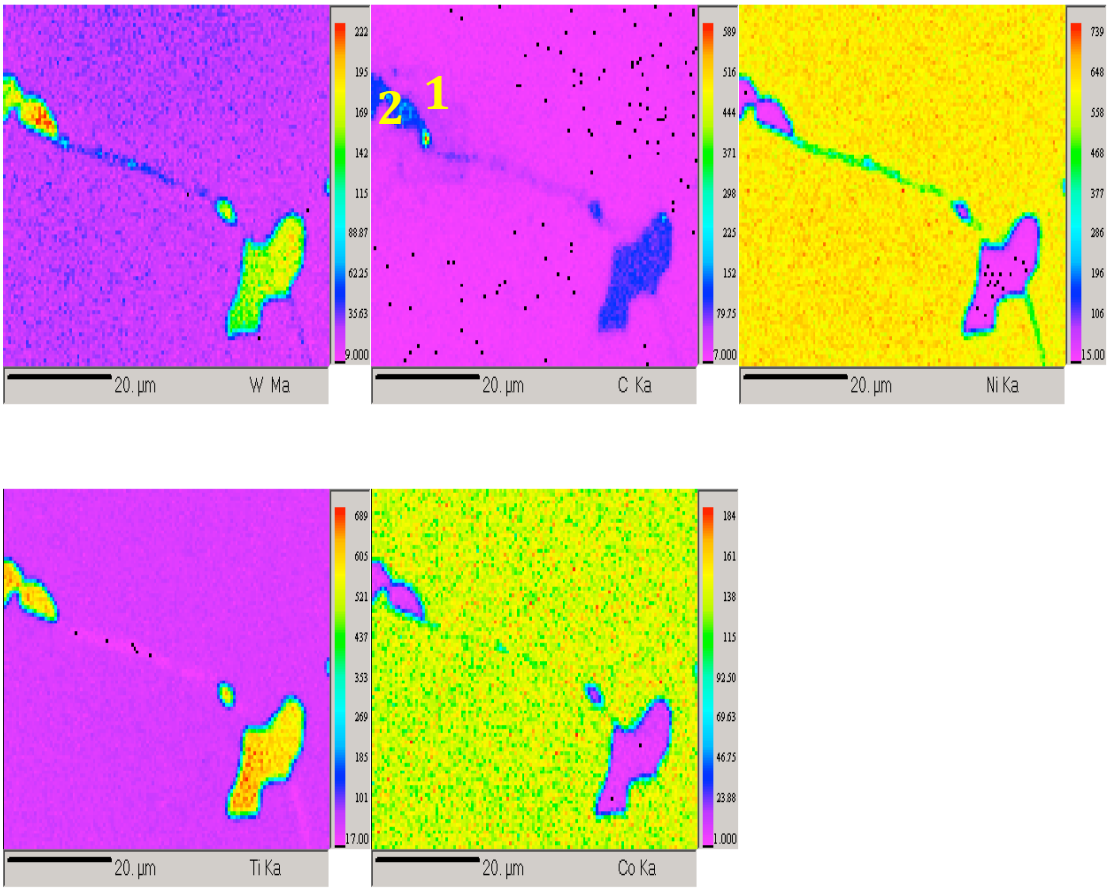

Figure 4.14 EPMA maps showing carbon concentration in particle 1

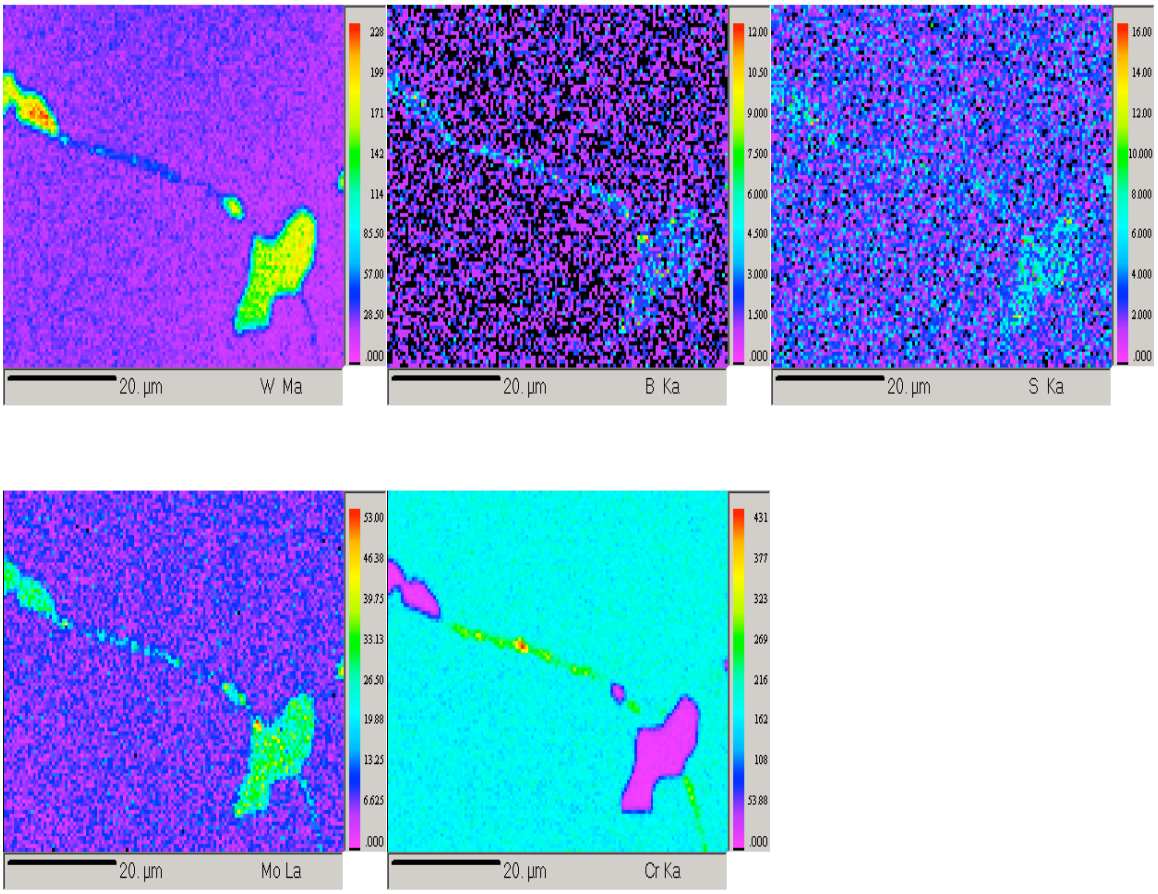

Figure 4.15 EPMA maps showing W peaking on particle 1.

Other notable phases in Ni base Superalloys such as γ- γ' eutectics, borides, Ni-Zr and Ni-Ti intermetallics were not found in the present alloy. Most of these phases which are normally located in the interdendritic regions were absent from the solution treated and aged (STA) DS R80 base material. Since they are non-equilibrium phases and are generally unwanted, they can be removed through appropriate heat treatment procedure. The presence of this non-equilibrium phases leads to incipient melting at low temperatures, which degrades the mechanical properties of the alloy. The absence of these non-equilibrium microstructures in the base metal suggests that, they possibly went into solution during the heat treatment.

TABLE 4.1 SUMMARY OF γ' PRECIPITATE SIZE IN BASE ALLOYS

ALLOY	Min/μm	Max/μm	Avg./ μm
DS R80 secondary	**0.2**	**0.4**	**0.3**
IN 738 primary	**0.7**	**2.6**	**1.3**
IN 738 secondary	**0.1**	**0.3**	**0.2**
IN 738 grain boundary	**3.5**	**15.1**	**6.6**

Table 4.2: SUMMARRY OF ALLOY AND MC carbides EDS chemical Analysis

Elements	DS R80 Base alloy wt%	IN 738 Base Alloy wt%	DS R80 MC at%	IN738 MC at%
Al	2.90	3.40	0.14	0.32
Si	0.004	0.004	-	-
Ti	4.98	3.44	70.07	44.09
Cr	14.10	16.02	1.61	1.36
Mn	<0.01	<0.01	-	-
Fe	0.18	0.03	-	-
Co	9.52	8.47	0.59	0.53
W	4.0	2.58	10.02	3.00
Mo	3.98	1.77	12.97	3.08
Ta	<0.02	1.71	0.10	14.55
Zr	0.028	0.028	0.75	0.19
Nb	0.02	0.90	0.68	27.08
Hf	0.02	<0.02	-	0.12
C	0.2	0.11	-	-
B	0.013	0.009	-	-
S	0.001	0.001	-	-
P	<0.015	<0.005	-	-
Ni	Balance	Balance	Balance	Balance

4.2 Weld Microstructure and Heat Affected Zone (HAZ) of IN738 & DS R80 alloy prior to TMF

The weld microstructure of the two alloys were mostly similar and will not be discussed separately. Primary MC carbides were located in the heat affected zone (HAZ) but were absent in the fusion zone (FZ) for both IN 738 and DS R80. Micro porosity [Fig. 4.16] and very fine particles of sizes ranging from 1.9µm-5.7 µm, also rich in Ti& W and having similar morphology as MC type carbides were observed in the interdendritic regions of the fusion zone for both alloys [Fig.4.17]. A line scan [Fig. 4.18] on these particles shows a peak in Ti & W and is further confirmation that, they are likely to be carbides of MC-type.

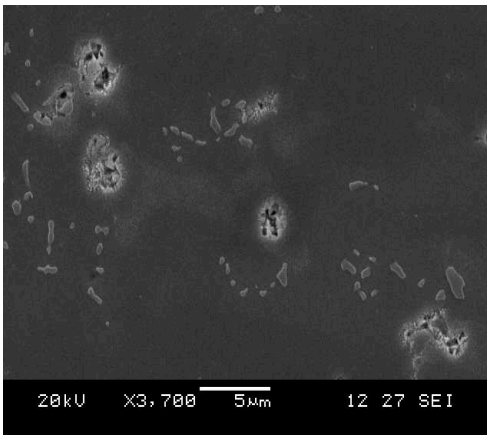

Figure 4.16 R80: SEM-EDS, showing microporosity & small Ti rich MC carbides on FZ

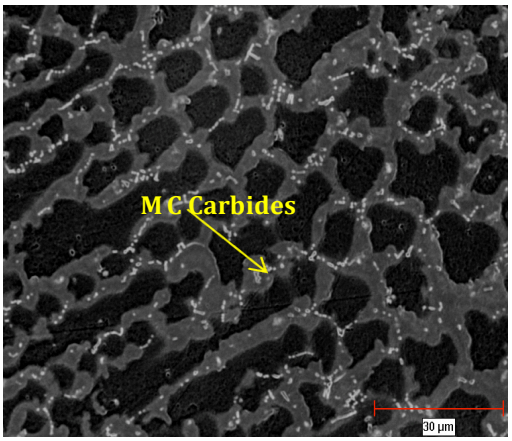

Figure 4.17: Optical micrograph, etched with marbles, Dark Field, showing interdendritic MC carbides in Fusion Zone

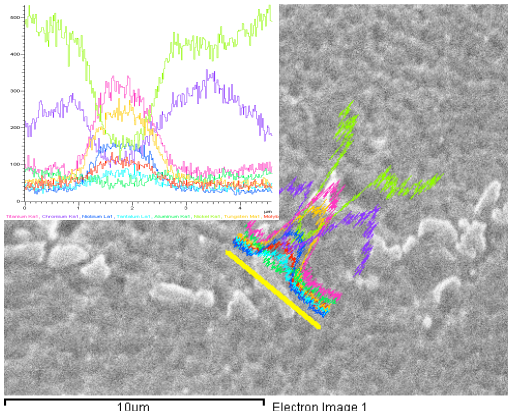

Figure 4.18 Line scan of interdendritic MC carbides in FZ showing a peak in Ti(Pink) & W(Orange)

Welding defects such as fusion zone cracking [Fig.4.19], and HAZ cracking [Fig. 4.20] were also observed. Typical dendrite feature of solidified products characterized both HAZ and FZ [Fig.4.21]. The dendrites in the HAZ which were formed from the solidification of the base material were larger compared to those located in the FZ [Fig. 4.22]. Typical FZ grain sizes for IN 738 and DS R80 were 52µm and 61µm respectively.

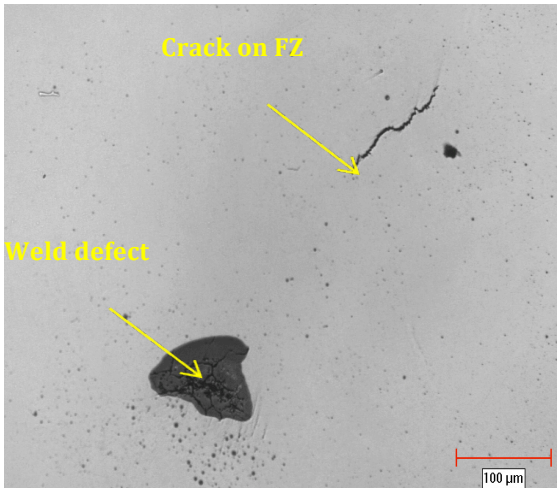

Figure 4.19 R80: Optical, showing weld defect

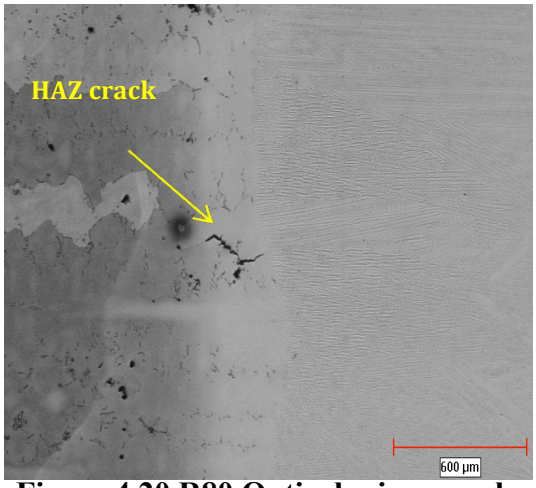

Figure 4.20 R80 Optical micrograph, etched with Marbles, showing HAZ crack

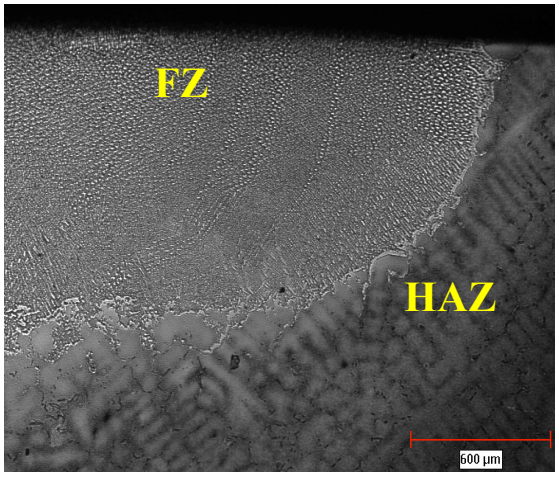

Figure 4.21 IN 738 Optical micrograph, etched with marbles, showing HAZ dendrites

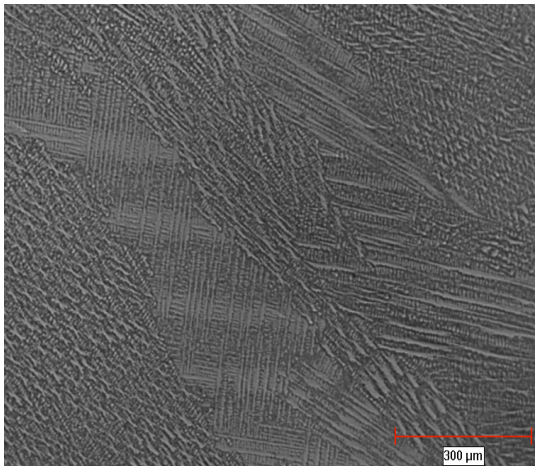

Figure 4.22 IN 738 Optical micro-graph, etched with marbles, showing dendrites in fusion zone

During solidification of the weld pool, two kinds of heat must be removed namely the specific heat of the liquid (SHL) and the latent heat of fusion (LHF) associated with phase transformation. When the cooling rate is slow as evidenced in equilibrium reactions, the temperature difference between the growing solid interface and the liquid pool is small. The latent heat of fusion is conducted from the liquid pool through the solid and into the base material. The solidifying interface is always colder than the weld pool because of the latent heat of fusion. For any solid to grow into the weld pool, it must be surrounded by warmer liquid pool having its temperature higher than the melting point of the growing interface. As such any solid growth into the weld pool will be stopped until all other part of the growing interface catches up. [61]. The heat in the solidifying pool will always be greater than the heat at the solidification interface and the solidification will then proceed in planar manner with uniform growth of solid into the liquid metal. [23] However, during practical solidification, equilibrium conditions are hardly achieved through out the whole solidification process. The heat profile during solidification is lowest when moving towards the centre line of the weld and the liquid metal ahead of the solidifying interface gets undercooled during solidification. Latent heat of fusion is therefore conducted from the solid interface into the weld pool. When there is a small protrusion on the solidifying interface, instead of melting, it rather conducts heat into the undercooled liquid and continues to grow and have branched network forming dendrites. When the solidifying weld pool continues to undercool, the dendrites start branching forming long columnar dendrites[61].

SEM images [Fig. 4.23-4.26] from the unaffected base material to the HAZ and then FZ show volume fraction of gamma prime phase decreasing in that direction. In the FZ, no evidence of gamma prime phase exist under the SEM after solution treatment and aging [Fig.4.23]. However, TEM analysis in other works [58] showed the presence of very fine gamma prime in the fusion zone after solution treatment and aging.

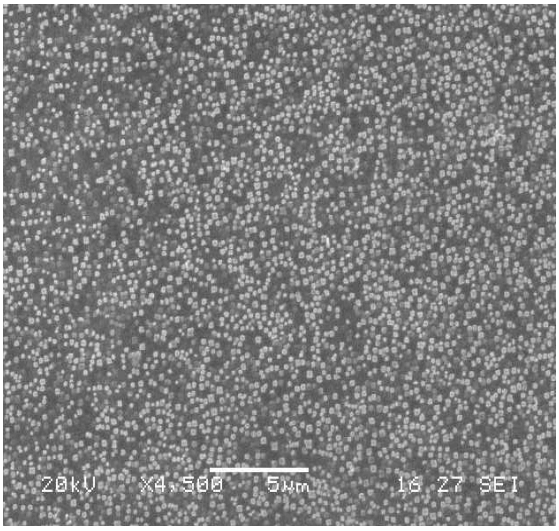

Figure 4.23 SEM micrograph, etched with γ' etchant, distance away from the FZ

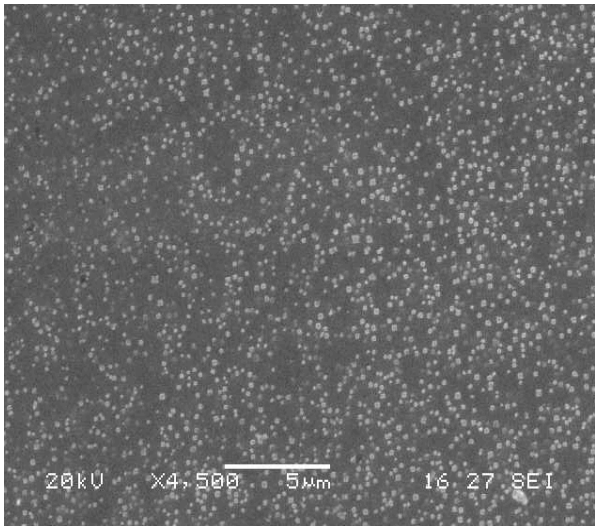

Figure 4.24 SEM micrograph, etched with γ' etchant, distance about 600µm away from the FZ

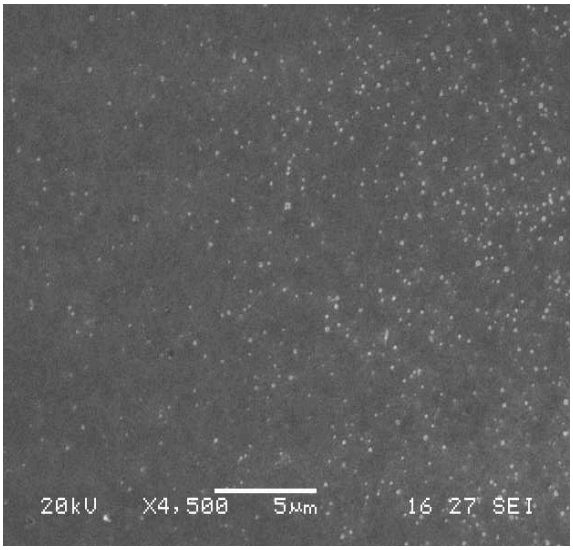

Figure 4.25 SEM micrograph, etched with γ' etchant, distance about 400 µm away from the FZ

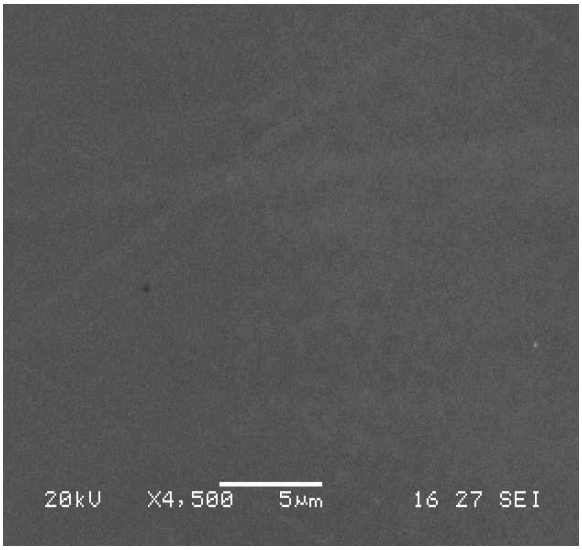

Figure 4.26 SEM micrograph, etched with γ' etchant, showing no γ' on FZ.

One variation in the characterization of the as-weld and heat treated IN 738 and DS R80 alloys was the phenomenon of recrystallized grains. In IN 738, there was recrystallization [Fig.4.27] in the as-weld and heat treated sample. The grain size of the recrystallized region for IN 738 prior to TMF was 29 µm. However, for DS R80, there was no evidence of recrystallization [Fig. 4.28] in the as-weld and heat treated condition.

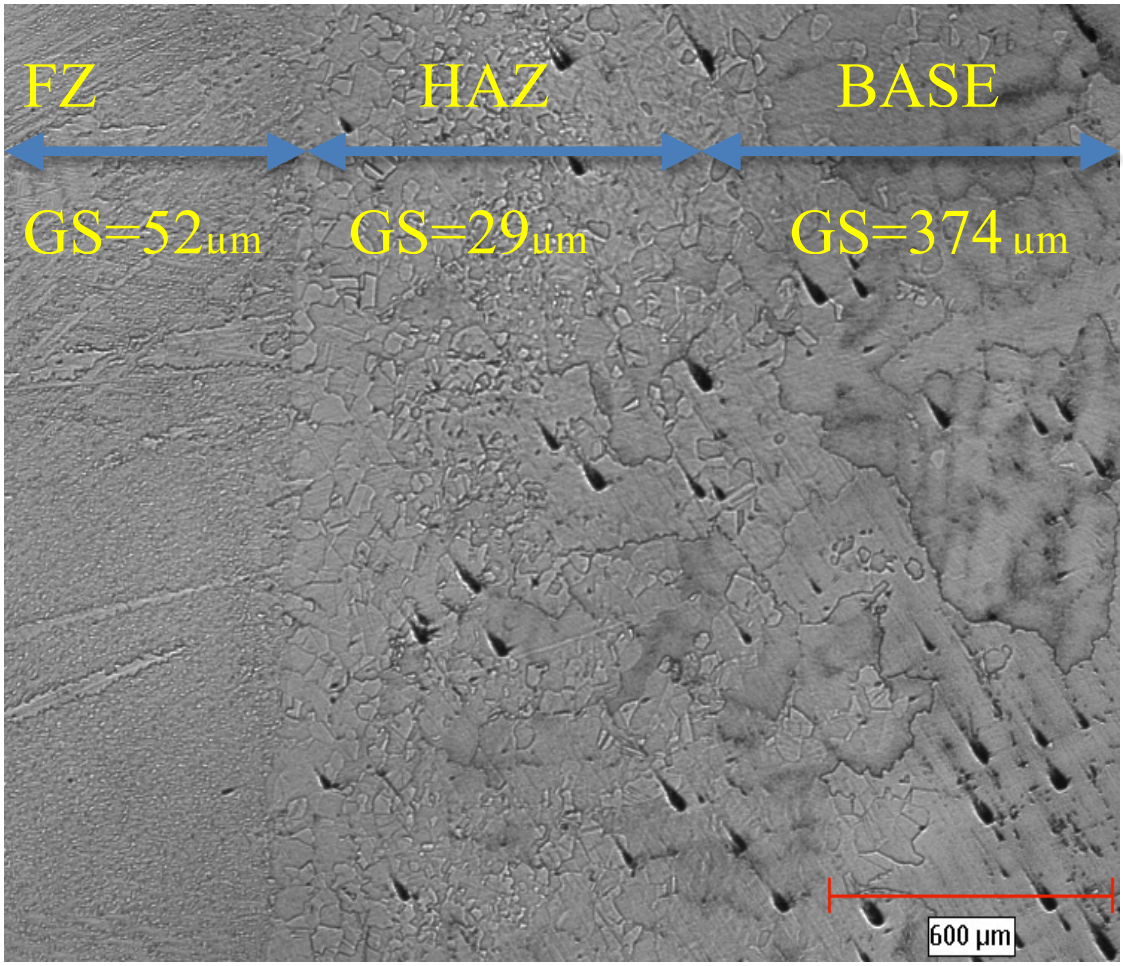

Figure 4.27 IN 738 Optical micrograph, etched with marbles, showing recrystallized grains in HAZ

GS=grain size

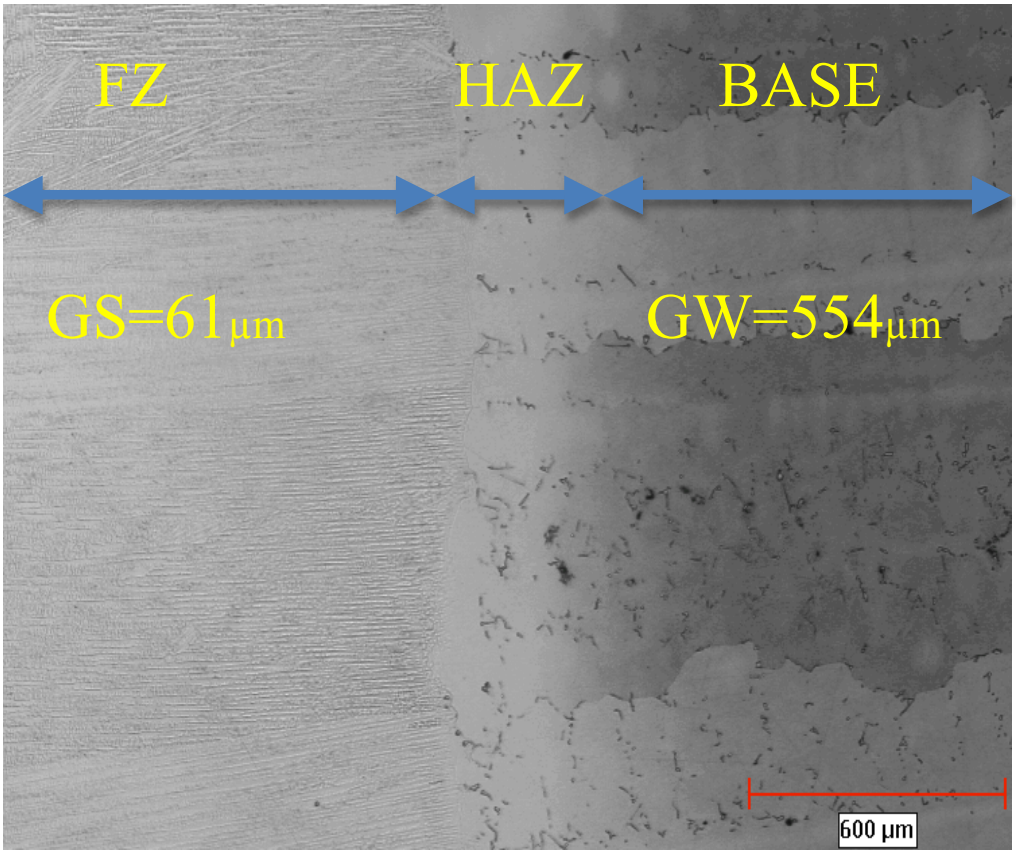

Figure 4.28 R80, showing no evidence of recrystallization after welding

4.3 Thermo-mechanical fatigue data

Mason [62] and Coffin[63] independently established a relationship between the plastic strain range and life of a component for LC fatigue test. This relation was to be known as the Coffin-Manson equation $Nf^{\alpha}X\Delta\varepsilon_p=C$ [30]…….(2)

Where Nf is the number of cycles to failure, ε_p is the plastic strain range and C and α are material constants. A plot of ε_p on a log vertical axis against log Nf on the horizontal axis yields a straight line relating the plastic strain range to the number of cycles to failure.

TMF results for DS R80 sample

Table 4.3 shows the TMF data for both baseline and repaired (GTAW) samples. Figure 4.29 shows the Coffin-Manson power law relationship where the applied plastic strain values are plotted against the number of cycles to failure for the STA and GTA welded and STA, fatigue tested at strains of 0.2 to 0.8%. As the plot in fig. 4.29 indicates, the higher the magnitude of plastic strain sustained by the sample, the smaller number of cycles the material is able to undergo before failure. The plot of thermo-mechanical fatigue data for DS R80 shows that the repaired samples had comparatively inferior fatigue strength and fatigue life properties to the base line samples. At a fixed strain %, for example, 0.5% traced on the graph, the total number of cycles to failure for the base alloy was approximately 5,200 cycles and that for the repaired (GTAW) was approximately 400 cycles showing superior fatigue life for base line over repaired sample. At a given number of cycles to failure, the base alloy can be used at higher damaging plastic strain compared to the repaired samples. If a components fatigue life is

fixed at 4,000 cycles, the repaired sample can be operated within a safe plastic strain of 0.4% and below whereas the base alloy can go almost up to 0.6% of damage strain. The base alloys therefore show far more superior fatigue strength compared to the repaired sample.

Table 4.3. R80 TMF values for Baseline and GTAW samples.

STA Base Line		**STA GTAW**	
Strain %	**No. of cycles to failure**	**Strain %**	**No. of Cycles to failure**
0.4	**7334**	**0.2**	**10000**
0.6	**2900**	**0.4**	**2360**
0.8	**148**	**0.45**	**1000**
0.8	**257**	**0.6**	**175**

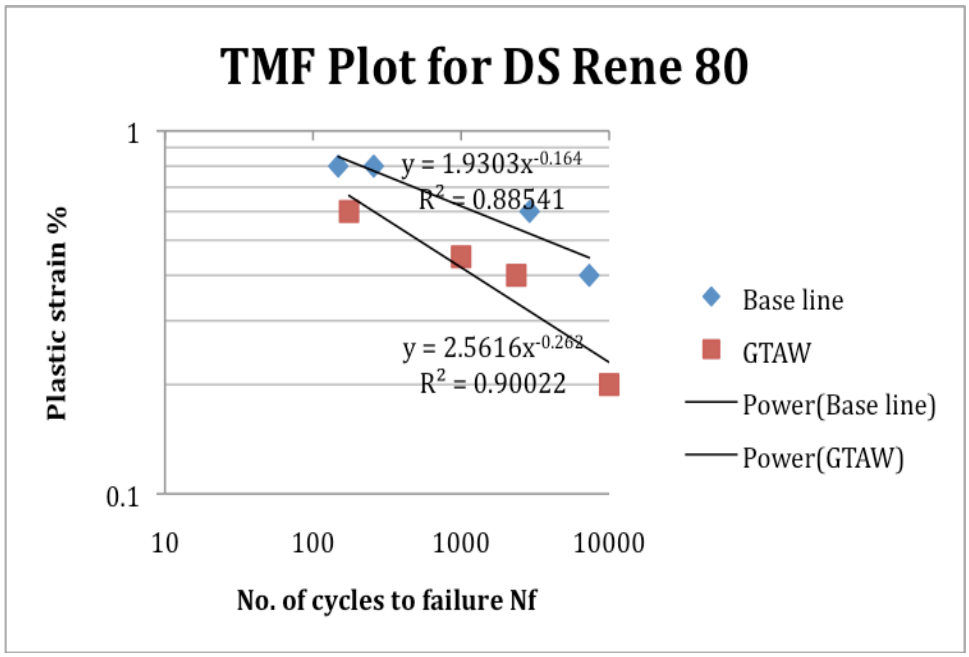

Figure 4.29 A plot of R80 TMF data for both baseline and repaired samples

TMF results for IN 738

Results from the gleeble thermo-mechanical fatigue test for IN 738 are recorded in Table 4.4. The plots in fig. 4.30 show no evidence of superior fatigue properties for the baseline compared to the repaired samples. From Table 4.4, the repaired sample at 0.1% strain ran for 10,000 cycles without failure whereas the baseline had a life of 5250 cycles. Similar trend was observed at 0.2% strain range and levels off at 0.3% strain. The repaired samples show a similar fatigue life to the baseline. The repaired sample graphs appear to show better fatigue life due to the general scatter in fatigue data.

Table 4.4. IN 738 TMF values for Baseline and GTAW samples

STA Base Line		**STA GTAW**	
Strain %	**No. of cycles**	**Strain %**	**No. of Cycles**
0.1	**5250**	**0.1**	**10000**
0.2	**1250**	**0.2**	**3000**
0.3	**500**	**0.3**	**500**
0.6	**130**	**0.35**	**750**
0.8	**50**		

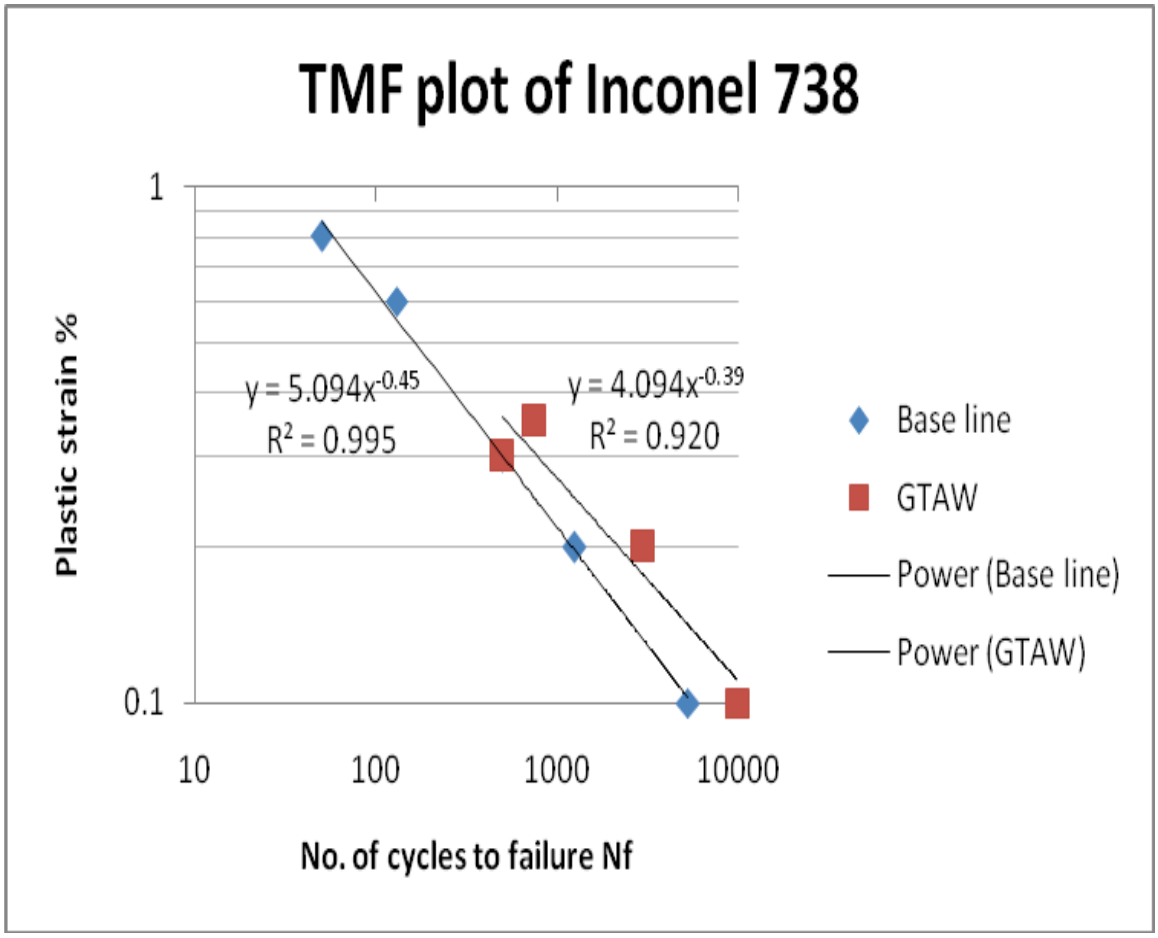

Figure 4.30, A Plot of IN 738 TMF data for both baseline and repaired samples

Figure 4.31 compares the baseline fatigue life for both alloys. Comparison of the base alloy TMF for DS R80 and IN 738 shows that, the directionally solidified alloy had better fatigue properties compared to the polycrystalline alloy at high temperatures. This is as a result of the elimination of grain boundaries perpendicular to the loading axis in the DS alloy, thereby minimizing the effect of creep-fatigue interaction during TMF. With less

grain boundary area, oxygen and other embrittling species will have limited interaction with fatigue damage leading to improved fatigue life. In addition, the smaller volume fraction of porosity in the base alloy of DS R80 compared to IN 738 affords the alloy with less site for crack initiation and hence better fatigue life. Fatigue life largely depends on solidifcation defects such as porosity. The orientation of grains in the <100> direction for DS R80 also reduces the magnitude of the state stress with subsequent improvement in mechanical properties.

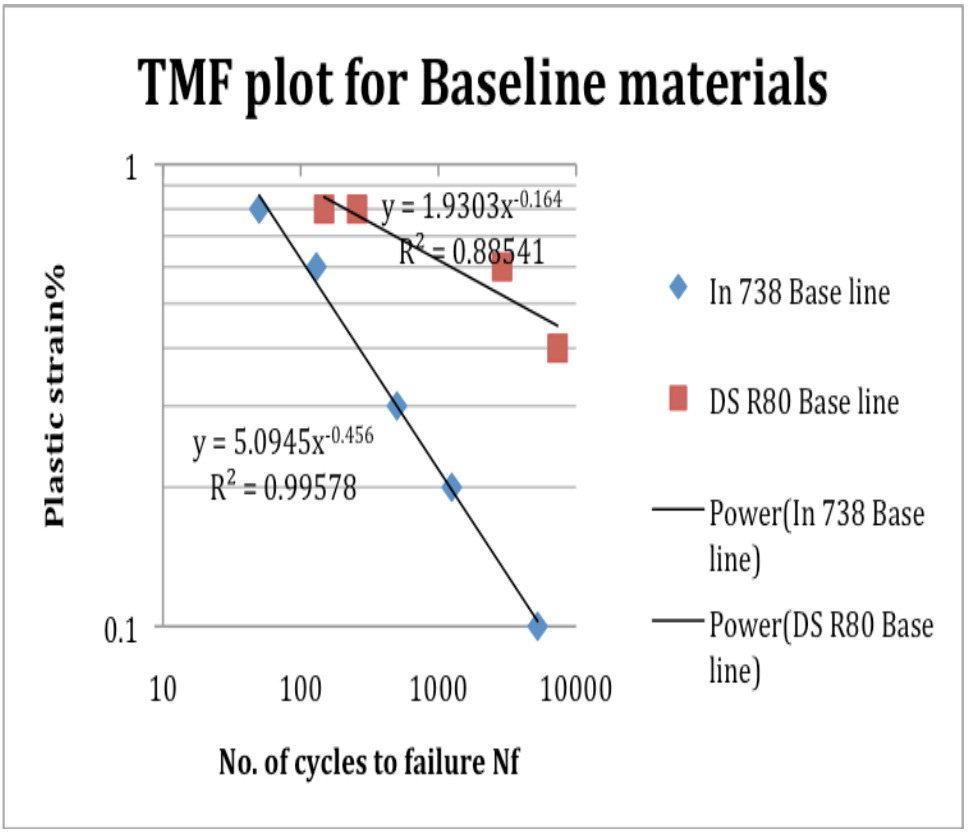

Figure 4.31 A plot of R80 and IN738 baseline

The TMF graph for the repaired (GTAW) samples shown in Figure 4.32 for both alloys shows DS R80 with superior fatigue life compared to its polycrystalline counterpart, which is consistent with the base alloy result. This implies that for both baseline and repaired samples, the DS R80 always posses superior fatigue properties compared to the IN 738 due to less grain boundary area, elimination of grain boundaries perpendicular to stress direction and less fraction of porosity in the base alloy. Less grain boundary area and porosity density for DS R80 confers better creep and fatigue properties respectively.

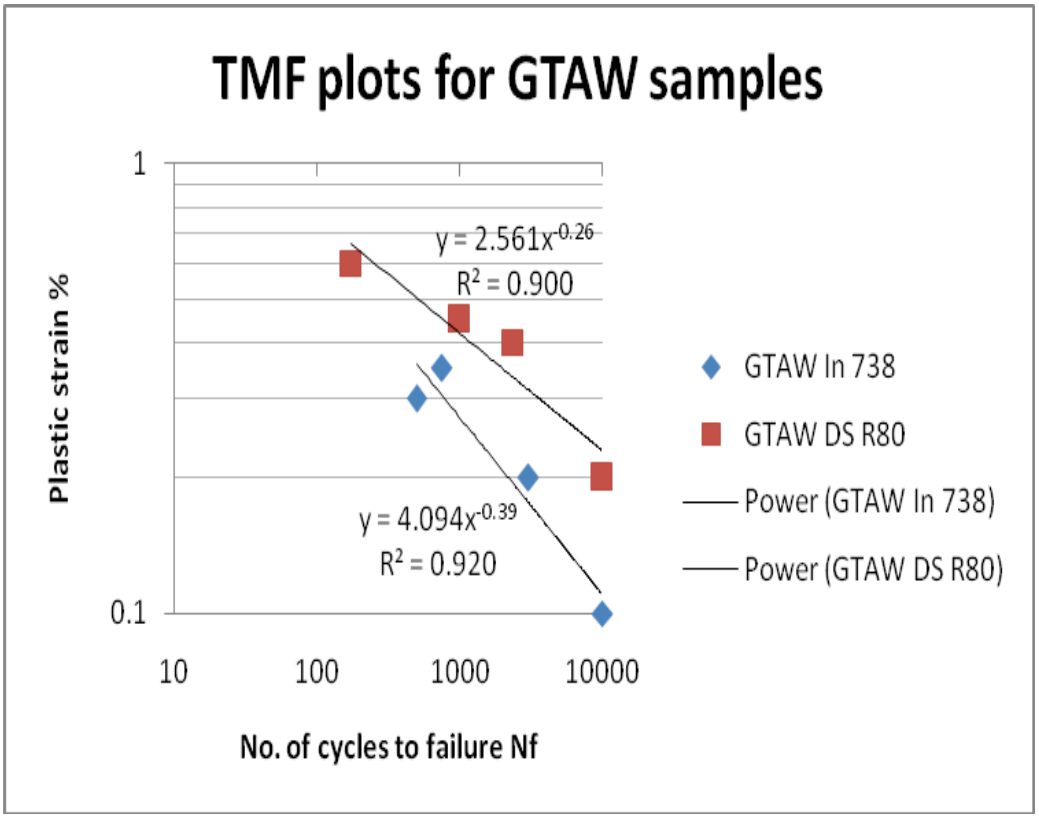

Figure 4.32 A Plot of DS R80 and IN738 repaired samples

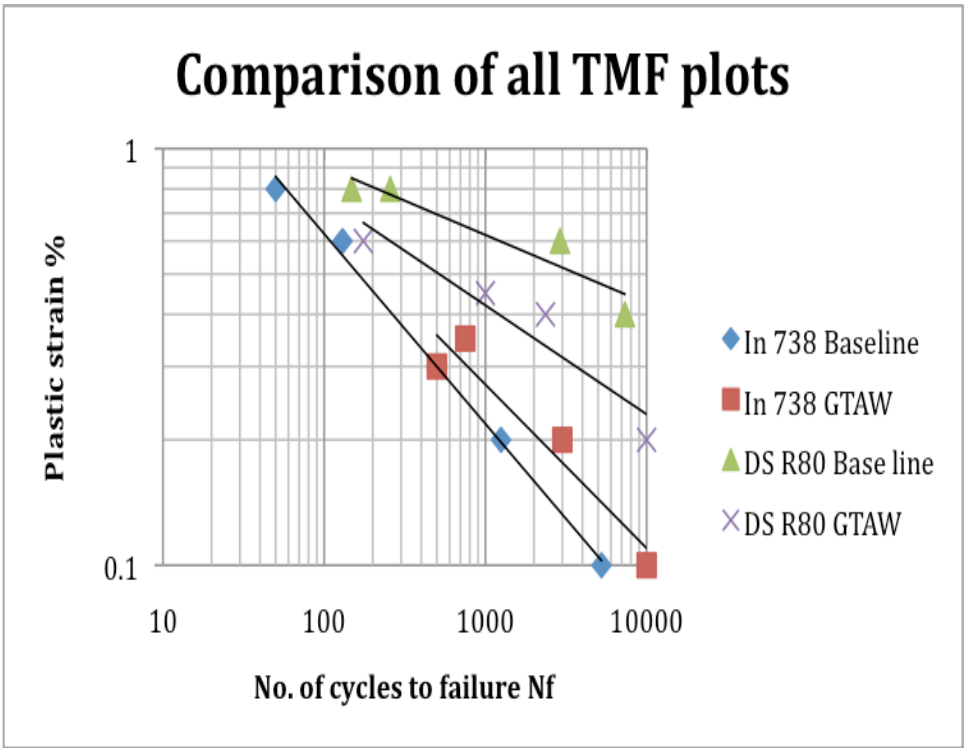

Figure 4.33 A plot of all TMF data for repaired and baseline IN738 and DS R80

The variations in the results for baseline and repaired IN 738 and the DS R80 suggest that, repaired component can be as good as the new component if the right conditions necessary for defect free welds are determined and applied throughout the repair process. The general impression derived from the superposition of all the TMF graphs underscores the importance of process optimization in the repair industry. For example, weld quality of welders reduces with time during working hours due to human fatigue. A system that replaces the welders with fresh hands in the course of the working day will help reduce variability in welding quality, producing defect free welds that are likely to have comparable fatigue properties to brand new components. A process of pre-weld heat treatments, post weld heat treatment, selection of appropriate filler metal electrode and welding parameters for each alloy must also be engineered, such that they are boxed in a "quality assurance matrix" within which acceptable weld quality that meets industrial standards and applications can be achieved with consistency.

4.4 Microstructure and fracture analysis:

Thermo-mechanical Fatigue (TMF) of base alloys IN738 and DS R80

A limitation to the understanding of high temeperature material behavoiur is the limited information on microstructural studies of the various failure mechanisms. The microstructural damage mechanisms are not well researched and understood. This section will consider some micristructural studies on crack initiation during low cycle thermo-mechanical fatigue. The damage mechanisms in the baseline will first be studied and then compared to the repaired (GTAW) samples. The microstructure comparison

between the baseline and the repaired samples will better explain the observed patterns in the TMF plots.

Fatigue crack initiation and propagation

Cracks normally initiate from weak links in a material, being defects in the solidified alloy such as porosity. In addition, grain boundaries may also serve as crystallographic defects at high temperatures in excess of the equicohessive temperature (ECT) in polycrystalline materials. Any failure mechanism will initiate from these weak sites and then propagate to final failure. Surface defects such as pores from either mechanical damage or corrosion pits can also serve as weak links for crack initiation. Cracks can also initiate at cooling holes in real turbine blade applications. Surface roughness (intrusions and extrusions) can be other sources of stress concentration and can also act as sites for crack initiation. Several of these weak sites were observed in both study of IN 738 and DS R80, which led to the failure of the specimen and are discussed below.

4.4.1. Fatigue crack initiation and propagation at porosity sites.

As was previously reported in the base metal microstructures for both alloys, there exist approximately 0.5-1% porosity density in DS R80 and IN738 alloys respectively. Crack initiation was observed in regions of porosity defects [Fig.4.34]. SEM image [Fig. 4.35] shows that the porosity sites acted as sources of crack initiation and propagation. As was previously reported in the base microstructure, the porosity density for the DS R80 and IN738 was 0.5% and 1% respectively and contributed to the numerous crack initiation observed in both alloys.

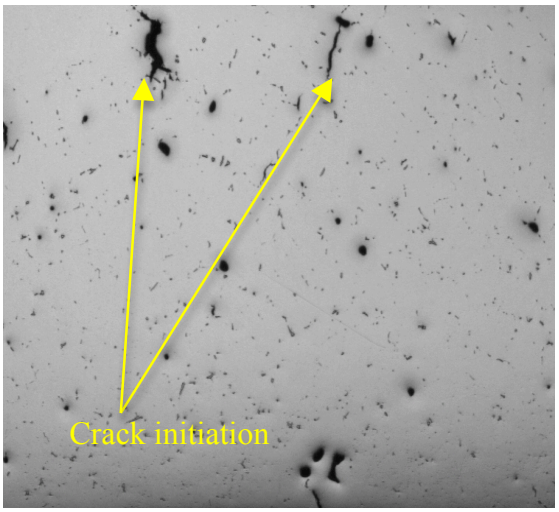

Figure 4.34 IN 738 Optical micrograph, polished sample, showing crack initiation from porosity site

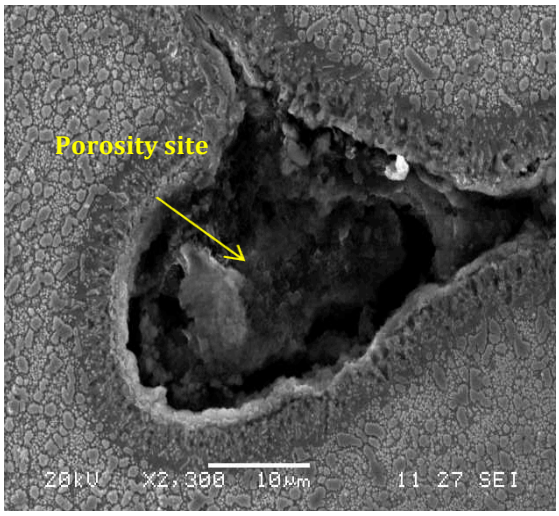

Figure 4.35 IN 738 SEM micrograph, showing porosity as source of crack initiation.

The majority of the cracks initiated from the surface of sample travelling through interconnected porosity sites [Fig. 4.36]. Similar crack initiation sites from pores have also been observed in the single crystal CMSX-4 [64]. Burke et al [65] reported an improvement in fatigue properties of HIPped In-738 due to the reduction in porosity density.

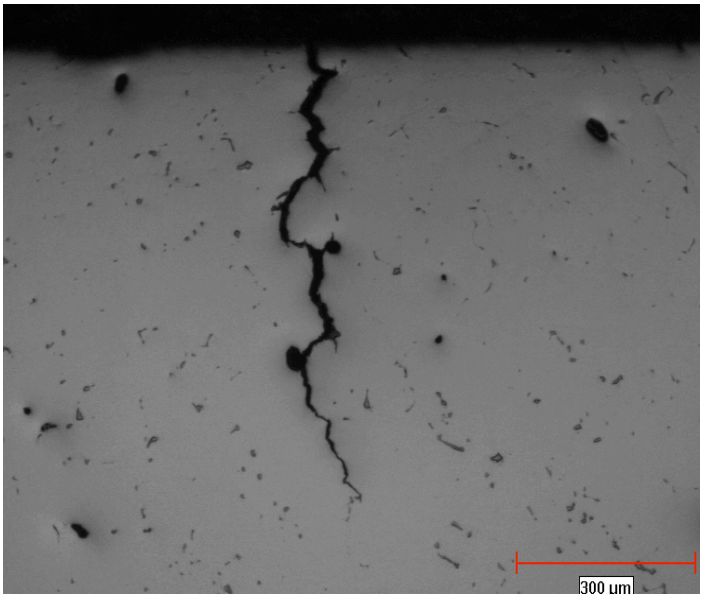

Figure 4.36 Optical micrograph, showing crack from surface and connecting porosity site

Any geometric discontinuity in a body such as porosity results in non-uniform stress distribution at the vicinity of the pore. The porosity therefore serves as a stress raiser with subsequent stress concentration at this point [66].

In the study of stage I crack initiation by M. Gell et al [67], fatigue crack initiation was noted to be as a result of porosity intersecting the surface of specimen. It is to be noted that, in aerospace gas turbine applications, not only porosity act as hole for crack initiation, but also hard object that abrades the surface of the component can cause

scratch marks or indent holes which act as stress raisers leading to crack initiation and propagation. This is normally referred to as Foreign Object Damage (FOD). In addition, cooling holes and sharp fillets or corners on turbine blades can also serve as crack initiation sites.

4.4.2. Fatigue crack initiation and propagation from precipitates.

The presence of primary MC carbides in base metal was a contributing factor to the numerous crack initiation sites observed in both IN 738 and DS R80. During loading, these refractory carbides act as obstacles to dislocation movement. When these MC carbides block slip motion, the shear stress causes dislocation pile-ups at the carbides. The brittle MC carbides are unable to accommodate the plastic strain of the matrix and consequently block the advancement of the dislocation pile up leading to in some cases a stress build up able to cut the MC carbide initiating a brittle crack. An example of a brittle fracture of an MC carbide is shown in Figure 4.37.

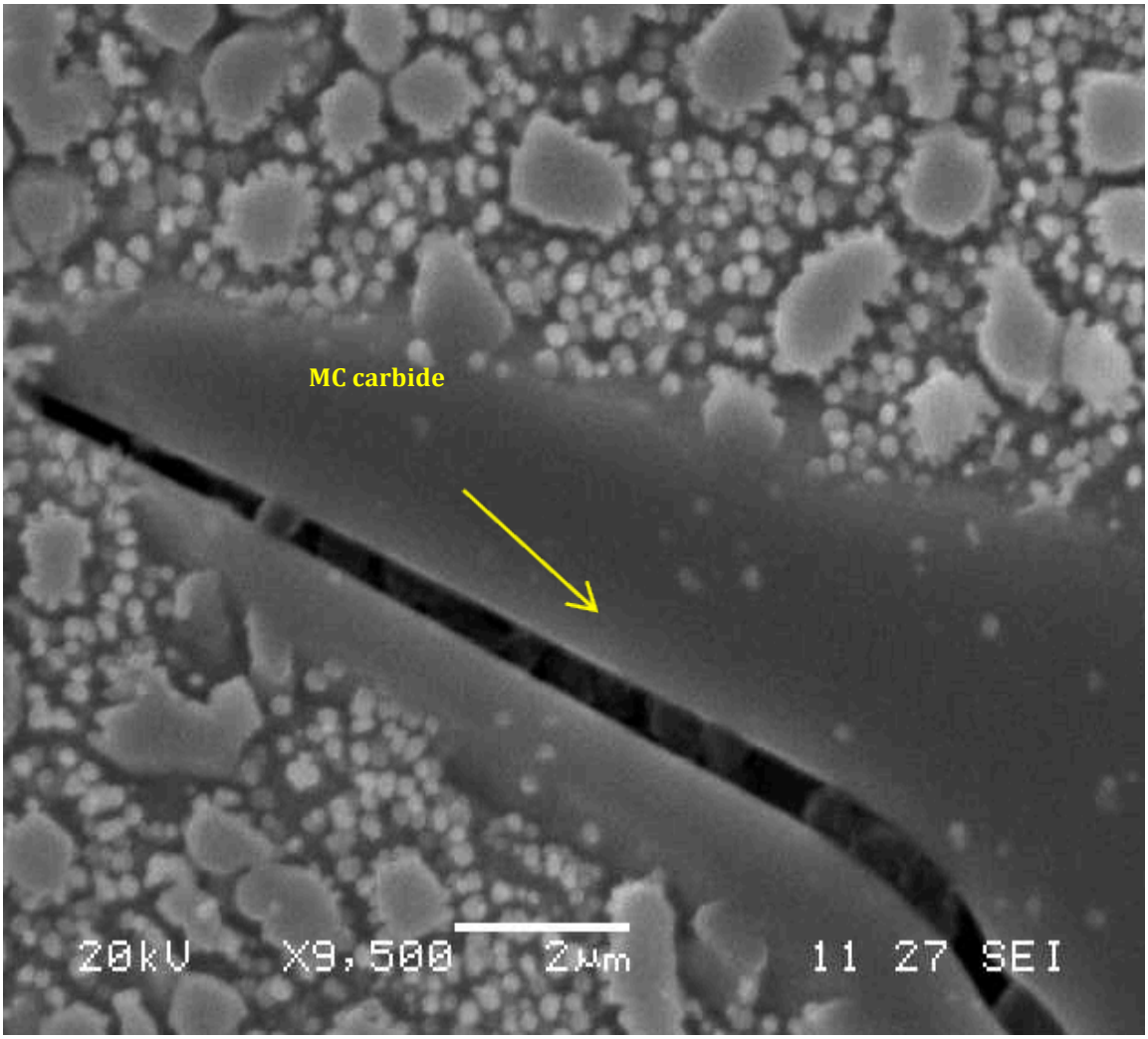

Figure 4.37 IN 738 SEM micrograph, showing MC carbide cracking

It must be noted that the MC carbides in the matrix crack but do not propagate, whereas those on the grain boundary propagates due to the grain boundaries being easy path for crack propagation above ECT. For instance, the crack initiation of carbides observed on the grain boundary, propagates beyond the boundaries of the carbide and travels on the grain boundary. However, crack initiation of the carbides situated within the grain, were unable to propagate to appreciable length that could cause failure, the cracks being arrested at the boundaries of the carbides. In the R80 micrograph [Fig. 4.38], a crack situated on the grain boundary (GB) is seen propagating on the GB but in Fig4.39, the crack direction through the MC carbide could not propagate into the material because grains, compared to boundaries are not easy path for crack propagation.

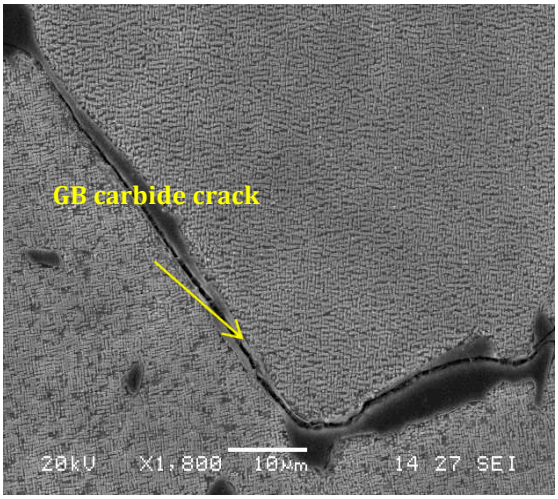

Figure 4.38 R80 SEM micrograph, etched γ' etchant, showing carbide crack on GB

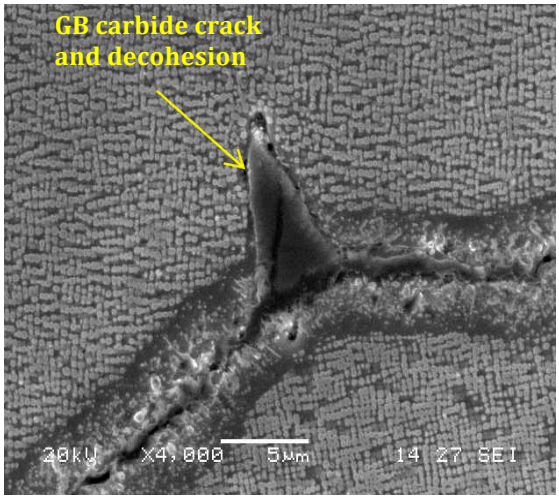

Figure 4.39 R80 SEM micrograph, etched with γ' etchant, showing crack arrest propagating into grain

The exact role of MC carbides in Superalloys applications is controversial. Some authors [3] are of the view that, they are beneficial because they stop slip and grain boundary sliding thereby preventing plastic deformation and damage. Others investigators [68] believe their presence is detrimental to the fatigue strength of the alloy since they serve as

crack initiation sites. Their formation also robs the matrix of elements that aids in the solid solution strengthening of the matrix. A compromise between its merits and its demerits can be reached by an optimized solidification process that can control the shape and size of the carbides. For instance smaller, spherical and randomly distributed carbides will effectively block slip and promote cross slip thus minimizing dislocation pile-ups that initiate wedge like cracks.

4.4.3. Fatigue crack initiation and propagation from the surface.

Most of the cracks observed initiated from the surface of the sample [Fig.4.40]. The surface cracks linked up with other cracks oriented at 45 degrees to the loading axis. Surface roughness can act as sources of crack initiation and underscores the importance of surface finish in manufacturing engineering. Initiation of cracks from the surface of specimen can also originate from slip steps at the surface of the sample during plastic deformation in a real application.

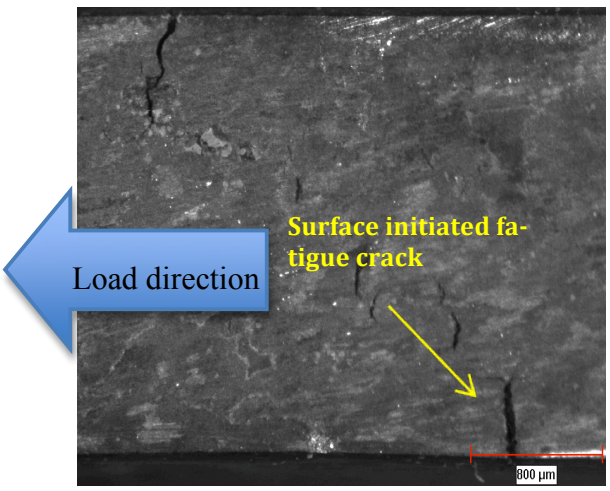

Figure 4.40 IN 738 Fatigue crack initiation and propagation from surface of specimen

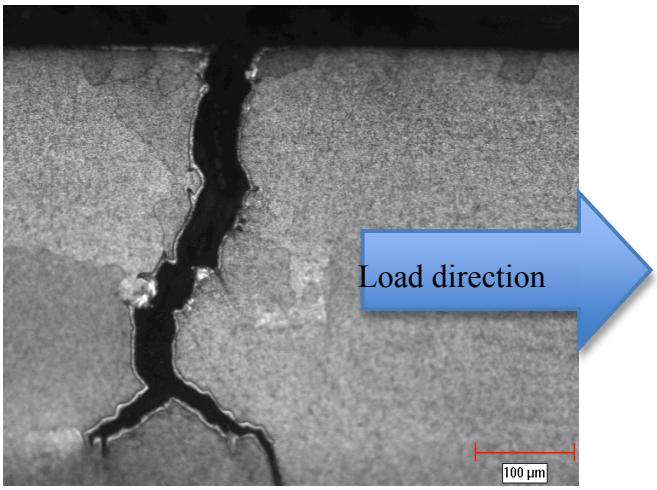

Figure 4.41 High magnification of surface crack initiation

Such steps can act solely or interact with already existing structural and geometric defect to produce cracks. The formation of the steps is due to persistent slip bands (PSB), which consist of series of "ledges" or ladders. These ladders are thought of as path of travel for dislocation movement [19]. During fatigue cycle, slip occurs in favorable planes that leads to intrusions and extrusions parallel to each other on the surface of the sample. The intrusion may grow and form a crack from continuous plastic deformation and subsequently propagates into the material to final failure. Almost all the specimen showed evidence of crack initiation from the surface of the sample in both alloys. Also, porosity and grain boundary intersecting the surface of the specimen can act as sources for surface fatigue crack initiation.

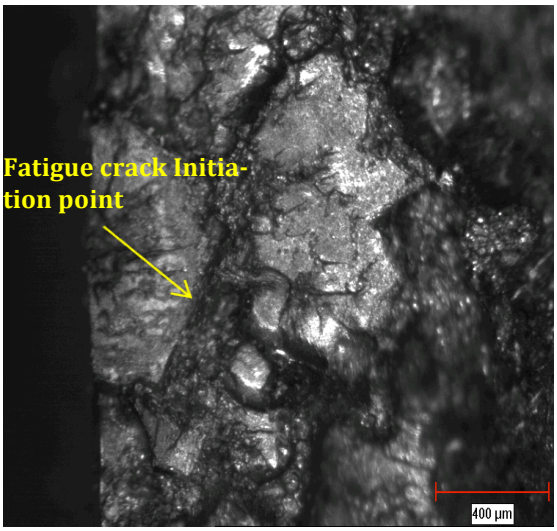

Figure 4.42 R80 Optical macrograph, showing fatigue initiation point

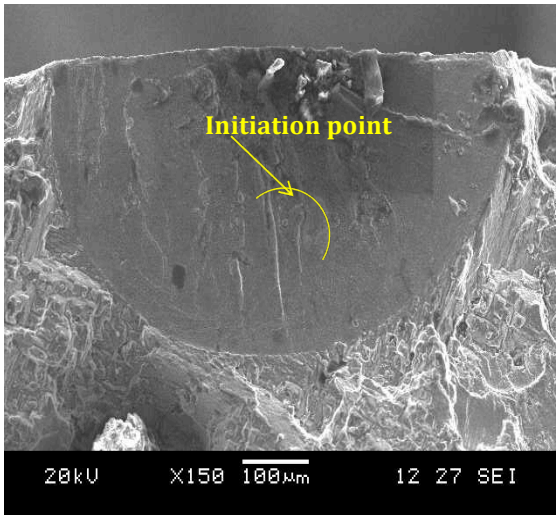

Figure 4.43, R80 SEM showing fatigue initiation point.

Figs. 4.42 & 4.43 show fatigue crack initiation at the surface shaped like a thumbnail. Most of the fatigue life of a component is spent in its crack propagation stage for low cycle fatigue. The initiation point appears relatively smooth and flat compared to the

regions of final failure. The initiation site signifies where the crack propagated slowly and the dull and fibrous texture depicts region where there was rapid failure and this kind of failure was observed in both alloys.

4.4.4 Oxidation

One of the advantages of using Superalloys in high temperature applications is their ability to resist oxidation at elevated temperatures. This property is achieved through alloying with Cr and Al. During the service life of the component, the interaction between the uncoated metal surface and its environment leads to oxidation. The inherent oxidation resistant of the alloy affords it the property to form thin protective oxide films of Al and Cr on the surface of the metal to prevent further oxidation. The effectiveness of the oxide films will depend on the arrangement of ions in the oxide, defects present in the oxide film and the mechanical properties of the oxide.

When oxide scales are formed, they contain some defects in their structure. These defects can either be missing atoms in their regular perfect crystal structure arrangement or displaced from their regular positions in the crystal lattice. Such defects are called point defects and may be grouped under vacancies, interstitials, or impurities. Vacancies form as a result missing metal cation or oxygen anion in the crystal lattice of the oxide. Interstitials are formed when a metal cation or an oxygen anion is displaced from their normal lattice positions. Impurity defects occurs when a cation is substituted by a foreign cation [69]

The arrangement of these crystal defects affects the transport of ions and electrons during oxidation. This factor and the intrinsic electronic nature of the cation dictates whether the

oxide formed will allow oxygen to diffuse into the alloy through the oxide scale or metal cation of Al and Cr will diffuse out of the alloy through the oxide scale [70]. It is therefore possible, for internal oxidation to occur even if surface oxides are undamaged and still coherent with the base metal since both Oxygen and metal ion diffusion over oxide barrier is possible. In addition, the mechanical properties of the oxide films would also dictate the effectiveness of the surface films to prevent oxidation. The cohesive strength of the oxide to the base metal will prevent spalling and the toughness of the oxide will accommodate stresses without cracking. However, there is a limit to which surface oxides can protect the alloy. In service, they lose their cohesive strength with the base metal and spall off. This has been attributed by some authors [71,72,73] to segregation of sulphur at the oxide-metal interface, which causes the de-bonding of the protective oxide film. In other instances, they crack due to stress build up in the scale and expose the metal to environmental damage. The principal source of stresses in the oxide is thermal stresses due to the difference in thermal expansion co-efficient of the oxide and the matrix. Once the mechanical integrity of the oxide is compromised, oxygen diffuses inwards and further oxidation leads to decrease in fatigue and creep life of the component [74]. Several mechanisms have been proposed to explain the effect of oxidation on the mechanical properties of Superalloys. Some of these were observed in this research and they will be discussed as follows.

4.4.41. Oxygen penetrating surface crack to cause internal oxidation.

Cracks initiated on the surface of the samples served as easy path for oxygen diffusion into the material. Figs 4.44& 4.45 show internal oxidation with alloy depletion of Cr associated with oxide formation, and oxide intrusions penetrating the crack from the specimen surface into the material.

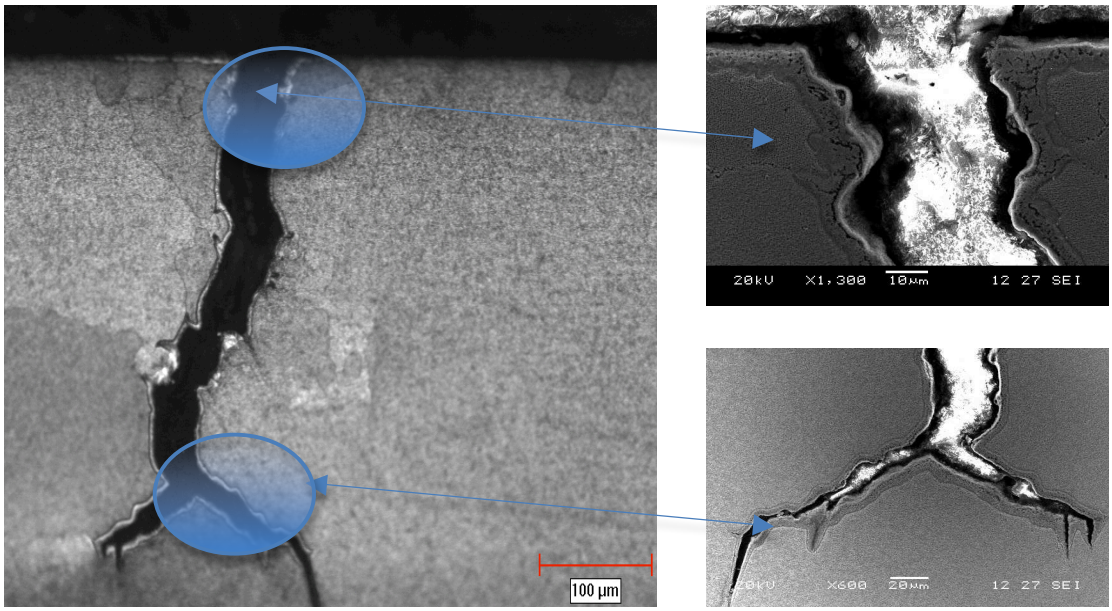

Figure 4.44 Optical & SEM micrograph showing surface crack and oxide spikes

Any crack opening on the surface of the metal will lead to internal diffusion of oxygen. Oxidation interacts with creep and fatigue to reduce the mechanical life span of the component. Either, oxidation will embrittle the grain boundary, or will cause formation of brittle oxide crack ahead of the crack. Oxidation can also lead to decohession of carbides, which leads to crack initiation.

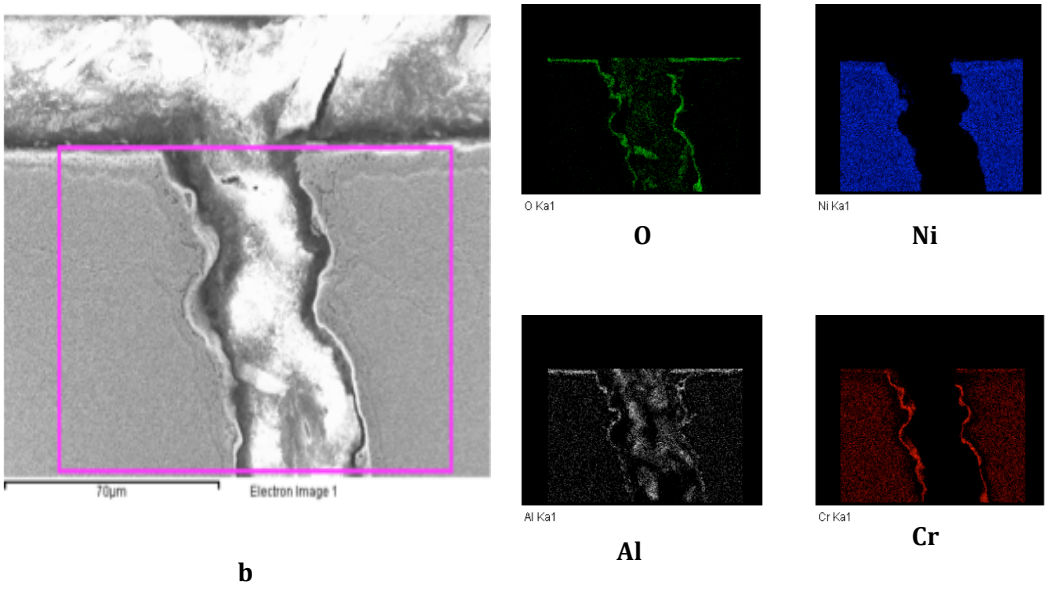

Figure 4.45, R80 SEM-EDS analysis, showing oxidation along crack from surface of sample.

4.4.42. Gamma prime depletion associated with oxidation at areas beneath sample surface and close to a crack.

One of the main strengthening mechanisms in Ni base Superalloys is precipitation hardening. Oxidation leads to the depletion of elements such as Al, Cr, Ni and Ti. The oxidation reaction forms oxides at the surface of the sample and at regions close to cracks. These oxides can be NiO, TiO_2, Cr_2O_3, or Al_2O_3. In practice, the normally observed oxides are a combination of these elements normally referred to as "spinel" $[Ni(Cr,Al)_2O_4]$. Coincidentally, two of these oxides (Al_2O_3 and TiO_2) have constituents of γ' ($Ni_3[Al,Ti]$) forming elements. This subsequently leads to the depletion of gamma prime phase at the surface of specimen and in regions of crack initiation as shown in Fig. 4.46. Such a depleted region will experience different fatigue yielding from the bulk, with

possible deformation bands developing in the precipitate free areas initiating microcracks. Any form of dislocation movement or crack initiation that originates from the gamma prime depleted region will meet relatively less resistance. As the crack propagates to the depth of depletion, and increases in length, more oxygen penetrates the cracks leading to more oxidation with subsequent reduction in strength. Plastic flow damage therefore increases and the observed depletion of γ' from oxidized crack boundaries leads to an increase in plastic flow and can lead to crack growth as was also reported by Rahmani et al [75]

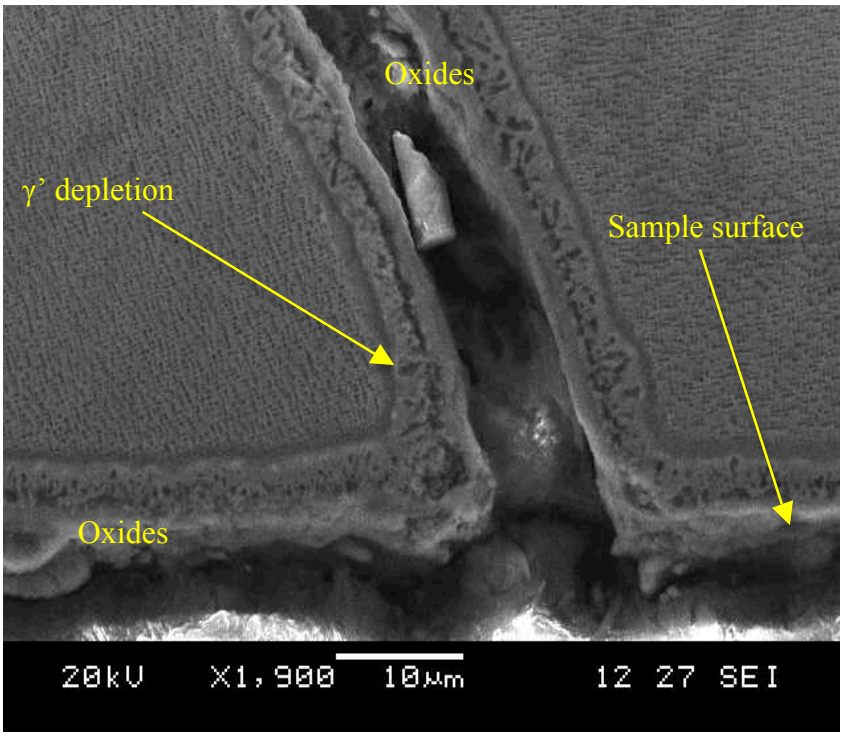

Figure 4.46 SEM showing γ' depletion at near surface region and in crack initiation region

4.4.43. Preferential oxidation of MC carbides intersecting a grain boundary

During thermo-mechanical fatigue, grain boundaries serve as easy path for atmospheric oxygen diffusion into the metal. As mentioned earlier the inward diffusion of oxygen ions leads to a chemical reaction with metal cations to form oxides. The chemical reactivity at the interface of carbide and matrix is different from the bulk matrix such that MC carbides intersecting a grain boundary get oxidized at its interface with the matrix leading to weak bonding. For example, in the micrograph 4.47 of IN 738, oxidation occurred at the carbide-matrix interface. This is evident because of the γ' depletion in the vicinity of the carbide along the crack length. With continuous application of load, a stress level far below what will normally cause decohesion of the carbides will overcome the little binding force remaining between the carbide and the matrix and dislodge the MC carbide from the matrix creating a void [55,56]. Stress will subsequently be amplified in this region, and a localized stress level exceeding the bulk stress will initiate a crack if not relaxed by plastic deformation. This form of oxidation-assisted carbide decohesion was observed in both alloys and contributed to the intergranular cracks observed in the samples.

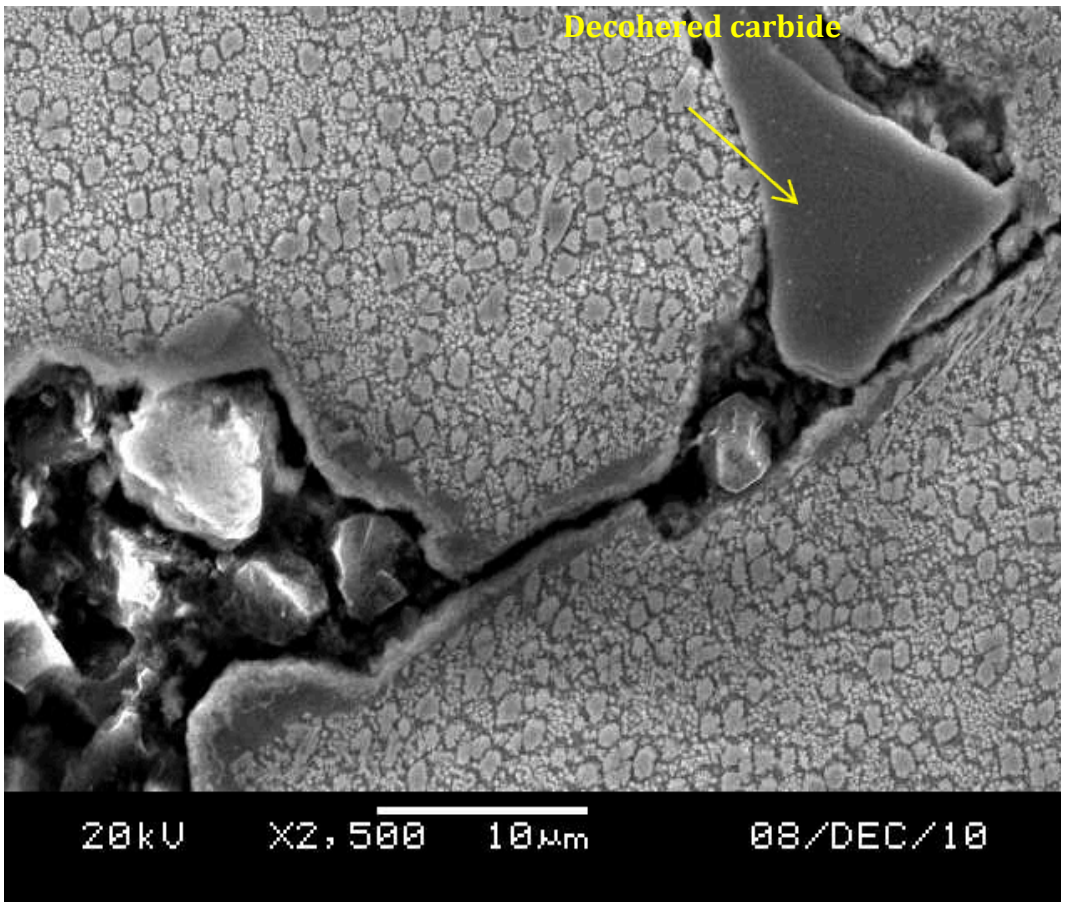

Figure 4.47 IN 738 SEM micrograph, showing preferential oxidation and decohession of MC carbides

4.4.44. Embrittlement involving atomic oxygen diffusion on grain boundaries

Starink et al [55] and other researchers [56] have also reported that embrittlement due to atomic oxygen penetrating grain boundaries and diffusing to crack tip influences the fatigue crack propagation. This effect was attributed to the diffusion of oxygen into the highly stressed alloy grain boundaries ahead of the crack tip resulting in interface decohesion and brittle intergranular crack propagation. Tensile stress forces the grain

boundary open making crack propagation very rapid under very low stress levels far below the yield stress during low cycle TMF.

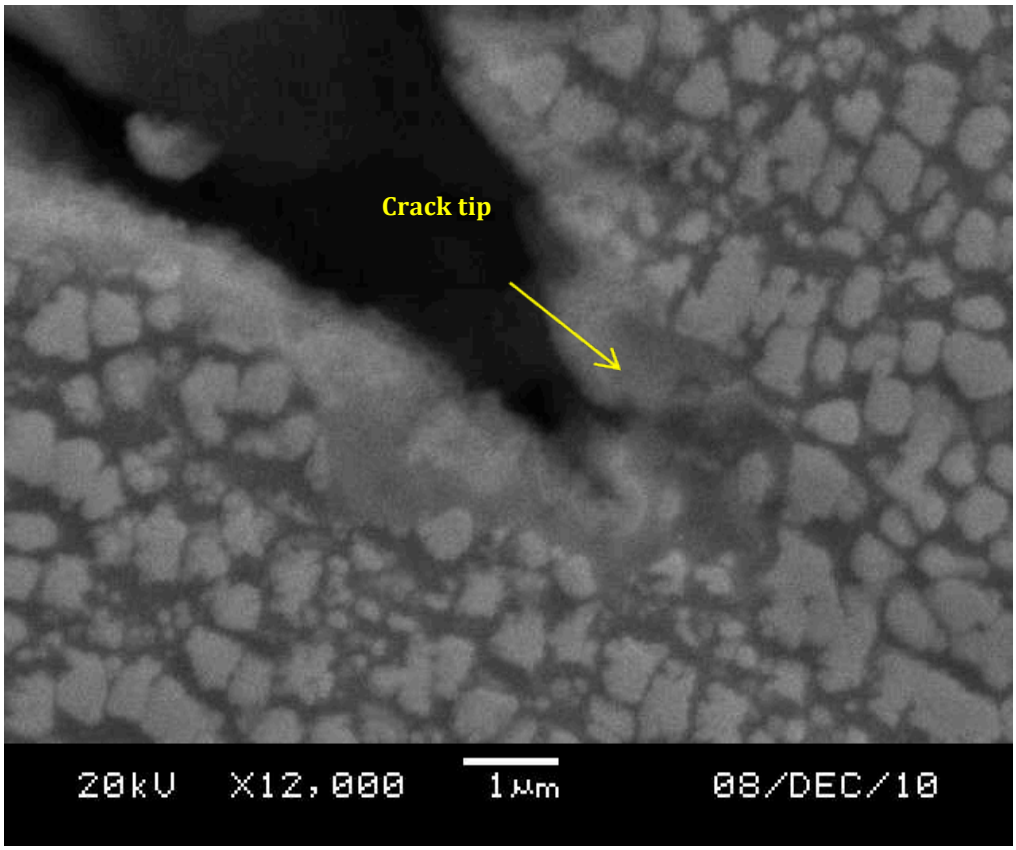

Figure 4.48 SEM micrograph, etched with γ' etchant, showing crack tip with branching at some angle to the crack tip

Such cracks normally do not have oxidation products ahead of crack tip and normally plays a role in the damaging mechanisms when the strain rate is very low. At high strain rates however, fatigue crack propagation is so rapid that, oxygen anions does not get the chance to penetrate the crack tip to cause embrittlement and the crack propagation will be purely due to fatigue. This kind of fatigue crack tip lacking any oxidation product were observed [Fig. 4.48] in the two alloys under study and was an indication that embrittlement might have played a damaging role in the two alloys.

4.4.45. Brittle Oxide cracking ahead of crack tip

In low cycle thermo-mechanical fatigue, plastic strain at the tip of an intergranular crack will be higher than strain imposed on the bulk material. This plastic strain is relaxed by plastic deformation with little increase in stress and the stress distribution becomes essentially uniform [20]. The plastically deformed region ahead of the crack tip will have a different chemistry of reactivity compared to other parts of the bulk material and becomes more susceptible to oxidation than other parts of the crack. Inward diffusing oxygen anion would diffuse towards the crack tip and would react with counter diffusing metal cation forming hard and brittle oxides ahead of the crack tip [Fig. 4.49,4.50] Figure 4.49 shows brittle oxide ahead of the crack in DS R80 alloy. Similar oxides forming ahead of crack tips were also observed in the polycrystalline IN 738 alloy. The brittle oxides however do not undergo plastic deformation and stress concentration on the grain boundary will build up in the oxide. The brittle oxide, with little fracture toughness, initiates cracks to relax the stresses after which there is more plastic deformation at crack tip followed by oxidation and oxide cracking, thus the cycle continues and the crack advances[51,52]. This kind of failure normally happens on grain boundaries because they serve as easy conduit for oxygen anion diffusion and formation of oxides. Oxide formation ahead of crack tip on the grain boundary was quite extensive in both alloys and might have contributed to the intergranular cracks observed. Evidence of micrographs, which appears to be crack healing was also observed [Fig. 4.50]. Sullivan and Donachie [10] observed in their work that, oxide formation that tends to partially heal cracks can cause strengthening as the oxide takes up some of the load offsetting the accelerated development of the crack [10]. Similar results were also reported by Duquette and Gell

[76], in single crystal Superalloy showing better fatigue properties in air at 927 ^{o}C compared to vacuum due to crack healing by the formation of oxides. It is therefore not clear the precise contribution of oxide spikes to the total failure of the component as opinion seems to be divided in the works cited above.

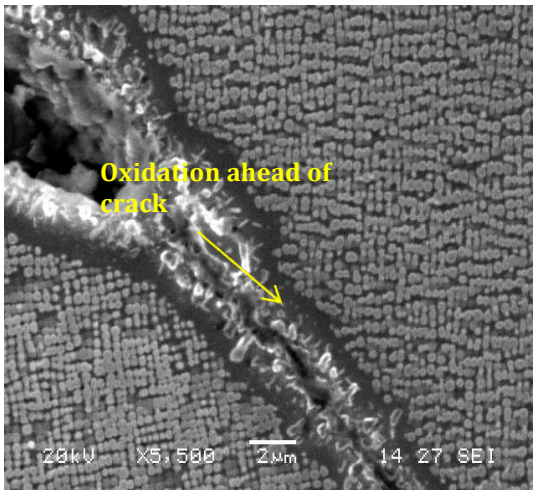

Figure 4.49 R80 SEM micrograph, etched with γ' etchant, showing γ' depletion on GB

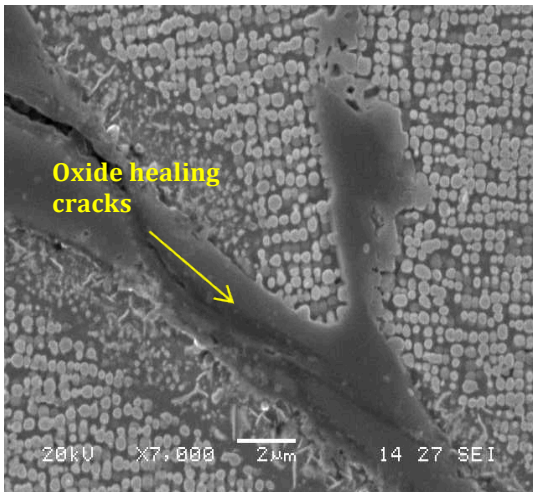

Figure 4.50 R80 SEM micrograph, etched with γ' etchant, showing evidence of cracking healing

4.4.5 Creep deformation and fatigue interaction.

Creep normally occurs in Ni base Superalloys at Homologous temperatures of 0.45-0.6. This temperature is estimated to be between 775K-925K in Ni base Superalloys [77]. Within this temperature range and above, diffusion becomes a significant factor. Diffusion being a thermally activated process shows an exponential dependence on temperature. Below 0.46Tm, the diffusion coefficient is low such that any deformation mode that is exclusively dependent on a diffusion process can be safely ignored. During the TMF test, the samples were cycled between the temperatures of 500^{o}C-900^{o}C for both

alloys, a temperature range well in the domain for diffusion aided deformation mechanism. In practical situations, a number of mechanisms may be responsible for creep deformation, notably diffusion creep, dislocation creep, dislocation glide and grain boundary sliding. These mechanisms occur at different combinations of stress levels and homologous temperatures. For thermo-mechanical fatigue tests conducted under varying strain, the stress and the temperature varied and a number of these mechanisms may be acting during the diffusion aided deformation process. Amongst the aforementioned mechanism, the one responsible for intergranular crack initiation and propagation through void formation on the grain boundary is grain boundary sliding. Creep voids were observed in only the base material for IN 738, no evidence of creep damage was observed in the DS R80 base material. This was probably due to the elimination of the grain boundaries perpendicular to the stress axis in the DS alloy. At the equicohessive temperature (ECT), the grain strength is the same as the grain boundary. The microstructure of IN 738 and R80 is tailored to precipitate small $M_{23}C_6$ and M_6C on the grain boundary to prevent grain boundary sliding. At temperatures above the ECT, under the influence of shear stress concentration and minor changes in shape of the grain due to diffusion process, the grain boundary become weaker than grains and the barriers are overcome leading to sliding of the grain boundaries. In the samples analyzed, wedge like voids were formed due to the difference in relative shear sliding action of the different grains in IN738. The sliding is possible because of high stresses normal to the grain boundary, which is capable of nucleating the wedge-like voids. These large stresses are likely to be produced in the vicinity $M_{23}C_6$ and M_6C particles, intersection of slip bands & grain boundary and more importantly at triple points on a sliding grain boundary. Both

optical and SEM magnification images [Fig.4.51 & 4.52] show the creep voids on grain boundaries and at triple point in IN 738 base alloy.

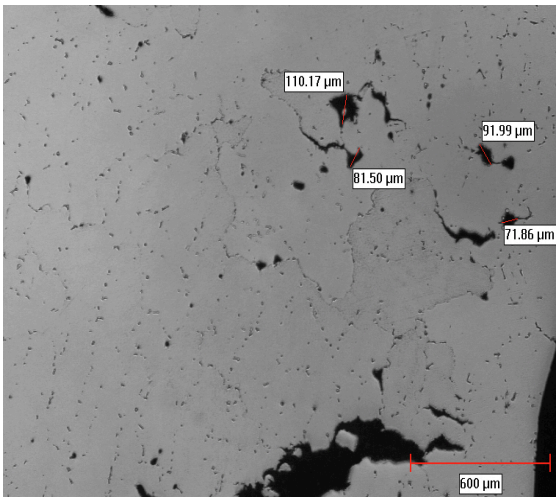

Figure 4.51 IN 738 Optical micrograph, polished, showing r-type void formation in base alloy

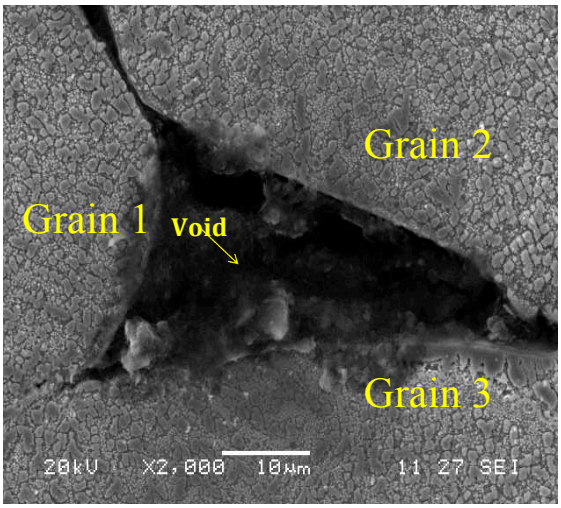

Figure 4.52 w-type void nucleation at triple point

However, w-type voids are less likely to occur in DS R80 base material since it is directionally solidified, having all grains oriented in one direction, preferably parallel to the stress axis and devoid of triple points which initiates these voids. The fracture surface of the failed specimen showed dimples with precipitates, which might have initiated the voids. The dimples are the half of the voids that came apart after final fracture failure.

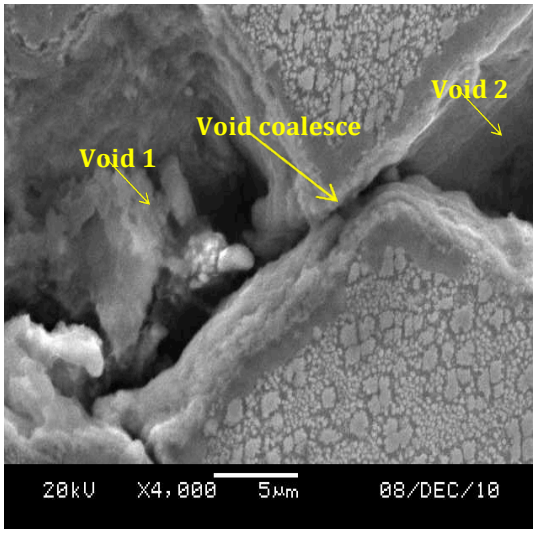

Figure 4.53 IN 738 Coalesce of voids by fatigue crack

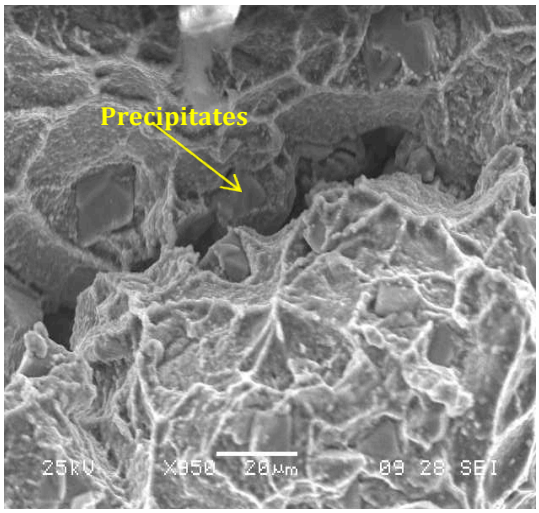

Figure 4.54, SEM fracture surface, showing dimple from fracture voids and particles that might have initiated the voids.

When the voids are nucleated on the grain boundary, they play similar role as porosity to initiate crack and coalesce by intergranular fatigue crack propagation. Interactions of creep and fatigue form of deformation at high temperatures leads to material instability and necks down to a point with the voids aligned perpendicular to the plane of stress application. Evidence of necking at the failed parts further confirmed creep voids playing a role in the ultimate failure for the base material of the polycrstalline alloys [Fig. 4.55]. The cumulative effect of the tensile component brief hold time of 1.5 sec. hundreds to thousands of cycles is translated to hours of total hold time, which is significant to cause creep.

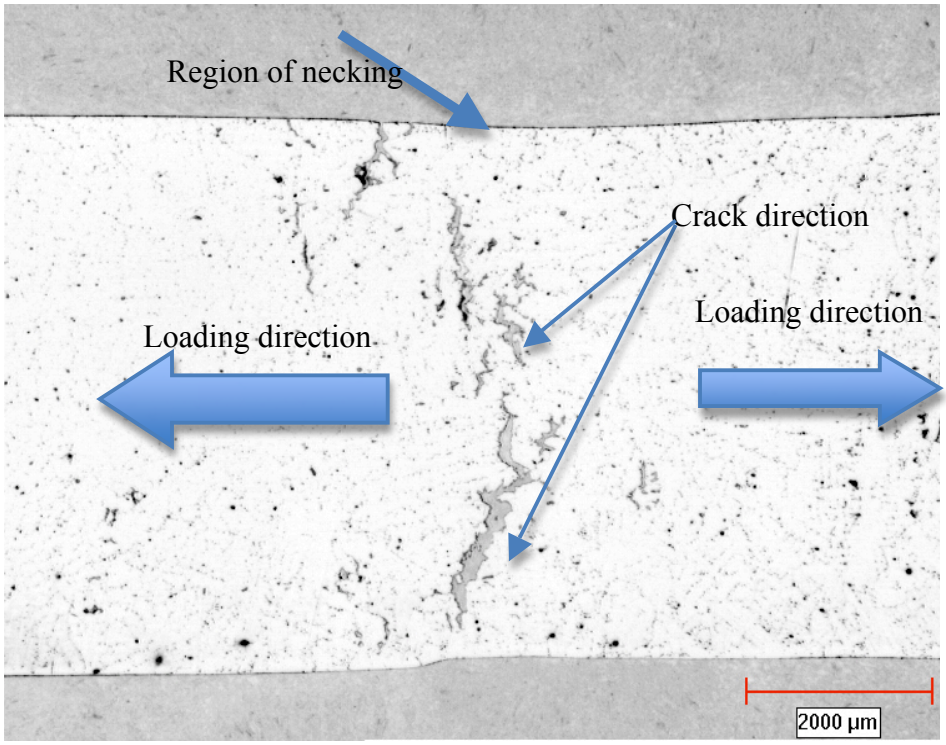

Figure 4.55 Optical micrograph, showing necking at failure section in IN 738 base alloy

4.4.6 Phase coarsening and incipient melting of low melting point γ-γ' phases in IN738.

Gamma-gamma prime eutectics coarsened in some regions of the base alloy IN 738 notably at triple points [Fig.4.56]. Precipitates of smaller gamma prime were observed in the coarsened gamma prime. Some regions of the coarsened eutectics were observed to undergo incipient melting [Fig. 4.57]. The incipient melting introduced more defects that can initiate cracks and degrade the mechanical property of the alloy during low cycle thermo-mechanical fatigue.

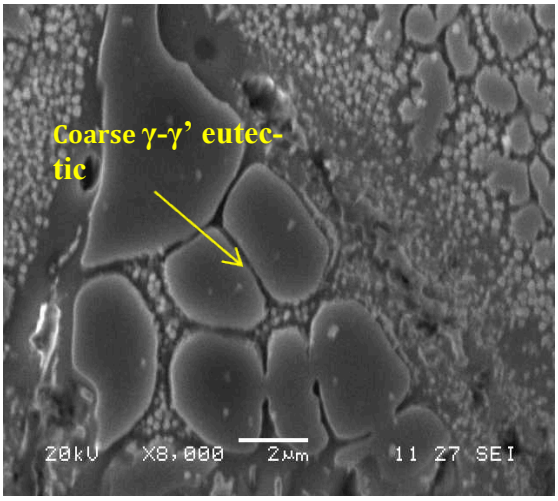

Figure 4.56 IN738 SEM micrograph, etched with γ' etchant, showing coarsening of γ'

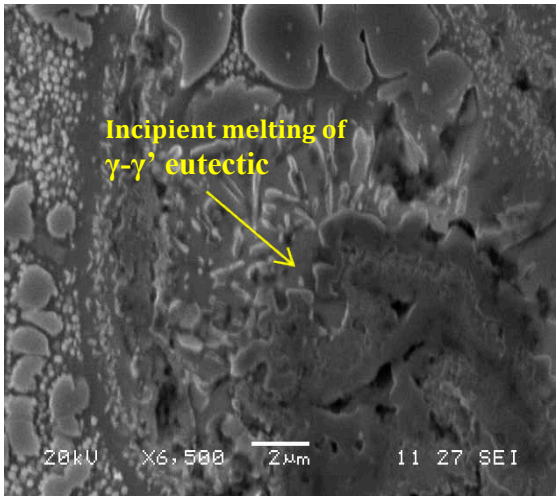

Figure 4.57 IN738 SEM micrograph, etched with γ' etchant, showing incipient melting of γ-γ' regions.

Regions of gamma prime depletion close to the coarsened eutectics suggest that there was considerable oxidation in this vicinity. The depletion of the gamma prime phase would rob the alloy of its main strengthening phase. This low melting point eutectic is formed from the last liquid to solidify due to dendritic microsegregation during solidification. Interdendritic liquid supersaturated with γ' forming elements caused by continuous enrichment of solute atoms at temperatures close to the equilibrium solidus culminates into the formation of the γ-γ' in the interdendritic regions of the alloy. The temperature for the formation of γ-γ' have been determined to be around 1230^{o}C and 1198^{o}C but could also be as low as 1180^{o}C [58]. The formation of the γ-γ' phase in the alloy is undesirable since it can melt at lower temperatures below the solidus of the bulk alloy and also rob the alloy of solid solution elements that could have strengthened the alloy.

However, it is not clear whether the incipient melting occurred during the STA prior to testing or during the TMF test.

In addition, grain boundary sliding in the regions of incipient melting of γ-γ' located at triple point served as sources for w-type void formation [Fig. 4.58] which will eventually initiate intergranular cracking. This form of damage was only observed in the IN 738 but absent in the DS R80 since there were no eutectics in the base DS R80 alloy. This can be one of the several reasons why IN 738 alloy showed a relatively poor fatigue life compared to the DS R80 for both baseline and repaired.

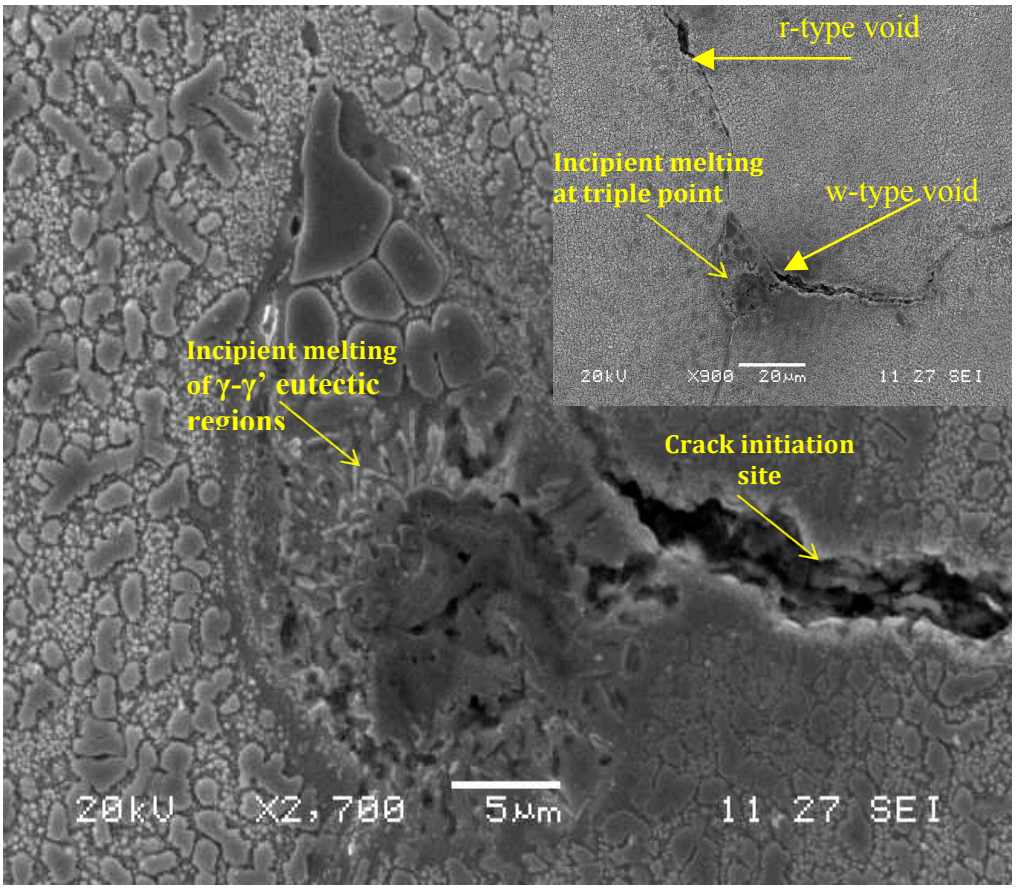

Figure 4.58 incipient melting of γ-γ' at triple point.

Elongated gamma prime, a phenomenon normally referred to as rafting was also observed in this work [Fig. 4.59]. Rafting normal to the direction of the load axis confers strength to the alloy by optimizing the lattice misfit towards a negative value thereby preventing dislocation climb [5]. A negative misfit does encourage the formation of raft γ‘ phase which is essentially layers of the phase in a direction normal to the applied stress. This rafting can help reduce creep rate if the main mechanism involves the climb of dislocations across the precipitate raft [11].

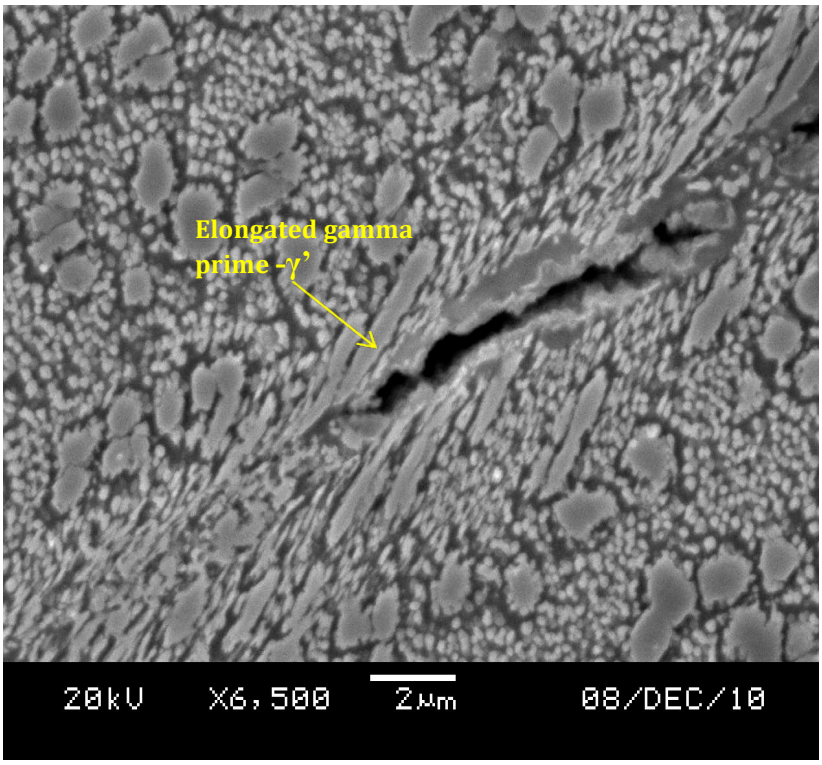

Figure 4.59 SEM micrograph, showing rafting

4.5 Failure mechanisms in the repaired samples.

The repaired samples had similar failure mechanisms as the base material except for extra failure initiation sites not present in the baseline. Typical failure mechanisms in baseline include creep, fatigue failure from porosity sites & surface of specimen and oxidation related failure mechanisms. They will not be discussed further. However, the extra failure initiation sites in the repaired samples are worth mentioning and will be discussed. These extra failure initiation sites not present in the base line were responsible for the occasional inferior fatigue properties of the repaired components compared to the base line. They include weld defects such as fusion zone cracking and heat affected zone cracking, insufficient fusion between weld joint and base material and other metallurgically related discontinuities such as recrystallization. These factors may act solely or sometimes simultaneously to degrade the mechanical property of the repaired sample. The difficulty and challenge is in controlling the defects and the discontinuities during the welding process. In the analysis of the repaired samples, it was evident that majority of the final crack that led to the final failure were in the vicinity of the welded joint and the joint itself. Some observed crack initiation sites that might have contributed to the inferior fatigue property of the repaired sample will be discussed.

4.5.1. Micro cracks in fusion zone and heat affected zone

All the cracks that led to failure were observed in the HAZ and the fusion zone. One possible explanation to this observation is the presence of weld defects in the fusion zone and the heat affected zone in the welded samples prior to the TMF test which was discussed earlier in the weld microstructure. In addition, the smaller grain sizes in the fusion zone prior to the TMF will encourage more void formation due to creep and subsequent fatigue intergranular cracks at high plastic strains and temperatures.

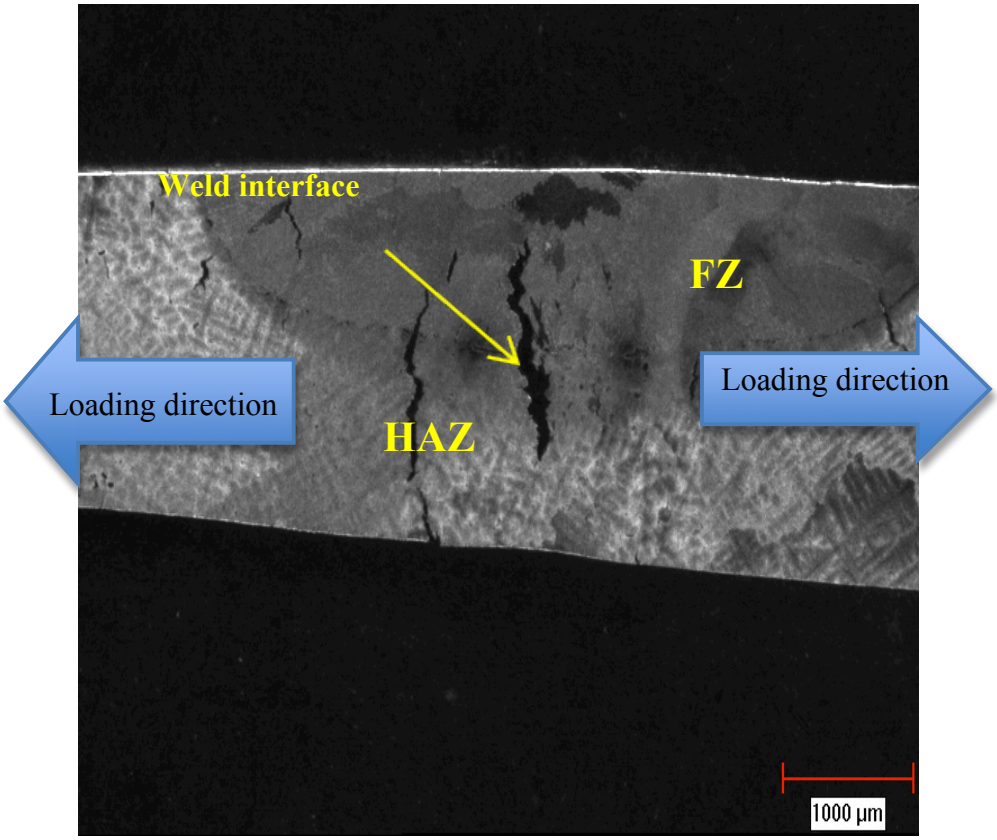

Figure 4.60 Optical micrograph, etched with Marbles reagent, showing direction of crack propagation.

Optical macroscopic examination revealed cracks oriented at some right angles to the direction of the loading axis [Fig. 4.60]. The general crack path was zigzag and intergranular with rare intragranular crack initiation in IN738. The zigzag nature suggest the contribution of creep to the fatigue damage, as the cracks follow the intergranular nature of creep deformation. Figure 4.61 shows crack initiation in FZ and surfaces beneath the weld.

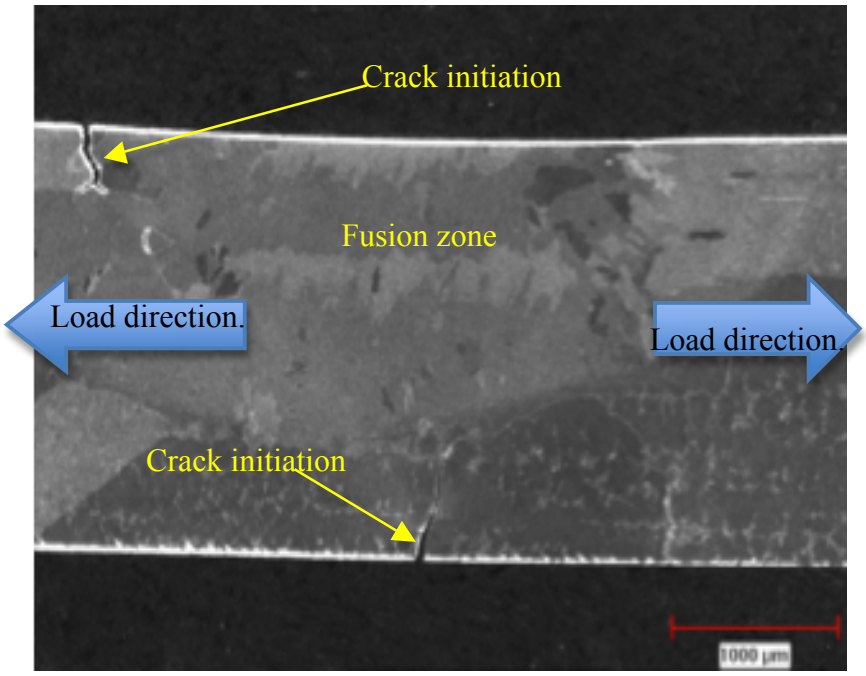

Figure 4.61 R80 Optical micrograph, etched with Marbles, showing crack originating from surface of sample.

For the DS R80, the crack propagation was intragranular in the base and the HAZ and changes to intergranular in the fusion zone. It is reported in the literature [78,79] that secondary solidification products such as MC carbides, borides, sulphocarbides , γ-

γ'eutectic and low melting point elements such as B, C, S and P can cause incipient melting [80] which leads to micro cracks in the HAZ during welding. Recent research [81,82], also discovered that gamma prime γ' can also liquate on grain boundaries in the HAZ. The melting phenomenon produces liquid films on the grain boundary during the welding process. These liquid films wet the grain boundary weakening the intercrystalline bonds. During weld pool solidification, the wetted grain boundaries easily come apart as result of tensile stresses imposed by the contraction of the cooling weld joint on the HAZ causing cracks in the HAZ. The cracks can act as sources of stress raisers for damage initiation. Cracking can also occur during post-weld heat treatment, a phenomenon known as strain age cracking. During aging, stresses are built up on embrittled boundaries due to precipitate growth with subsequent crack development as a mechanism to relax stresses. Although stress raisers are not usually thought to be dangerous in ductile materials subjected at constant loading, appreciable stress concentration effect will occur in ductile materials under fatigue conditions [20]. At high temperatures of >0.5Tm, the material can be treated as a ductile material and under fatigue loading, stress raisers at this microfissure site will increase stress concentration and may initiate cracks which propagates to final failure during high cycle fatigue. The microfissures that develop in the HAZ will therefore greatly influence the mechanical properties of the repaired component when placed in service.

4.5.2. Incomplete fusion on the weld-metal interface.

Good fusion between the weld metal and the base metal is critical if full strength of a joint is to be achieved. Incomplete fusion means that at some point in a weld, the base metal and weld metal have not been joined properly. Possible causes for incomplete fusion may include [26]:

1. Failure to raise the temperature of the weld area to the correct level
2. Failure to remove large amounts of mill scale, oxides, or any other foreign materials present on the base metal. These materials could hinder the fusing of the weld metal to the base metal.
3. Improper joint design basically refers to the size of the groove angle and root openings on a butt joint. Should these angles or openings be too small for proper electrode extension and gas shielding, incomplete fusion and possible other defects can occur.

Incomplete fusion was observed in some of the repaired samples. Fig. 4.62 shows cracks due to fatigue and creep running perpendicular to the direction of loading axis, however, on careful observation, a crack situated on the weld-base metal interface is seen running parallel to the direction of the loading direction. The direction of the crack and the exact positioning suggest it was incomplete fusion between the weld metal and the base metal and this can lead to a reduction in the mechanical properties of the welded samples.

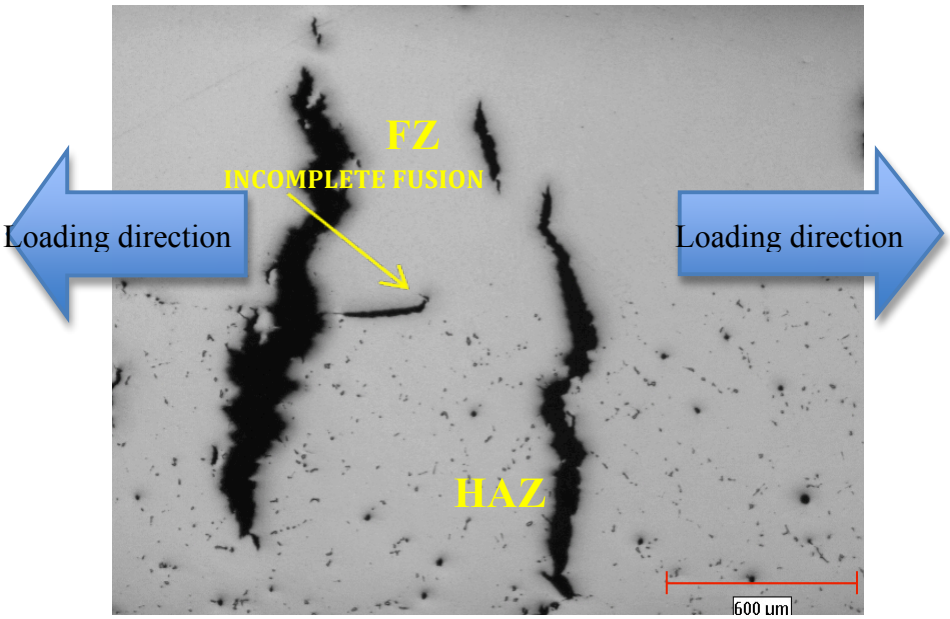

Figure 4.62 Optical micrograph showing crack initiation at line of fusion.

4.5.3. Recrystallization and annealing twins.

A. Recrystallization of the HAZ prior to TMF for IN 738 and after TMF for DS R80.

The grain size of the recrystallized regions prior to TMF in the repaired IN 738 was 29µm. For high temperature applications, creep plays a dominant role in the failure of components. Creep will normally interact with fatigue causing intergranular fatigue crack initiation and propagation. For good creep resistance properties, larger grain sizes are desirable compared to smaller grain sizes. As such, the recrystallized regions with smaller grain sizes will be thought to favour intergranular crack initiation. However, there was grain growth in the HAZ of IN 738 after the TMF. Figure 4.63 shows that the recrystallized grains merged into the substrate grains and an increase in creep damage in the recrystallized regions in the welded IN 738 may be precluded.

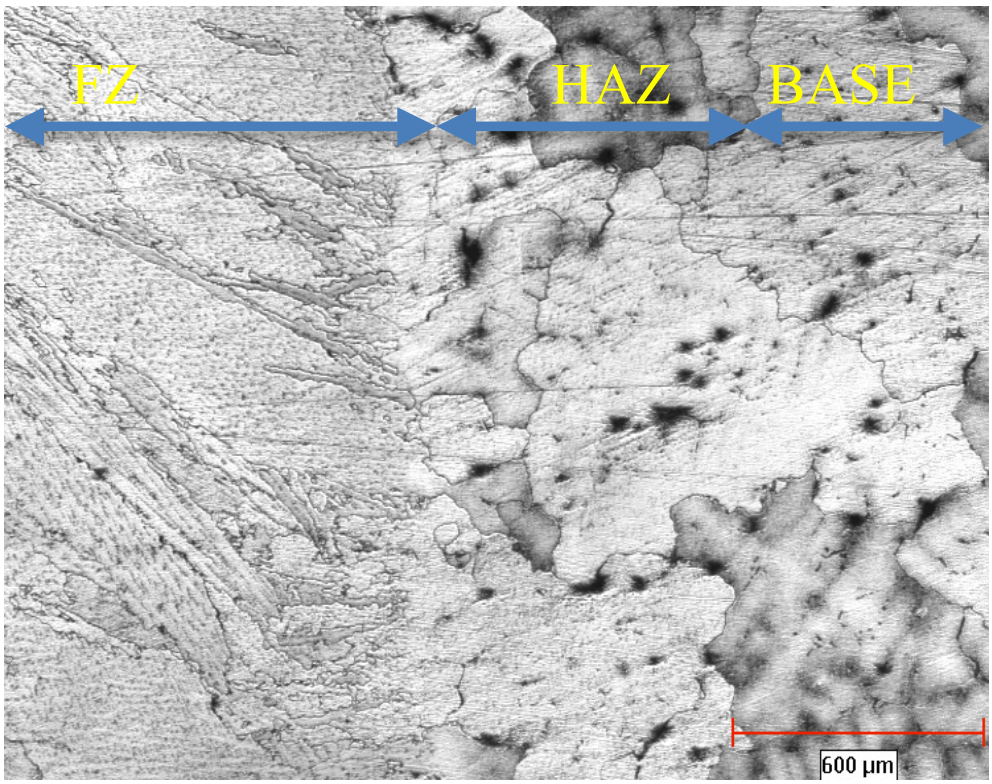

Figure 4.63 Optical micrograph of IN 738 showing grain growth in re-crystallized HAZ after TMF

However, the DS Rene 80 alloy was observed to have a different recrystallization behaviour to the IN 738 but only in 0.2% strain sample. Recrystallized grains in the HAZ as shown in figures 4.64 and 4.65 were not observed in the as weld and heat treated condition for DS R80. However, after the TMF test, equiaxed grains recrystallized in regions close to the fusion boundary only in the 0.2% strain in the DS R80. During welding, the specimen is restricted and the heat used in welding expands the specimen producing plastic strain in the HAZ. The plastic strain work hardens the HAZ region with accompanying residual stresses.

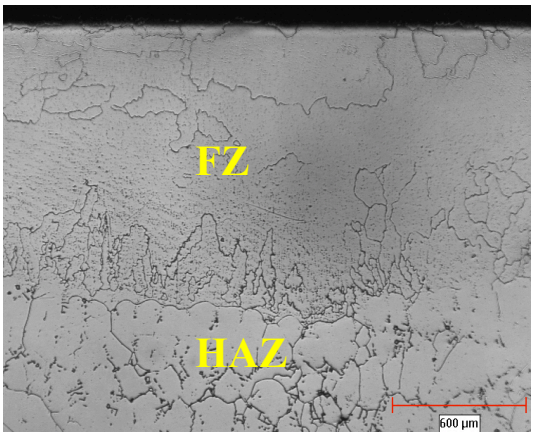

Figure 4.64 DS R80 Optical micro-graph, polished and slightly etched with Marbles, showing recrystallized grains in HAZ

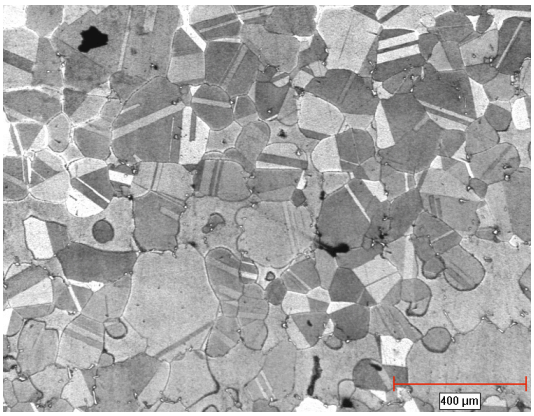

Figure 4.65 DS R80 Optical micro-graph, etched with Marbles, showing recrystallized grains & twin grains

Recrystallization was severe in regions close to the FZ and diminishes in regions away from the FZ [Fig. 4.66-4.69]. The recrystallized grains showed high tendencies of nucleating and clustering on the directionally oriented grain boundaries. Kanesund et al [6], in their investigation of the deformation and damage of IN 792 during TMF also observed recrystallization close to the grain boundaries. During loading, stresses are

amplified on grain boundaries during plastic deformation. Regions close to the boundaries will therefore undergo more deformation. These regions are likely to undergo recrystallization at high temperature during thermo-mechanical fatigue [6]. It must be emphasized that DS R80 samples cycled at strains, 0.4%, 0.5%, and 0.6% did not recrystallize. The recrystallization only occurred in the 0.2% strain sample, which ran for 120 hours with 10,000 cycles without failure.

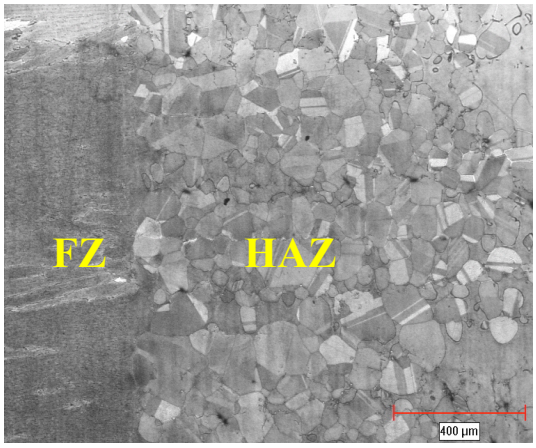

Figure 4.66 Optical micrograph, etched with Marbles reagent, showing recrystallization close to Fusion line

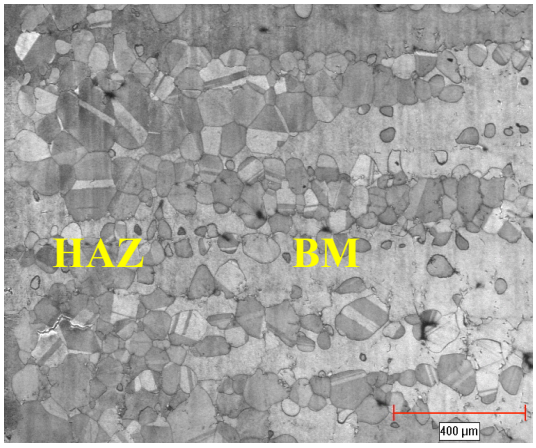

Figure 4.67 Optical micrograph, etched with Marbles reagent, showing recrystallization at distance away from Fusion line

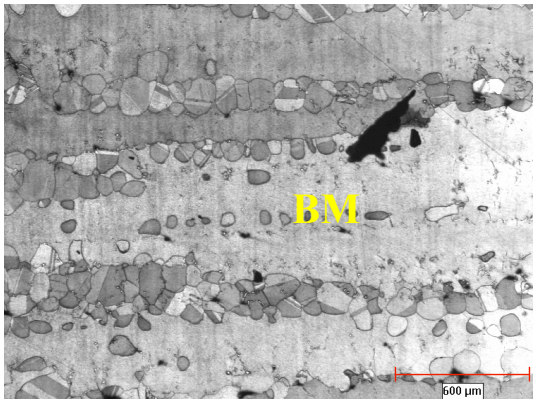

Figure 4.68, Optical micrograph, etched with Marbles reagent, showing recrystallization further away from fusion line

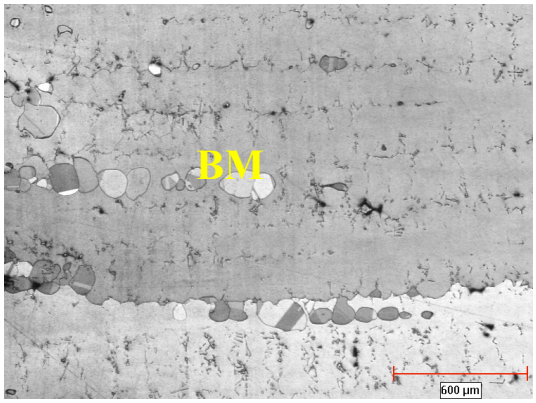

Figure 4.69, Optical micrograph, etched with Marbles reagent, showing recrystallization thinning out into base material

The recrystallization occurred as a result of a particular strain-temperature-time combination. Microstructure for strain at 0.2% baseline for DS R80 was not undertaken, which would have shed more light on the cause of recrystallization. In the absence of the test, an informed deduction can still be made based on the exact location of the recrystallized grains to the weld interface and the decrease in the density of recrystallized grains with distance away from the weld interface. The recrystallization process was a complex interrelationship between the GTAW fusion boundary, the strain induced during TMF, the temperature and time. During the TMF test, there is stress build up on the weld interface such that the stress at the interface will be relatively higher compared to regions removed away from the interface. As such, the HAZ region undergo relatively higher degree of plastic deformation with time compared to regions removed away from the weld interface and may retain some inelastic strain energy exceeding a critical strain. The temperature excursions during the TMF will anneal the highly strained HAZ causing nucleation of new grains. If the driving force for recrystallization had no relationship to the weld interface, recrystallized grains would have been uniformly distributed in the material and not confined to just the weld interface and the HAZ. Residual stresses due to welding was ruled out as possible driving force for the recrystallization because after welding, the post weld heat treatment at 1204°C and held for two hours would have been sufficient to relieve any residual stress in the HAZ. Recrystallization will have a detrimental effect on the creep rupture strength and fatigue properties of the repaired R80 component [83] with time. Recrystallization will increase the grain boundary area per unit volume and a subsequent decrease in creep resistant property of the alloy due to grain boundary sliding after long hours of exposure to high stresses and temperatures.

Also, with increase in grain boundary area, there is more conduits for easy diffusion of oxygen and other oxidation species from the environment which can further reduce the fatigue life of the repaired alloy when placed service. The SEM images shown in fig. 4.70 shows the recrystallized grains in the HAZ. Recrystallization of the DS alloy will annul the advantage of directionally oriented grains. The DS alloy will basically respond to loading just like the polycrystalline alloy and creep deformation can then become active.

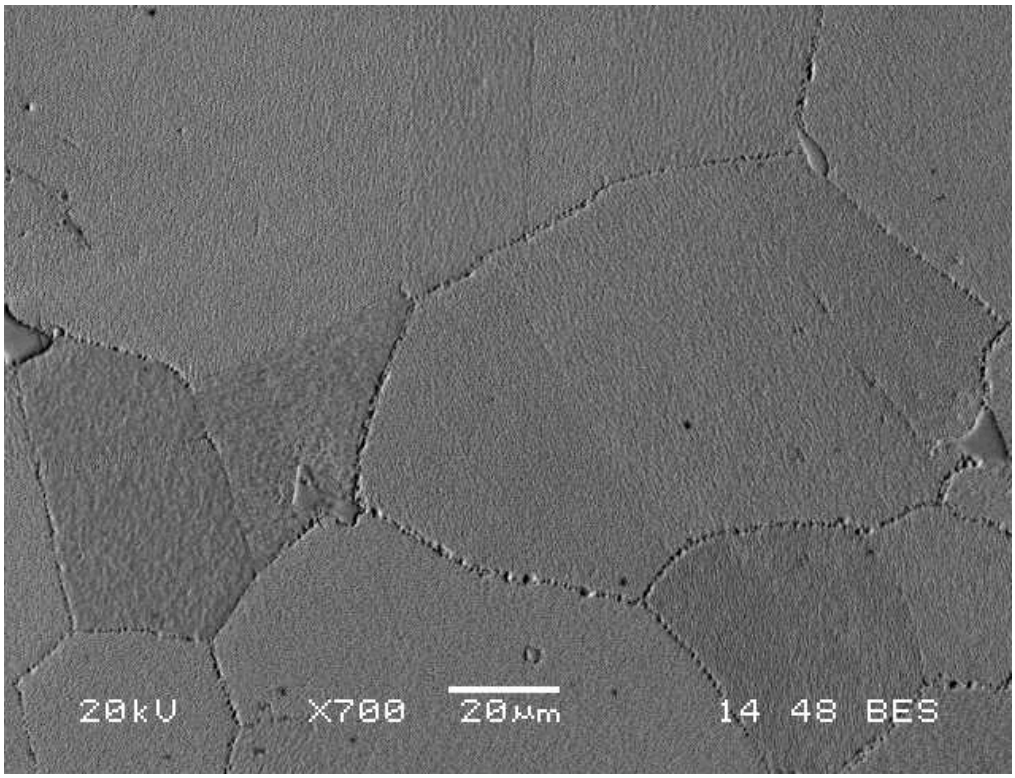

Figure 4.70 R80 SEM micrograph, showing recrystallized grains DS R80

Fig 4.71 shows creep void formation in the recrystallized region and also void initiation close to grain boundary precipitate.

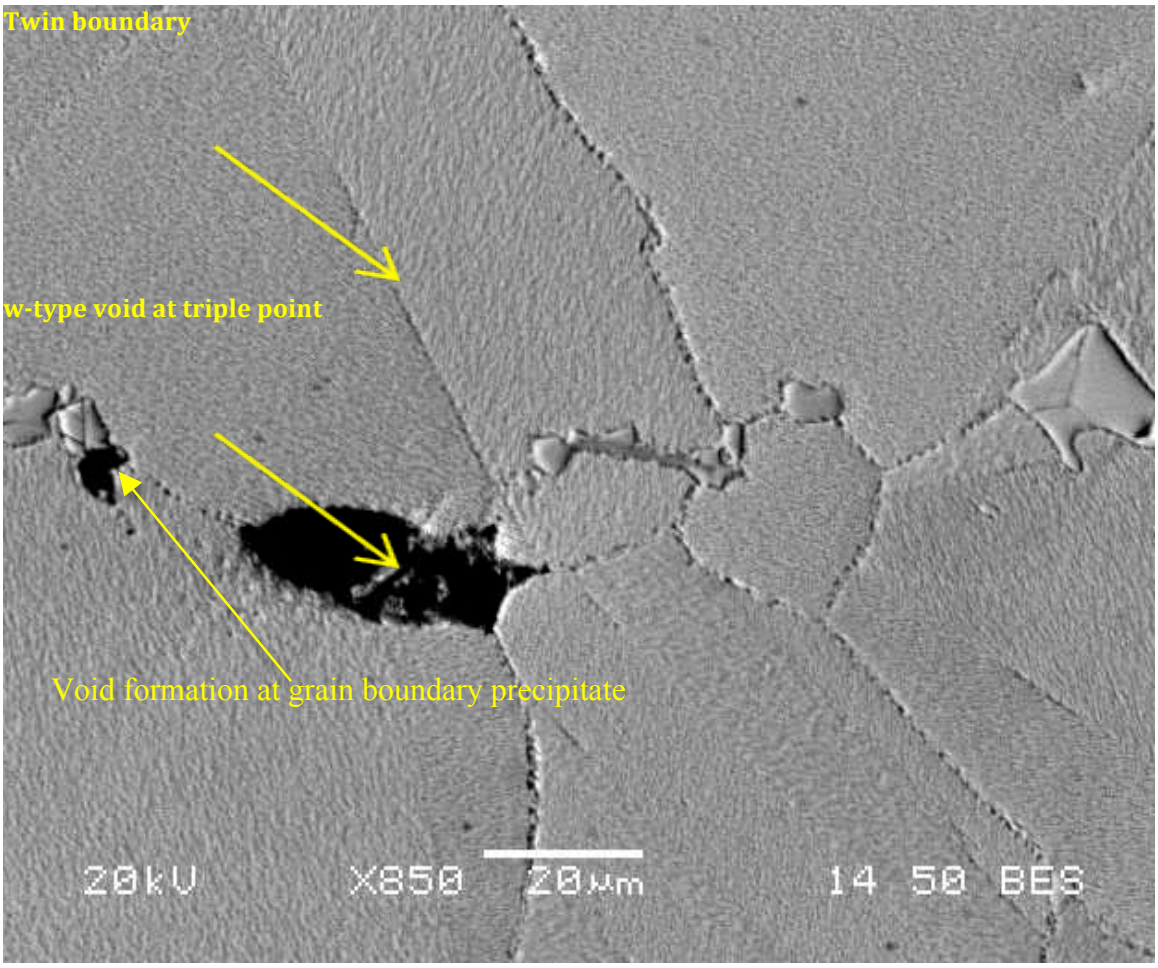

Figure 4.71 R80 SEM micrograph, showing void formation at triple points in the re-crystallized regions

However, it must be noted that the occurrence of recrystallization does not imply a drastic reduction in low-cycle fatigue life of repaired component if the prevailing strain levels at start-ups for components are low. For a reduced fatigue life due to increase in grain boundary area, a higher strain level in excess of 0.2% might be necessary. This may

be the case in real component applications where the strain levels may vary during each start-up operation. As was observed in the TMF data, the 0.2% strain sample that underwent recrystallization ran for 10,000 cycles without failing even though creep void formation was present. Perhaps the strain level at 0.2% was too low to cause rapid propagation of small cracks that can lead to the final fatal crack. For real components, especially land base turbines that can run for more than 10,000 cycles for its entire operation life, the small void/cracks may grow in response to high stresses during start-ups such that high-cycle fatigue may act sequentially with low cycle-fatigue and lead to a drastic reduction in fatigue life.

Annealing twins were also observed within the recrystallized grains [Figs 4.72& 4.73]. The effect of twins on the fatigue properties of Superalloys have been reported by Sullivan et al [10] for wrought Udimet 700.

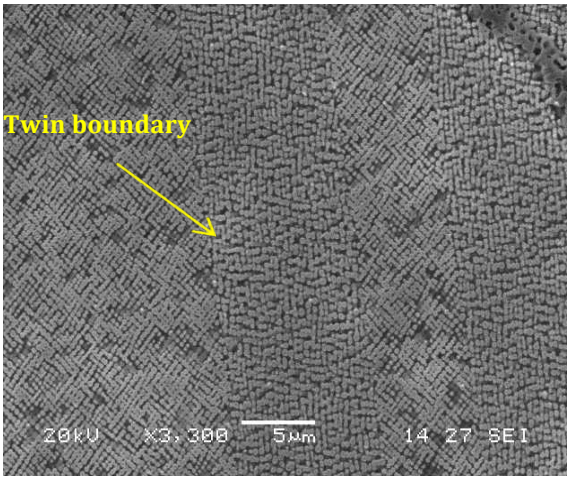

Figure 4.72 SEM micrograph of DS R80, etched with γ' etchant, showing different arrangement of γ' for twin boundaries.

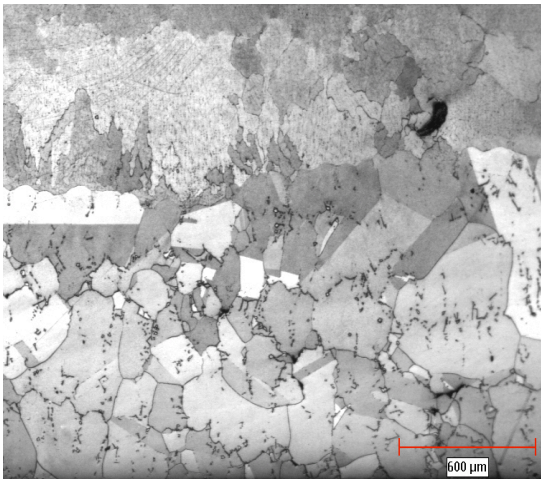

Figure 4.73 Optical micrgraph, etched with Marbles, showing annealing twins in DS R80

In their work, they reported the low cycle fatigue properties of wrought Udimet 700 at room temperature and at 760^{o}C and concluded that, surface cracks initiated along the coherent boundaries of the annealing twins as well as slip bands[10]. Zhang et al [84] and Hong [85] independently observed twin boundaries serving as crack initiation and propagation in single crystal Ni-base Superalloys [84,85] The cracks were observed to be relatively long because the twins generally run across the grain rather than ending within them [10]. However, such cracking phenomenon along coherent twins was not observed in DS R80 and IN 738 alloys in this study. Figure 4.74 shows the prominent cracks being intergranular, with no crack initiation on any of the twins. Crack propagation would selectively travel on a grain boundary as compared to a twin boundary. As such, in the absence of grain boundaries in the single crystal Udimet 700, the twin boundaries were the next favourable path for crack propagation.

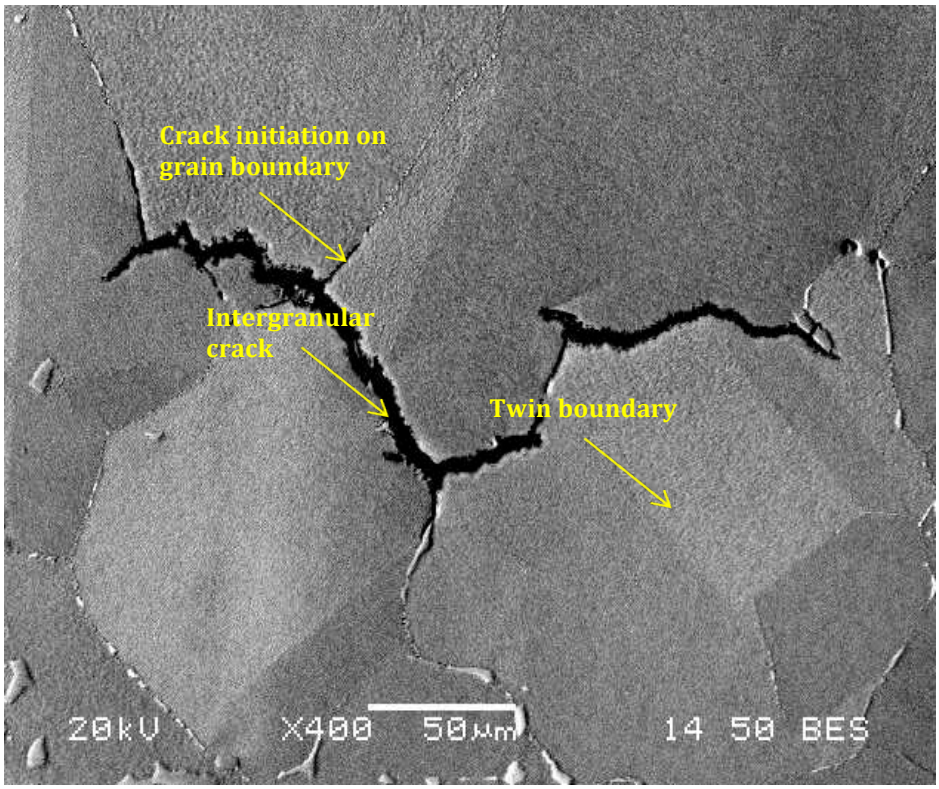

Figure 4.74, R80 SEM micrograph, back scattered, showing no crack on twin boundary

It is not known whether the absence of annealing twins will improve on the fatigue property of the alloy, but they can provide path for initial cracks to propagate in single crystal alloys. However, the contribution of twin boundary shearing, to the overall deformation and fracture process is unknown presently [10] and its effect at high temperatures in polycrystalline and directionally solidified alloys is also yet to be explored

CHAPTER 5.0 Summary and Conclusions

In an industrial environment as that observed by a turbine component such as a blade, the part is going to fail at the weakest link, with the probability of a defect initiation site most likely being at or adjacent to the free surface. The thermomechanical fatigue life and its associated failure mechanisms for both baseline and repaired (GTAW) Rene 80 and IN738 alloy were studied and the following conclusions were drawn.

(i) The TMF GTAW plot for the DS R80 alloy lies below the parent material line, with a smaller life at a given strain range value. The GTAW IN 738 showed comparable fatigue life to the baseline.

(ii) In both the parent material and the welded alloy, crack initiation from the surface of specimen were observed. In an actual component this would also translate into a sharp radius, or initiation from a cooling hole.

(iii) Oxidation also occurred in both parent material and welded conditions along grain boundaries, which leads to accelerated crack growth along oxidized boundaries.

(iv) Direct evidence for porosity acting as crack initiation sites for both baseline and repaired was observed in the present research. The porosity in the castings being about 7 microns on average with volume fractions of about 0.5-1.0 % for DS R80 and IN738 respectively may have played a role in addition to the obvious initiation sites such as surfaces, carbides and oxidation assisted cracking on grain boundaries.

(v) Initiation at MC carbide interfaces and cracking of the carbide during TMF was common to both baseline and GTAW samples.

(vi) Additional crack initiation sites present only in the GTAW samples, which led to the reduced life of the repaired DS R80 samples, include creep void formation in recrystallized regions serving as crack initiation site. The numerous crack initiations from FZ and areas underneath the weld joint suggest crack initiation from weld defects present prior to the TMF.

In summary, weak links or defects present in a material normally causes materials to fail at stress level below their theoretical cohesive strength. The weak links observed in this study include porosity, grain boundaries, and second phase precipitates. In addition, the surfaces of the samples also served as crack initiation sites leading to mechanical damage. These weak links normally act as stress raisers and amplifies the stress levels in these defect sites. The amplified stress in the localized regions of these defects subsequently initiates fatigue cracks and propagates with continuous loading. Other typical damaging mechanisms include oxidation related failures, melting of low melting point phases in IN 738 and creep deformation. The defect sites were common to both the baseline samples and the repaired samples. With similar crack initiation sites for baseline and repaired, it is expected that both will have comparative fatigue properties. However, some of the repaired samples had additional defect sites that were not present in the base line samples. They include weld cracks, HAZ micro cracking and debonded weld interface. This may account for the variability in the fatigue data obtained, with repaired IN 738 samples showing comparable fatigue properties to the baseline whereas the DS R80 repaired samples recorded poor fatigue life compared to baseline. With more potential sources for crack initiation in the repaired samples, the repaired DS R80 alloy

exhibited poor fatigue properties compared to the baseline, thus the need for a general process optimization. A good weld joint with comparatively good fatigue properties as the baseline would look more attractive to industry.

Future work

1. Recrystallization during TMF of repaired DS R80 will rob the alloy of its advantage in eliminating grain boundaries perpendicular to the stress direction. This will in effect reduce the mechanical properties of the repaired samples. It is therefore important to investigate the relationship between the GTAW joint and the recrystallization in the HAZ of the DS R80 alloy during thermo mechanical fatigue.

2. More than one test necessary for each strain level in future works since fatigue data can vary widely with scatter. This may be due to the heterogeneous distribution of defects in the material and mechanical malfunction of Gleeble equipment. This will reduce scatter and error margin in the data.

3. In the present research, the effect of each failure mechanism was not investigated separately. The contribution of each mechanism to the total failure of the repaired component can be very crucial in determining appropriate measures to reduce the damage mechanism. In order to investigate the creep effect on the fatigue property, the hold time at the peak temperature can be varied from no hold time to different times. Oxidation effect can be analyzed by conducting the experiment in

an argon or a vacuum environment to exclude the effect of oxidation and compared with the data obtained for test in air. Also, the strain rate for the test can be varied to determine the changes in failure mode with change in loading frequency.

4. The effect of softer filler alloy such as IN 600,625, and 718 versus 738 on TMF life of repaired components will be necessary in the general optimizing process of improving on the fatigue life of repaired Superalloy components and therefore require further studies.

References:

1. Private communication with Dr. N.L. Richards, University of Manitoba, MB, Canada

2. Kenneth A. Green, Tresa M. Pollock, Hiroshi Haroda, Timothy E. Huoston, Roger C. Reed, John J. Schirra, and Scott Walston. Superalloys 2004, Proceedings of the tenth international symposium on superalloys, September 19-23,2004. pp 238-244

3. C.T Sims, N. Stolloff and W. Hagel, Superalloys II: High temperature for aerospace and industrial power. pp 1-20, pp 111-116 and pg187

4. T.J. Fitzgerald and T.J. Carr, Grain boundary cracking and microstructural changes induced by the grinding of IN738LC turbine blades. Presented at the international gas turbine and aerogine congress & exhibition, Orlando Florida, June 2- June 5, 1997.

5. Yukiya Nakagawa, Aero-engine business and material technologies in Japan. Superalloys 2004, The Minearal,Metals, and Materials Society. pp 3-14

6. J. Kanesund, J. Moverare and S. Johansson, The deformation and damage mechanisms during thermomechanical fatigue (TMF) in IN 792. Procedia Engineering 10(2011) pp189-194.

7. A. Kermanpur, N. Varahraam, E. Engilehei, M. Mohammadzadeh and P. Davami, Directional solidification of Ni base superalloy IN738LC to improve creep

properties. Materials science and technology, Vol. 16, No. 5, May 2000 pp 579-586

8. M. Okazaki, T. Tabata, and S. Nohmi, Intrinsic stage I crack growth of directionally solidified Ni-base superalloys during low-cycle fatigue at elevated temperature. Metallurgical transactions A, Vol. 21A, August 1990 pp. 2201-2208

9. Tresa M. Pollock and Sammy Tin, Nickel-Based superalloys for advanced turbine engines: chemistry, microstructure, and properties, Journal of propulsion and power Vol.22, No.2, March-April 2006. pp. 361-373

10. C.P. Sullivan and M.J. Donachie Jr. Some effects of microstructure on the mechanical properties of Nickel base superalloys ASM Met. Eng. Q. Vol 7, Feb1967, pp 36-45

11. D.H. Bhadeshia, Nickel based superalloys. http://www.msm.cam.uk/phasetrans/2003/Superalloys/superalloys.html (accessed 18 Nov. 2010)

12. Janine Johnson and Matthew Donachie Jr. Microstructure of precipitation strengthened nickel base superalloys. pp 1-18, presented at 1966 National Confrence Oct. 31-Nov. 3rd, Chicago Illinos.

13. M. Okazaki, M. Sakaguchi, Thermomechanical fatigue failure of a single crystal Ni-based superalloy. International journal of fatigue 30(2008) pp 318-323

14. Ercan Balikci and Dinc Erdeniz, Multimodal precipitation in the superalloy IN738LC, Metallurgical and materials transaction A, Vol. 41A, June 2010.

pp1391-1398.The Minerals, Metals & Materials Society and ASM International 2010 DOI: 10.1007/s11661-0241-3

15. E. Balikci, R.A. Mirshams and A. Raman, Tensile strengthening in the nickel-base superalloy IN738LC. Journal of Materials Engineering and Performance, Vol.9(3) June 2000 pp 324-329

16. E. Balikci, R.A. Mirshams and A. Raman, Microstructure and texture effect on the thermal expansion of a variously aged polycrystalline superalloy IN738LC. Metallurgical and Materials Transaction A, Vol. 30A, Nov. 1999 pp 2803-2807

17. E. Balikci, A Raman and R.A. Mirshams, Influence of various heat treatments on the microstructure of polycrustalline IN738LC. Metallurgical and Materials Transaction A, Vol. 28A, October 1997, pp 1193-2003.

18. A. Thomas, M. El-Wahabi, J.M. Cabrera, J.M. Prado, High temperature deformation of inconel 718. Journal of Materials Processing Technology 177(2006) pp 469-472

19. M. A. Meyers, K.K. Chawla, Mechanical metallurgy principles and applications, 1984, Prentice-Hall Inc., Englewood Cliffs, New Jersey pp 670-676

20. George E. Dieter, Mechanical metallurgy 3rd edition, 1986, 1976, 1961 McGraw Hill Inc. pp 442-454

21. http://en.wikipedia.org/wiki/Precipitation_hardening (accessed Dec. 2011)

22. John N. DuPont, John C. Lippold, Samuel D. Kisser. Welding metallurgy and weldability of Nickel base alloys. John Wiley & Sons, Inc., Publication pp 1-2, 283-284.

23. R.J. Christiffel, E.F. Nippes, H.D. Solomon. Weldments: Physical metallurgy and failure phenomenon, proceedings of the fitfth Bolton Landing Conference pg. 14

24. Sindo Kou. Welding Metallurgy 2nd edition 2003 by John Wiley & Sons Inc. New Jersey. pp 311-390

25. ASM Vol.6 welding, Brazing and Soldering pg. 2608

26. Gas Tungsten Arc welding-GTAW www.gtz.de/en/dokumente/en-metalwork-gas-tungsten-arc-welding.pdf *(last accessed* September 17,2011)

27. W. Glaesser and I.G. Wright, Forms of Mechanically Assisted Degradation, corrosion fundamentals, testing, and protection, Vol 13A, ASM Handbook, ASM international, 2003. pp 322-330

28. R.K.Sidhu, N.L. Richards and M.C. Chaturvedi, Post-weld heat treatment cracking in autogenous GTA welded cast Inconel 738LC Superalloy, Institute of Materials, Minerals and Mining, Materials Science and Technology 2007 vol.23 No.2 pp 203-213

29. R.K.Sidhu, N.L. Richards and M.C. Chaturvedi, Effect of filler alloy composition on post-weld heat treatment cracking in GTA welded cast Inconel 738LC Superalloy.

30. ASM metals Handbook, Volume special, Heat resistant materials, pp 444-481

31. R.S Nelson, J.F. Schoendorf and L.S. Lin, Creep fatigue life prediction for engine hot section materials (isotropic), interim report CR-179550, NASA, Dec. 1986.

32. J.L. Malpertu and L. Remy, thermo mechanical fatigue behaviour of a superalloy, low cycle fatigue. STP 942, edited by H. Solomon, G. Halford, L. Kaisand and B. Leis, ASTM 1988 pp. 657-671

33. R.C. Bill, M.J. Verrilli, M.A. McGaw and G.R. Halford, Preliminary study of thermomechanical fatigue of polycrystalline MAR-M200 TP-2280, NASA Feb. 1984.

34. K. Kuwabara, A Nitta, and T.K. Kifamura, tjermal mechanical fatigue life prediction in high temperature component materials for power plant, ASME international conference, advance in life prediction, edited by D.A. Woodford and J.R. Whitehead, 1983, pp131-141.

35. V.G. Ramaswany and T.S. Cook, Cyclic Deformation and Thermomechanical Fatigue Model of Nickel based Superalloys, abstract presented at ASTM Workshop on Thermo-mechanical Fatigue and Cyclic Deformation (Charleston), 1986.

36. J. Gayda, T.P. Gabb and R.V. Miner, paper presented at NASA 4th TMF workshop, 1987.

37. Y. Pan, K. Lang, D. Lohe and E. Macherauch, cyclic deformation and precipitation behaviour of NiCr22Co12Mo9. Phys. Status solidi (a) Vol. 138, 1993, pp 133-145.

38. S. Kraft, R. Zanter, and H. Mugrabi, investigations on the high temperature low cycle fatigue thermomechanical fatigue behaviour of the monocrystalline Nickel base superalloys CMSX-6, symposium on thermomechanical fatigue behaviour of materials, STP 12630, ASTM, 1996.

39. M. Marchionni, D. Ranucci, and E. Picco, influence of cycle shape and specimen geometry on TMF of an ODS nickel base superalloy, symposium on fatigue under thermal and mechanical loading, edited by J.Bressers and L. Remy, European Commission, Petten, May 1995.

40. W. Rosenhain, D. Ewen, intercrystalline cohesion in metals, Journal Inst. Metals, Vol. 8, 1912 pp 149-173.

41. L.A. shepard and W.H. Giedt, Transgranular and intergranular fracture of ingot iron during creep, National advisory committee for aeronautics, technical notes 4285, Washington Aug. 1958

42. M.N. Ganbe and M. Heilmaier, Creep behaviour and damage of Ni-base superalloys PM1000 and PM3030. The Minerals,Metals, and Materials Society and ASM international, Metallurgical and materials transaction A, volume 40A, Dec.2009 pp 2971-2979

43. L.F. Coffin Jr. Cyclic strain induced oxidation of high temperature alloys, Trans ASM Vol. 56, 1963, pp 339-344

44. L.F. Coffin, The effect of high vacuum on the low cycle fatigue law, Metal Trans. Vol 3, July 1972 pp 1777-1788.

45. K.B. Sankara Rao, High temperature fatigue behavior of intermetallics, Sadhana Vol. 28, Parts 384, June/Aug. 2003 pp 695-708

46. P. Rodriguez and S.L. Mannan, High temperature low cycle fatigue, Sudhana Vol. 20 part 1 Feb 1995 pp123-164

47. R.W Neu and Huseyin Sehitoglu, Thermomechanical fatigue, oxidation and creep. Part 1 Damage mechanism, metallurgical transactions A, Vol. 20A Sept. 1989, pp 1755-1766

48. H-J Christ, A. Jung, H.J. Maier and R. Teteruk. Thermo-mechanical fatigue damage and mechanism-based life prediction methods. Sadhana Vol. 28 Part 1 and 2, Feb/April 2003 pp 147-165

49. Z.B. Chen, Z.W. Huang, Z.G. Wang and S.J. Zhu, Failure behaviour of coated nickel-based superalloy under thermo-mechanical fatigue. J. Mater. Sci (2009)-44: pp 6251-6257

50. M.H. Li, X. F. Sun, J.G. Li, Y. Zhang, T. Jin, H.R. Guan and Z.Q.Hu, Oxidation behaviour of a single crystal Ni-base superalloy in air I: at 800^{o}C and 900^{o}C, Oxidation of Metals, Vol. 59, No.5/6, June 2003 pp 591-605

51. R.H. Jones, Stress-Corrosion cracking: corrosion fundamentals, testing and protection. Vol 13A ASM Hand Book, ASM international 2003, pp 346-366.

52. A. Nagesba, S. Goyal, M. Valsan, K.B.S. Rao and S.K. Mannan, Low cycle fatigue behaviour of inconel alloy 783. Transaction of the Indian Institute of Metals, Vol. 63, Issues 2-3, April-June 2010 pp 575-579.

53. D.A. Woodford, Environmental damage of a cast Nickel base superalloy, Metallurgical Transactions, Vol. 12A 1981 pp 299-308

54. S. Srinivas and M.C. Pandey, Air-Environment-Creep interaction in a Nickel base superalloy: experiments and mechanisms, Engineering Failure Analysis, Vol.2 , Elsevier Science Ltd. No.3 pp 191-196

55. M.J. Starink & P.A.S. Reed, Thermal activation of fatigue crack growth: analyzing mechanisms of fatigue propagation in superalloys. Materials Science and Engineering A, Vol 491, Issues 1-2. Pp 279-289

56. Ph. E. Wagenhuber, V.B. Trindade, V. Krupp. The role of oxygen-grain-boundary diffusion during intercrystalline oxidation and intergranular fatigue crack propagation in alloy 718.

57. A. Thakur, N.L. Richards & M.C. Chaturvedi, Intl. J. Joining of Materials, Dec. 2003, 15(4), pp 21-25

58. O.A. Ojo, PhD thesis submitted to the University of Manitoba,2004. pp 4-14,224-240

59. R.K. Sidhu, O.A.Ojo, N.L. Richards and MC Chaturvedi, Metallographic and OIM study of weld cracking in GTA weld build-up of polycrystalline, directionally solidified and single crystal Ni based superalloys. Science and technology of welding and joining, 2009 Vol. 14 No.2 pp 125-131

60. S. Tin, T.M. Pollock and W. Murphy, Stabilization of thermosolutal convective instabilities in Ni-base superalloys: Carbon additions and freckle formation. Metallurgical and materials transaction A, Vol. 32A, July 2001 pp1743-1753

61. D.R. Askeland &vP.P. Phule, The science and engineering of materials (2003) 4th edition. pp. 308-311

62. S. Manson, Behaviour of Materials under conditions of thermal stresses, Heat transfer symposium at the Univesity of Michigan. *Eng. Res. Inst. Vol 27-38,1953*

63. L.F. Coffin Jr. A study of the effects of cyclic thermal stresses on a ductile metal, Trans ASME Vol. 76 (No.6) , 1954 pp.931-950

64. L. Felberbaum, K. Voisey, M. Gaumann, B. Viguier, A. Mortensen, Thermal fatigue of single-crystalline superalloy CMSX-4: a comparison of epitaxial laser-deposited material with the base single crystal. Materials science and engineering A299(2001) pp 152-156

65. M.A. Burke, C.G. Beck Jr. and E. A. Crombie, Influence of material processing on the high temperature low cycle fatigue properties of the cast alloy IN-738LC, Fifth International Symposium on Superalloys, Champion, Pennsylvania, 1984 pp 63-71

66. Callister, W. D. Jr. (2001), *Materials Science and Engineering, An Introduction*, 5th ed., pgs. 210-212, Willey and Sons Inc., New York.

67. M.Gell and G.R. Leverant, Characteristics of stage I fatigue fracture in a high-strength nickel alloy. Acta Metallurgica, vol. 16, April 1968 pp 553-561

68. E. Balikci, R.A. Mirshams, A. Raman, Fracture behavoir of superalloy IN738LC with various preciptate microstructures. Materials science and engineering A265(1999) pp 50-62

69. A.S.Khanna, Introduction to high temperature oxidation and corrosion, ASM International, 2002. pp 25

70. M. Danielewski, Kinetics of Gaseous Corrosion Processes, *Corrosion:Fundamentals, Testing, and Protection*, Vol 13A*, ASM Handbook*, ASM International, 2003, pp 97–105

71. S. Sarioglu, J.R. Blachere, F.S. Pettit, G.H.Meier, J.L. Smialek, and C. Mennicke in "Addition of reactive elements, sulphur removal and specimen thickness on oxidation behaviour of Alumina-Forming Ni and Fe-Base alloys. Materials Science Forum, Vols. 251-254(1997) pp 405-412.

72. A.W. Funkenbusch, J.G. Smeggil and N.S. Bornstein, Reactive element-sulfur interaction and oxide scale adherence, metallurgical transactions A, vol. 16A June 1985 pp1164-1166.

73. James L. Smialek, Maintaining adhesion of protective Al_2O_3 scales. JOM 2000 Jan. pp 22-25

74. M.C. Pandey, Oxidation-creep interactions in a nickel base superalloy: experiments and mechanisms. Trans. Indian Inst. Met. Vol.49 No.4 August 1996, pp 343-348.

75. Kh. Rahmani and S. Nategh, Low cycle fatigue mechanism of Rene 80 at high temperature-high strain, Material science and engineering A 494(2008) pp 385-390

76. D.J. Duquette and M. Gell, The effect of environment on the elevated temperature fatigue behavior of Nickel-base superalloy single crystal. Metallurgical transactions Vol. 3 July 1972 pp 1899-1905

77. ASM vol 11 Failure analysis: creep and stress rupture failures. Electronic version pp 1532-2909

78. R.K. Sidhu, O.A. Ojo, M.C. Chaturvedi, sub-solidus melting of directionally solidified R80 superalloy during solution heat treatment. J. Mater Sci (2008) 43: pp 3612-3617.

79. M. Zhong, H. Sun, W. Liu, X. Zhu and J. He, Boundary liquation and interface cracking characterization in laser deposition of inconel 738 on directionally solidified Ni-base superalloy. Scripta Materialia Vol. 53 Issue 2 July, 2005. pp 159-164

80. S. Benhadad, N.L. Richards, and M.C. Chaturvedi, The Influence of minor elements on the weldability of an inconel 718-type superalloy. Metallurgical and materials transactions A, Vol. 33A July 2002 pp. 2005-2017

81. O.A. Ojo, N.L. Richards & M.C. Chaturvedi, On contribution of constitutional liquation of gamma prime precipitate to weld HAZ cracking of Inconel 738 superalloy. Scripta Materialia 50(2004) pp 641-646

82. A.T. Egbewande, H.R. Zhang, R.K. Sidhu and O.A. Ojo, Improvement in laser weldability of Inconel 738 superalloy through microstructural modification. Metallurgical and Materials Transactions A, Vol. 40, Number 11, pp 2694-2704.

83. X. Huang and D. Nagy, Investigation of recrystallization phenomenon of single crystal superalloys for gas turbine applications. 45th Annual Conference of Metallurgist of CIM, Montreal, Quebec, Canada. pp 687-699

84. J.X. Zhang, H. Harada, Y. Koizumi and T. Kobayashi, Crack appearance of single crystal nickel-base superalloy after thermo-mechanical fatigue failure. Scipta materialia 61 (2009) pp 1105-1108

85. H.U. Hong, J.G. Kang, B.G. Choi, I.S. Kim, Y.S. Yoo and C.Y. Jo, A comparative study on thermomechanical and low cycle fatigue failures of a single crystal nickel-base superalloy.International Journal of Fatigue 33(2011) pp 1592-1599

APPENDIX A

EDS CHEMICAL ANALYSIS OF MC CARBIDES IN IN 738

Element	Weight%	Atomic%
Al K	-	-
Ti K	24.08	45.74
Cr K	1.23	2.16
Co K	0.54	0.83
Ni K	3.22	4.99
Zr L	0.24	0.24
Nb L	19.50	19.10
Mo L	3.62	3.43
Hf L	1.23	0.63
Ta M	41.07	20.65
W M	9.78	4.84
Totals	100.00	

Element	Weight%	Atomic%
Al K	0.00	0.01
Ti K	25.58	46.42
Cr K	0.89	1.48
Co K	0.48	0.71
Ni K	2.65	3.92
Zr L	0.61	0.58
Nb L	26.22	24.53
Mo L	3.28	2.97
Hf L	0.24	0.12
Ta M	38.66	18.57
W M	5.83	2.76
Totals	100.00	

Element	Weight%	Atomic%
Al K	-	-
Ti K	22.67	44.72
Cr K	0.78	1.42
Ni K	2.51	4.04
Zr L	0.20	0.21
Nb L	20.23	20.58
Mo L	3.34	3.29
Ta M	41.56	21.60
W M	8.81	4.53
Totals	100.00	

APENDIX B

EDS CHEMICAL ANALYSIS OF MC CARBIDES IN DS R80

Element	1	2	3	4	5
Al	0.14	0.38	-	-	0.21
Ti	70.07	66.22	64.41	69.13	74.25
Cr	1.61	2.34	2.71	1.66	0.75
Co	0.59	0.96	0.56	0.39	0.16
Ni	3.25	6.48	3.20	2.76	1.58
Zr	0.75	0.95	1.14	0.97	1.51
Nb	0.68	0.86	0.77	0.62	1.21
Mo	12.97	12.53	14.02	14.25	13.52
Hf	-	-	0.08	0.03	0.40
Ta	0.10	-	-	0.08	-
W	10.02	9.40	13.12	10.11	6.50